UNIVERSIDAD TÉCNICA FEDERICO SANTA MARÍA

DEPARTMENT OF ELECTRICAL ENGINEERING

---

# Torque Ripple Reduction of a Switched Reluctance Machine by Implementing an Optimization Based Control Strategy

---

*Supervisor:*
Prof. Alejandro Alberto
Angulo Cárdenas
*Co-Supervisor:*
Prof. Jorge Andrés
Juliet Avilés

*Author:*
Andrés Ignacio
Carvajal Carrasco

A thesis submitted in partial fulfillment of the requirements for the degree of

*MSc Electrical Engineering*

October 17, 2023

## Abstract

In recent times switched reluctance machines have started to draw attention as a feasible alternative to be implemented in electrical vehicles, due to its low-cost manufacturing and reliability at high speeds. However, the usual operation of these machines involves a high torque ripple, which can bring unwanted mechanical consequences. This is why the control strategy of these machines is vital to overcome these drawbacks. This work proposes a novel control strategy for torque–ripple minimization of a switched reluctance machine drive. The strategy is composed of two stages: (i) an outer flux–linkage reference generation layer delivers optimized patterns obtained offline via mixed-integer quadratic programming; (ii) an inner flux-linkage control loop that tracks references of the outer layer by applying an optimal switching sequence model predictive control algorithm. Each stage is tested in simulation and the results show that both the proposed reference generation technique and flux control algorithm can produce lower torque ripple and better flux–tracking performance than their state-of-the-art counterparts, them being the torque sharing function approach for reference generation, and the finite control set model predictive control and the deadbeat predictive control algorithms for flux–tracking. The proposed strategy and its components are implemented in an experimental setup, which consisted of a 2.32 kW switched reluctance machine being fed by three Asymmetric Bridge Converters. The switched reluctance machine is coupled to a 2.23 kW induction machine working as a regenerative brake and is controlled by an external AC drive. The experimental outcome validated the proposed approach and the results obtained by simulation.

# Acknowledgements

A mis padres, Claudia y Rodrigo, a quienes admiro y que siempre me han brindado su amor incondicional. A mis hermanos Esteban, Vicente y Rosario, con quienes aprendí a jugar y reír. Al resto de mi familia, por todo su cariño y apoyo. Gracias a todos ustedes, de quienes considero que provienen mis mejores cualidades.

A Fernanda, quien estuvo conmigo durante todo este proceso, entregándome su amor todos los días. Gracias por creer en mí cuando dudaba, y hacerme reír cuando me apenaba. Espero con ansias compartir contigo nuevos desafíos y aventuras.

A mis amigos y amigas, con los que siempre pude contar y que me alegraron los días con su compañía. A los cabros del LIAcE, con los que disfruté esta última etapa y me ayudaron enormemente para sacar este trabajo adelante, especialmente a Cristóbal, que me aportó con más de una solución. Como olvidar también a Carlos (Chico Mark), que me enseñó con humor y carcajadas a no quejarme de la adversidad. A los cabros de pañol, que literalmente me salvaron en la parte experimental de esta tesis en múltiples ocasiones. Son unos cracks.

A mis profesores, que con dedicación y paciencia me formaron durante estos años. Especialmente agradezco a los profesores Alejandro Angulo y Jorge Juliet, los cuales me dieron su confianza y me guiaron pacientemente durante este proceso.

Finalmente, agradecer nuevamente a todos ustedes que me apoyaron durante esta etapa, haya sido estudiando juntos o compartiendo una risa. Este trabajo hubiera sido imposible sin esos detalles, así que por eso se los dedico a ustedes.

A la Agencia Nacional de Investigación y Desarrollo (ANID), que por medio del proyecto basal FB0008“ Advanced Center for Electrical and Electronic Engineering, AC3E” y los proyectos Fondecyt Regular N°1210625 y N°1191520, colaboraron con el desarrollo de este trabajo.

# Contents

# List of Figures

# List of Tables

# Chapter 1

# Introduction and motivation

Due to the imminent threat of global warming and the subsequent climate change phenomena, several efforts have been made worldwide to decrease the use of fossil fuels and CO2 emissions. Among the most important sources of greenhouse gas emissions globally, the transportation sector is responsible for 23% of them worldwide [4]. Therefore, during the past decade, the interest and study of electrified, more efficient powertrains have increased more than ever [5, 6], leading to new technology development regarding alternative motor topologies and control strategies. Specifically concerning electrical machines, switched reluctance machines (SRM) have proven to be a promising alternative for traction applications due to their low-cost, rugged construction and wide constant-power speed range [7]. However, it has not yet been widely adopted by the industry due to its inherent drawbacks: high torque ripple and acoustic noise. Nonetheless, the continuous development of power electronics technologies and control techniques has proven that these drawbacks can be overcome [8].

Numerous control techniques have been proposed to decrease torque ripple. The most commonly used consists of an inner current control loop fed by current references found by different methods, like the Torque Sharing Functions (TSF) [9]. The inner control loops usually use hysteresis controllers [1] or Proportional Integral (PI) regulators [10]. Due to the nonlinear characteristic of the SRMs, predictive control techniques have proven to be a promising alternative to control inner variables of the machine, like current or magnetic flux [11]. Regarding the reference generation for inner control loops, some interesting approaches have been taken by shaping the waveforms of the inner variables by numerical optimization techniques [3, 12] to minimize the output torque ripple of the SRM.

This document proposes a novel torque control scheme for SRMs composed of an inner magnetic flux controller fed by an outer flux reference generator. The internal control loop implements an optimized switching sequence model predictive control (OSS-MPC) algorithm, based in [2], thus ensuring a high tracking performance. The torque reference is an input for a look-up table (LUT) containing the optimized flux waveforms, parametrized in speed, torque, and position. These patterns are computed offline using mixed-integer quadratically constrained programming, similar to the formulation proposed in [3]. This flux pattern reference generation technique will be called Optimal Flux Waveform Generation (OFWG). By adopting this control scheme, the torque ripple decreases in steady–state compared to state–of–the–art techniques. The structure of this work comprises the following chapters:

Chapter 2 addresses relevant background information on SRM control and torque ripple minimization, presenting and analyzing state-of-the-art strategies. Chapter 3 outlines the experimental procedures for obtaining flux-linkage and torque characteristics needed for implementing OFWG and OSS-MPC, providing detailed explanations and result analyses. Chapter 4 introduces the proposed control approach, comprising an external flux-linkage reference generation layer solved using a mixed-integer quadratically constrained program, along with an internal control loop implementing an OSS-MPC for machine flux-linkage control. Moving to Chapter 5, the proposed control strategy and its components undergo simulation testing, with comparisons to other state-of-the-art techniques and subsequent analysis and computational validation. In Chapter 6, experimental validation of the proposed strategy is carried out, including a description of the implemented setup and additional components in the control scheme, along with performance-enhancing maneuvers to analyze further and discuss the experimental results, thus validating the proposed strategy.

Finally, Chapter 7 presents a comprehensive review of the work, discussing final thoughts and reaching conclusions about the entire study.

## 1.1 Hypothesis

Considering a 12/8 switched reluctance machine fed by an asymmetric bridge converter, the main control objectives for achieving high-quality performance are: (i) to minimize the torque ripple; (ii) to reduce the conduction losses; and (iii) to decrease the switching frequency of the converter. Regarding these requirements, we claim the following:

*A SRM drive comprising flux–linkage control loop fed by an outer flux reference generation layer can be achieved by combining an OFWG approach with an OSS-MPC algorithm. Using OFWG, the outer layer will generate optimal flux–linkage patterns used as a reference for the flux control loop based in OSS-MPC. This strategy will achieve a lower torque ripple than state–of–the–art control strategies, reducing the average switching frequency, and keeping low conduction losses.*

## 1.2 Objectives

- To design and implement an SRM drive composed of an outer flux reference generation layer that feeds a inner flux–linkage control loop. This scheme should achieve a lower torque ripple than traditional control schemes, using offline flux–linkage patterns for the reference generation, and a modified OSS–MPC algorithm for the flux-linkage tracking.

- To identify the machine's parameters by designing and implementing experimental laboratory tests.
- To propose a mixed–integer quadratically constrained program that solves the torque ripple minimization problem and implement it in a wide range of operational points.
- To load the optimal flux-linkage patterns to a flux reference generator control block. It will provide flux references as a function of the machine's position, speed, and torque reference.
- To implement an OSS-MPC-based algorithm in order to track the flux–linkage of the machine successfully.
- To efficiently develop the proposed strategy's implementation and verify its real-time execution capability on a commercial control platform.
- To implement the proposed strategy in a laboratory setup along with other state–of–the art techniques and compare their performance.

# Chapter 2

# Background

Since 1969, variable reluctance motors [13] have been proposed for variable speed applications. The origin of this motor can be traced back to 1842, but their “reinvention” has been possible due to the advent of inexpensive, high-power switching devices. This machine has wound field coils for its stator windings, and it has no coils or magnets on its rotor. The stator and rotor have salient poles; hence the machine is called a doubly salient machine. The cross–section of such a machine is shown in Fig. 2.1.

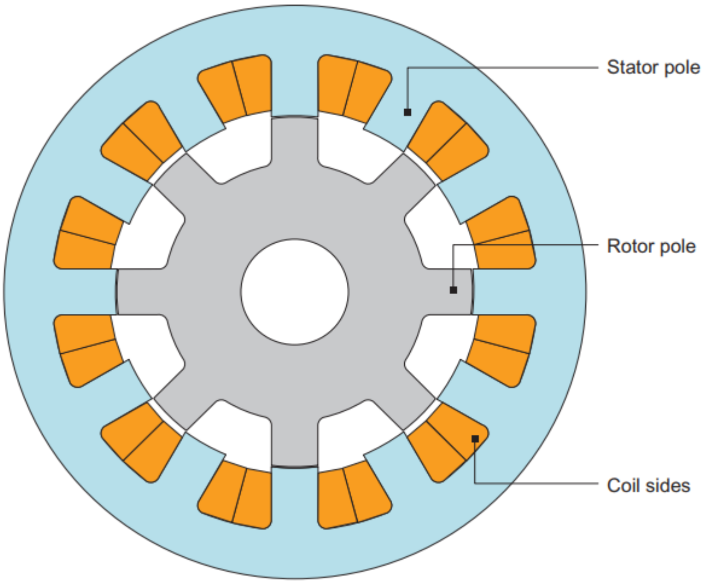

Figure 2.1: Cross section view of a SRM [1]

This type of machine makes use of the elementary principle of electromechanical energy conversion, which states that given constant magnetic flux (generated by a constant current) that circulates in a magnetic circuit with a variable reluctance, dependent on the relative position of its components, a force is generated between them that seeks to decrease the reluctance value of the magnetic circuit and also to increase to coenergy of the magnetic field [1]. Thus, the explanation of how these machines work comes naturally. When a set of stator poles are excited, the rotor moves towards a position in which two rotor and two stator poles are aligned, reaching the minimum reluctance position, but at the same time leaving another set of rotor poles out of alignment with respect to a different set of stator poles. Then, this last unaligned set of stator poles is excited to get aligned with the rotor poles, and so on. By doing this sequentially, the rotor spins. The movement of the rotor and the torque generation is caused by switching currents into stator windings when there is a variation of reluctance; therefore, this variable speed machine is referred to as an SRM.

The SRMs have a simpler, cheaper, and more robust construction than some of the most commonly used electrical machines. Permanent magnet machines have magnets on the rotor, and induction machines have conductors in theirs. Also, the synchronous reluctance machine has a complex rotor topology that makes them more expensive. The SRM stator comprises a salient pole laminated core with concentrated windings, while the rotor also has a salient pole structure without windings or permanent magnets. This enables reliable operation at high speeds due to its robust rotor core, which makes it resistant to rotor displacement and rotational stress. The double salient structure also allows it to operate at high temperatures, partly due to the absence of a rotor winding and its inherent thermal limitations [1]. This structure also brings many challenges, being the most significant the existence of high torque ripples that negatively impact the machine's performance. The existence of torque ripples also brings undesired consequences, such as acoustic noise and vibration. The solution of the torque ripple drawback is defined as the main motivation of this work.

## 2.1 Operational principles and modelling

### 2.1.1 Equivalent circuit of an SRM

SRM are basically composed of stator windings excited by a DC voltage and no windings on the rotor. Each phase of the SRM is electrically independent of each other, and therefore it can be controlled separately. A generalized expression for an arbitrary phase of an SRM which neglects coupling effects between the phases [1], is the following:

$$v = Ri + \frac{d\psi}{dt}, \tag{2.1}$$

Where $v$ is the voltage across the coil, $R$ is the resistance, $i$ denotes the current, and $\psi$ is the flux linkage of the coil. A simplified equivalent circuit is shown in Fig 2.2.

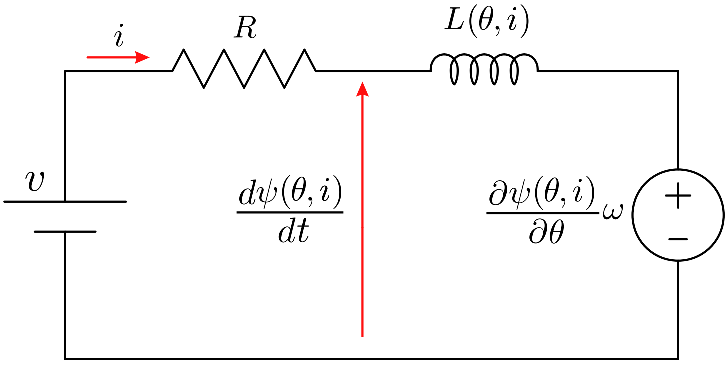

Figure 2.2: Equivalent circuit of a SRM

Flux–linkage is produced only when the stator coils are excited with current. Due to the salient structure of SRM, the air gap between the rotor and stator poles changes based on the relative position of the rotor and the stator. Also, due to the magnetical saturation of the core, the flux–linkage has a non–linear dependence regarding the excitation current. For this reason, the phase inductance depends on rotor position $\theta$ and current $i$. Therefore, the flux linkage expression for an SRM appears as follows:

$$\psi = \psi(\theta, i) \tag{2.2}$$

If we replace (2.2) in (2.1) and chain rule is applied, we obtain:

$$v = Ri + \frac{\partial\psi(\theta, i)}{\partial i}\frac{di}{dt} + \frac{\partial\psi(\theta, i)}{\partial\theta}\frac{d\theta}{dt} \tag{2.3}$$

Defining $\frac{d\theta}{dt}$ as the rotational speed $\omega$, and $\frac{\partial\psi(\theta,i)}{\partial i}$ as the phase inductance $L(\theta, i)$, (2.3) can be rewritten as:

$$v = Ri + L(\theta, i)\frac{di}{dt} + \frac{\partial\psi(\theta, i)}{\partial\theta}\omega \tag{2.4}$$

As depicted in (2.4), phase inductance is both dependent on rotor position and phase current. The inductance dependency on the current is because when the magnetic core of an SRM saturates, the permeability and, hence the inductance decrease. The inductance dependency on the position is caused because, at different rotor positions, the air gap between the stator and rotor poles varies, and so does the reluctance seen from that phase. Also, it is interesting to note that the last term in the right of (2.4) depends linearly on the rotational speed of the machine. This voltage term can be identified as the back electromotive force or Back-EMF of the SRM.

### 2.1.2 Torque generation

The power conversion process in SRM can be explained by the definitions of forces in electromagnetic fields, which states that the electromagnetic torque $T_e$ can be defined as

$$T_e = \frac{\partial W^{'}(\theta, i)}{\partial \theta} \tag{2.5}$$

where $W^{'}$ represents the system co-energy, and it can be defined as:

$$W^{'}(\theta, i) = \int_0^i \psi(\theta, u)\, du \tag{2.6}$$

From (2.5) and (2.6), it is possible to analyze the case where the machine is operating without magnetical saturation of the core. In this case the phase inductance is no longer dependent on the excitation current. Therefore the phase inductance in linear region can be defined only as $L(\theta)$. Having this into consideration, the torque expression in the linear region $T_e^{\text{unsat}}$ is equal to:

$$T_e^{\text{unsat}} = \frac{1}{2}\frac{dL(\theta)}{d\theta} i^2 \tag{2.7}$$

From (2.7) it can be observed that the direction of torque is independent on the polarity of the current, due to their quadratic relation.

### 2.1.3 Operational characteristics

As mentioned before, the SRM torque generation mechanism originates in the rotor/stator salient structure. Consequently, the machines' flux and torque characteristics depend on the rotor position and the current circulating through the windings. In the SRM, each phase achieves one electrical cycle when the rotor poles move from an unaligned position to the next, reaching at 180 electrical degrees the alignment of the rotor and stator poles, as depicted in Fig. 2.3a, which shows one electrical cycle in a 6/4 SRM (six stator poles and four rotor poles). In this figure, the green stator pole represents the pole to which the given phase to be analyzed is wound up, and the blue rotor pole represents the closest rotor pole during one electrical cycle. In Fig. 2.3b, the flux profile of the same given phase is shown during a whole cycle, and it's noticeable how the flux linkage increases while the rotor moves towards the aligned position and decreases when it moves towards the unaligned position. This occurs because the permeability of the magnetic path increases, and therefore the reluctance decreases. It is also important to notice how the flux linkage value does not increase linearly with the current value because of the iron's magnetic saturation. Unlike the aligned position, the magnetic saturation is not noticeable when the rotor is unaligned with the stator.

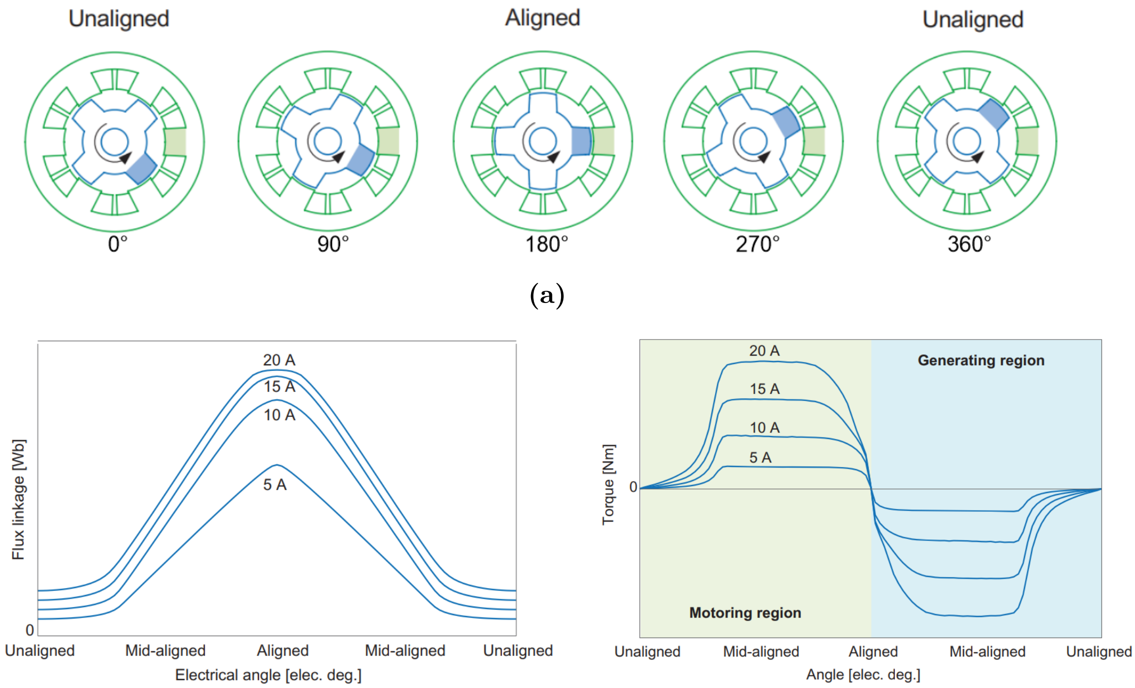

(a)

(b)

(c)

Figure 2.3: Rotor position during one electrical cycle along with the flux and torque profiles for different excitation currents for one electrical cycle [1]. **(a)** Rotor position; **(b)** Phase flux; **(c)** Rotor torque

Also, in Fig. 2.3c it is shown that the torque produced by the machine is positive when the magnetic flux is increasing with the rotor position and that it is negative when it is decreasing, which matches with the expression shown in (2.7), and that also states that the torque profile is independent of the direction of the current. Finally, it is necessary to note that when the coils of a conventional SRM phase are energized with current, most of the generated flux-linkage remains in the same phase, and no significant coupling between phases occurs. Therefore, the mutual flux is negligible. Consequently, once the characteristics of one phase of an SRM are determined, they can be used for other phases as well [1].

## 2.2 Asymmetric Bridge Converter

To ensure continuous torque production, it is necessary to excite the different phases sequentially; therefore, a power converter is required. The Asymmetric Bridge Converter (ABC) is the most commonly used converter for SRM applications and is the one that is used in this work. This converter consists of two switching devices and two diodes placed diagonally, as shown in Fig. 2.4. Since each phase in an SRM is electrically isolated from each other, one asymmetric bridge converter is required for each phase.

A DC voltage source feeds this converter, and it has three different states of conduction, as shown in Table 2.1. The first state of conduction energizes the phase by applying $+V_{dc}$ to it, thus increasing the phase current while this state is applied. In this operation mode, both switching devices are conducting. In the second state, both switching devices are off; therefore, the voltage applied to the phase is $-V_{dc}$, decreasing the phase current. It is called a Hard Switching (HS) operation when only these two conduction states are applied. The third state of conduction is often applied in most control schemes because of its lower current decay rate than the second state. It is produced by only activating one switching device, letting the phase without excitation. This last state of conduction is called freewheeling, and when it is present, the mode of operation is called Soft Switching (SS). The freewheeling state can be subdivided into two different states, thus having a total of 4 possible states or voltage vectors that can be applied to each phase. A graphical explanation is shown in Fig 2.4.

Table 2.1: Output voltage vectors and switch configurations.

| Vector | $S_1$ | $S_2$ | $v$ |
|---|---|---|---|
| $P$ | 1 | 1 | $V_{\mathrm{dc}}$ |
| $O$ | 1 | 0 | 0 |
| $O'$ | 0 | 1 | 0 |
| $N$ | 0 | 0 | $-V_{\mathrm{dc}}$ |

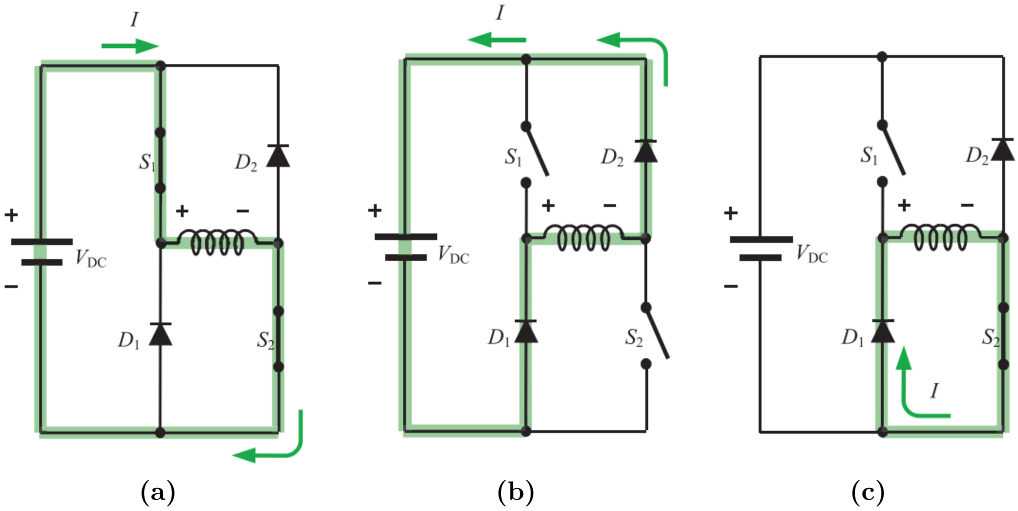

Figure 2.4: Operational modes of asymmetric bridge converter for one phase. **(a)** Both switching devices are on, $V_{DC}$ is applied to the phase; **(b)** both switching devices are off, -$V_{DC}$ is applied to the phase; **(c)** freewheeling mode, voltage across the phase is zero [1]

.

## 2.3 Current regulation

For SRM drives performance enhancement, there have been multiple different approaches taken. A significant portion of them are based on the generation of current patterns, which are taken as reference for nested control; therefore, the current tracking capability of these current patterns have been widely studied. The SRM presents significant current tracking challenges regarding its highly nonlinear behaviour due to varying phase inductance and magnetic saturation. The same nonlinear behaviour is also present on the references to be tracked. Among the most classic current control techniques, the most widely known is the hysteresis current control [1], which consists of the use of an hysteresis controller with a predetermined hysteresis band, having this last one a considerable impact on the SRM drive performance such as torque ripple, semiconductors losses, and so on [14].

As to the rest of conventional techniques used in current control of SRM drives, there are those based in PI regulators including a modulation stage such as Pulse-width Modulation (PWM) [10,15–23]. PI regulators compensate for the error in the current tracking, and the reference voltage is applied using a modulation stage as a PWM, providing a constant switching frequency [10, 15]. Within this category, one of the first studied control schemes is the state feedback controller [16]. Considering that the SRM has a nonlinear nature, it is evident that the design of linear controllers becomes very difficult. That is why some studies present linearized modelling of SRMs for the design of closed-loop current controllers, such as small-signal modelling, where linear SRM model is derived for nominal operating conditions in [17]. Another linear SRM model is made based on the inductance profile of the machine [18]. These models are then used to design a fixed gain PI controller.

Another challenge in the current regulation of SRM using PI-based techniques is the back-EMF compensation. It is easy to see in (2.4) that this component of the machine's fundamental equation can be very determinant, especially if the speed is high. Contrary to the DC machine, the change of the back-EMF voltage on SRMs are faster and greater. Therefore, the back-EMF at the SRM has a significant impact on the dynamic performance of the controller. That is why the compensation becomes so important to compensate this disturbance that degrades the tracking capabilities of the PI controllers. Among the multiple back-EMF compensation techniques, it is possible to employ a technique based on offline estimations from flux-linkage data [19], or it also can be compensated using a back-EMF observer [20], allowing the current rate to increase and also to decrease the burden on the PI controller. Finishing with the most conventional control PI-based regulation techniques, it is necessary to also take into account the variable gain PI controller [21], where the gains are adjusted as a function of both current and rotor position, ensuring better tracking performance.

Exploring the non-conventional current control techniques, it is possible to find the adaptive current controllers, which are another alternative to deal with the highly nonlinear behaviour of SRMs, by dynamically adjusting the controller gains. These techniques are also implemented with PWM modulation, so it keeps the advantage of ensuring a fixed switching frequency. These controllers employ complex online equations, resulting in a more complex control than their linear counterparts [22, 23].

In the last few years there has been significant development and interest in studying predictive control techniques, which have become an attractive alternative to conventional control techniques, due to their capability of handling nonlinearities, their consideration of the discrete nature of power converters in the calculation of control actions, the simplicity of implementation and its effectiveness in dynamic response [24]. These techniques can be classified into two categories: one computes a duty cycle modulated by PWM, while the other directly determines the converter's switching states. In the first group, some of the most studied are the deadbeat predictive control (DBPC) [25, 26] and the continuous control set (CCS-MPC) [27, 28], where the DBPC makes use of a predictive model without considering the system's limitations as a means to determine which voltage value should be applied in order to produce zero tracking error in one digital time step, as the minimization of a cost function characterizes CCS-MPC in order to determine the control output. In the second group, the finite control set (FCS-MPC) technique is found, which is very similar to CCS-MPC, but it has the difference that it directly computes the switching state directly or optimal switching vector (OSV) that will be applied during the whole next sampling period. In [11] an FCS-MPC technique is proposed, where flux-linkage is tracked in order to control phase currents indirectly. This last technique is also known as virtual flux finite control set (VF-FCS-MPC). The flux–linkage control approach has not been widely studied yet and there is not much literature about it so far.

### 2.3.1 Optimal Switching Sequence Model Predictive Control

The classic FCS-MPC techniques use the discrete nature of the power converters to simplify the MPC problem. Using a finite set of possible switching states reduces the optimization problem's complexity, achieving a fast dynamic response. Nonetheless, since it applies the OSV directly into the converter with no modulation stages during one sample time, the optimal solution could be the same for consecutive sample steps. This causes a variable switching frequency that leads to a disperse harmonic spectrum which may be desirable from an acoustic perspective, and it also produces higher ripple in the current waveforms delivered by the converter [29].

Due to the torque ripple drawback present in applying FCS-MPC, another alternative is first proposed in [30], which consists of an algorithm that searches the optimal switching sequence of switching vectors and the time of application of them in one sample period to track active and reactive power outputs for grid-connected power converters. This technique is called OSS-MPC, and it has also been applied to grid-tied 3-level NPC converters [31, 32], LC-filtered voltage source inverters [33], and single-phase NPC converters [2], among others.

The OSS-MPC algorithm first defines sequences of switching vectors (SV) that the converter can potentially apply. Then, based on the values of these SV, it computes the variation of the control variable when one of them is applied. By using this information, the algorithm solves an optimization problem which finds the optimal times of application of these SV by minimizing a cost function, which can be the tracking error between the reference variable and the predicted variable obtained by applying the SV during the times of application as shown in Fig. 2.5a. This process is repeated for each switching sequence. Then, by comparing their optimized cost functions, it selects the one with the lowest value of it. Once the sequence is selected and the optimal time of

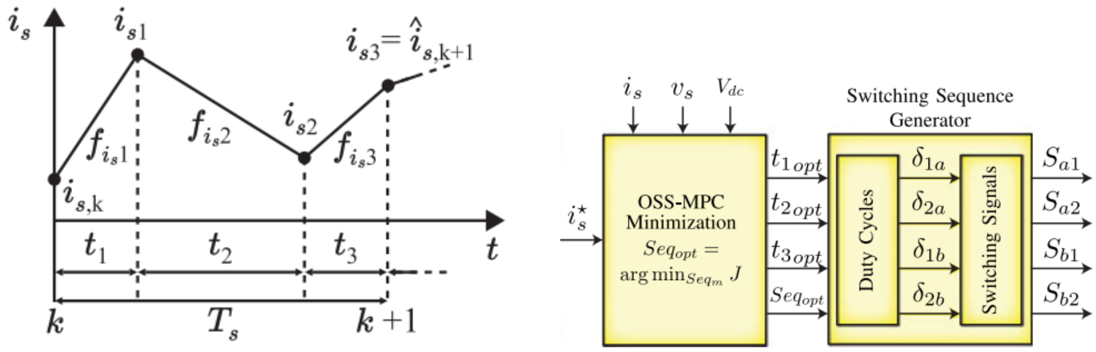

**(a)** **(b)**

Figure 2.5: **(a)** Predicted current trajectories for a switching sequence of three vectors; **(b)** OSS block diagram [2]

application of each SV is computed, it is possible to generate switching signals by first translating the application time into a duty cycle and then using a modulation stage, as shown in Fig. 2.5b.

## 2.4 Torque control

Due to the double salient structure of the SRMs, the generated torque is pulsating, and there is no reference transformation yet to eradicate the position from its voltage and torque expression, as stated in equations (2.4) and (2.7). Therefore, the most known vector control methods used in AC machines cannot be directly used in SRM drives, including the ones regarding torque control. That is why multiple works regarding the study of torque control in SRM drives have been proposed, where it is roughly possible to classify them as conventional or predictive techniques.

Among the conventional techniques, some of the first strategies studied are TSF [9]. The TSF proposes generating appropriate per-phase torque references by distributing them accordingly to a numerical function and then using a nonlinear function $i(T, \theta)$ to convert the torque reference to current reference. It is possible to subdivide TSF in three categories: analytical [9, 34], dynamical allocation [35, 36] and numerical optimization [12, 37, 38]. An alternative to TSF is the current profiling technique [39, 40], which directly determines the reference current without using any LUT. The current profiling method starts from a simple reference current and requires fine-tuning to reach the final reference value. Another strategy is the harmonic current injection technique, which takes advantage of the periodic characteristic of the current and flux-linkage profiles and adds harmonic components to the current reference [41, 42] to improve the torque ripple. Some works have intended to use vector control approaches to improve torque control performance [43, 44]. The torque control strategies presented so far are all indirect, thus requiring the use of a current control loop and making the torque control performance dependent on the current controller's tracking capability.

There exist other conventional strategies that do not rely on internal control loops, such as Direct Instantaneous Torque Control (DITC) [45] and Direct Torque Control (DTC) [46]. DITC consists basically of a torque estimator and torque hysteresis controller. The first computes the torque tracking error using the reference torque, and the second generates the appropriate switching signals based on the estimated torque error and position information. On the other hand, DTC, which was created inspired by the DTC technique employed in induction machines, uses the torque error, flux-linkage error, and flux-linkage vector sector information to decide the appropriate voltage vector which could keep the torque and flux linkage within a hysteresis band.

Over the last few years, there has also been a significant development in predictive torque control techniques for SRMs due to their potential to control highly nonlinear systems simply but effectively. Among the methods which do need a modulator, some of the most studied are deadbeat predictive torque control [47–49] and virtual voltage finite control set (VV-FCS-MPC) [50], where the first one computes the optimal input voltage in the form of duty cycle directly using the predictive model and omitting the use of a cost function, and the second resolves an optimization problem based in a cost function in each sampling instant, using Discrete Space Vector Modulation (DVSM) with virtual state vectors.

There also exist predictive torque strategies which do not use modulation stages, such as approaches based on conventional FCS-MPC [51, 52], and virtual–flux FCS-MPC (VF-FCS-MPC) [53]. This recent study proposes a voltage vector approach combined with current control based on virtual-flux estimation, resembling the methodology introduced in [11].

### 2.4.1 Optimal waveforms for SRM

The torque ripple minimization problem has been proven to be suitable for a standard numerical optimization procedure, where the RMS current can be part of the objective function [12, 54]. The constant torque requirement is the equality constraint. Other conditions, such as the current limitation, form the inequality constraints.

Due to the nonlinear relation between flux linkage and torque with the circulating current and position on an SRM, the mathematical representation on optimization models of these characteristics imposes a challenge. In [3], they address this issue by replacing the torque and flux linkage nonlinear characteristic with a piecewise affine approximation, as seen in Fig. 2.6, where the flux-linkage $\psi$ is defined as a function of the magnetomotive force $F$ and the position $\theta$. By approximating this problem as a mixed-integer convex program, it is possible to solve it globally using state-of-the-art solvers. The optimization problem which the last work intends to solve assumes that the phase current $i$, the phase voltage $v$, and the flux-linkage $\psi$ are $2\pi$–periodic functions of the position $\theta$.

The results shown in this work are promising due to the generalized model proposed and the results obtained in the simulation. Still, it is important to mention that no experimental work regarding the optimization of current waveforms using similar mixed-integer convex programming (MICP) formulation has been presented in recent works. A similar problem is solved and implemented in an experimental setup in [38]. However, in this work, the machine dynamics constraints are only applied between the positions where the torque is positive, and the current can only take non-zero values over the same position range. Furthermore, the dynamic constraints are dependent on the sampling time of the current control strategy. These considerations do not allow satisfactory current tracking during the whole cycle and do not allow taking advantage of negative torque by over-restricting the optimization problem.

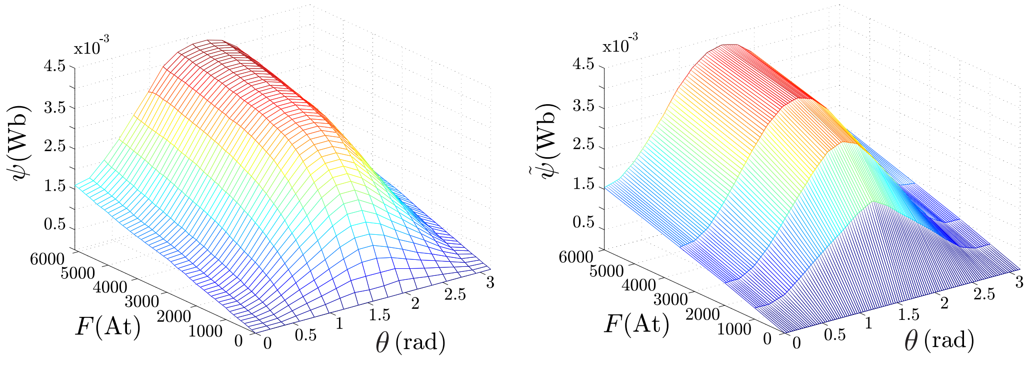

Figure 2.6: Piecewise affine function representation of the flux characteristic [3]

# Chapter 3

# SRM model characterization

As mentioned before, the flux-linkage and torque characteristics of the SRM are not linear and depend on the rotor's position and the current through the phase. Identifying these characteristics successfully is of tremendous importance to implement a model-based control strategy and to achieve the objective of operating this motor with a low torque ripple. The following sections describe the procedure for identifying these characteristics.

## 3.1 Flux characteristic

To obtain the flux-linkage characteristic, an experimental procedure was proposed in which a train of voltage pulses is applied to a motor winding by an ABC; in this case, the test was implemented on the phase $a$. The rotor was clamped in forty-four different positions in the range of $[0, 180]$ electrical degrees. Hence, due to the symmetry around the aligned position, the flux-linkage characteristic could be found for the whole electrical cycle. Fig. 3.1 shows the setup used to carry out these experiments. It was composed of an SRM connected by its shaft to a torque sensor. The shaft was locked by a clamp made by an arrangement of locking pliers and metal rods. The SRM was fed by an ABC which received its firing pulses from a Digital Control Platform (DCP). These components are detailed on Appendix A.1.

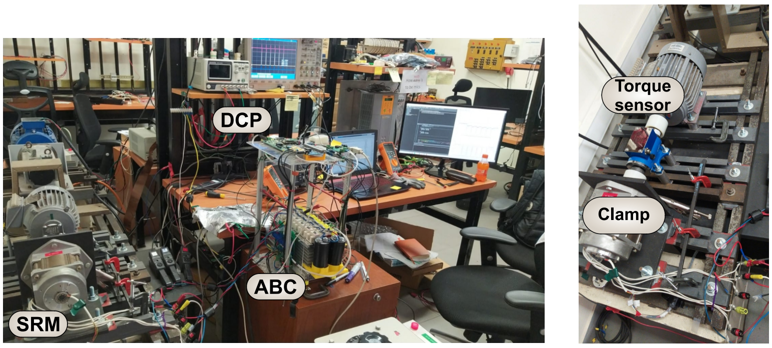

**(a)** **(b)**

Figure 3.1: Experimental setup used for flux-linkage and torque characterization. **(a)** Full view; **(b)** Top view

A train of voltage pulses was applied to increase the current up to close to 33 `A` and then reduce it until zero. The frequency of these pulses was 100 `Hz`, and the DC-link voltage was close to 50 `V` for each measurement. These experiments aim to find the flux-linkage value by knowing the current, voltage, and resistance values by integrating the flux-linkage derivative term in (2.1).

$$\psi(i, \theta = cte) = \int_0^t v(t) - Ri(t)\,dt + \psi_0 \tag{3.1}$$

As it is known, this motor does not contain permanent magnets. Thus, the flux-linkage is zero when the current is zero, which is true if non-hysteresis phenomena are considered, along with implementing the pulse train from a non-energized state, leading to $\psi_0 = 0$ `Wb`. In Fig. 3.2, two of the forty-four measurements are shown, more specifically, the ones performed in the aligned and unaligned position, which correspond to 180° and 0° respectively.

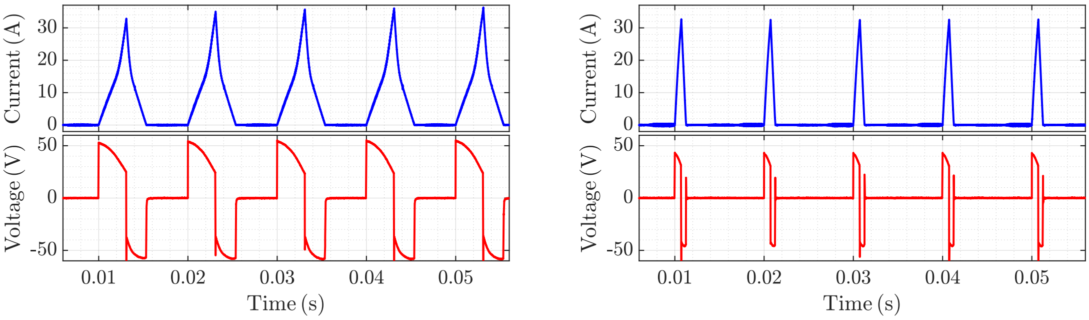

**(a)** **(b)**

Figure 3.2: Voltage/Current pulse measurements. **(a)** Aligned position; **(b)** Unaligned position

Once the flux-linkage value is known for several different currents and rotor positions, a radial basis function (RBF) approach is used to characterize the flux-linkage in specific current values and positions known in RBF as nodes. This approach considers that any given function can be approximated by a sum of radial basis functions weighted by a different parameter for each one of those functions. In this case, the flux-linkage approximation can be written as portrayed in (3.2), where $\mathcal{N}$ represent the set of nodes, $\alpha$ are the weight parameters of the RBFs, and $\Phi$ is the RBF that has as an argument an user-defined parameter $\epsilon$ multiplied by the norm of the distance between the sample points and the chosen nodes. This distance is normalized in both dimensions current and position by their maximum values $I_{max}$ and $\Theta_{max}$, which are equal to 33 `A` and 180°, respectively.

$$\hat{\psi}(i,\theta) = \sum_{n\in\mathcal{N}} \alpha_n \Phi\left(\epsilon\left|\left|\left(\frac{i-i_n}{I_{max}}\right)^2+\left(\frac{\theta-\theta_n}{\Theta_{max}}\right)^2\right|\right|\right) \tag{3.2}$$

There are several choices for the RBF, but in this work the Gaussian function is selected, therefore rewriting (3.2) into (3.3).

$$\hat{\psi}(i,\theta) = \sum_{n\in\mathcal{N}} \alpha_n \, e^{-\epsilon^2\left[\left(\frac{i-i_n}{I_{max}}\right)^2+\left(\frac{\theta-\theta_n}{\Theta_{max}}\right)^2|\right]} \tag{3.3}$$

The idea is to find the weight parameters $\alpha$ in order to turn $\hat{\psi}(i,\theta)$ into a good approximation of $\psi(i,\theta)$, so a constrained linear least-squares problem is solved using the measured flux-linkage value, as shown in (3.4). As can be observed, two constraints are set for this problem, where the first constraint assures that the flux-linkage is zero when the current is zero. The second one forces the derivative of the flux-linkageto be zero in the unaligned and unaligned positions, thus making these characteristics periodic past these values.

$$\min_{\alpha_n} \quad \frac{1}{2}\left|\left|\hat{\psi}(i,\theta)-\psi^{med}(i,\theta)\right|\right| \tag{3.4a}$$

$$\text{s.t.} \quad \hat{\psi}(0,\theta) = 0 \tag{3.4b}$$

$$\frac{d\hat{\psi}(i,\vartheta)}{d\theta} = 0 \quad , \quad \vartheta \in \{0, \Theta_{max}\} \tag{3.4c}$$

Once the function $\hat{\psi}(i,\theta)$ is obtained, the flux-linkage measurement curves for all positions are compared to the ones obtained by the proposed approximation. The comparison for nine out of the forty-four positions is displayed in Fig. 3.3.

As can be seen, the difference between the measured and estimated flux-linkage is negligible, hence validating the flux-linkage characteristic that will be used from this point forward in this

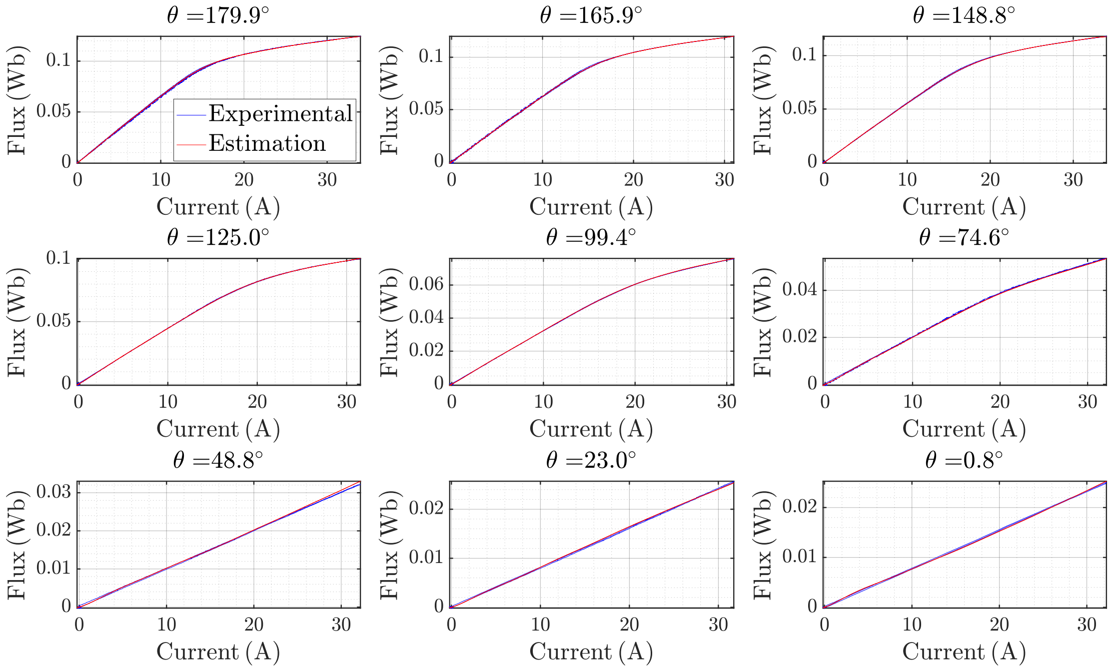

Figure 3.3: Comparison per angle

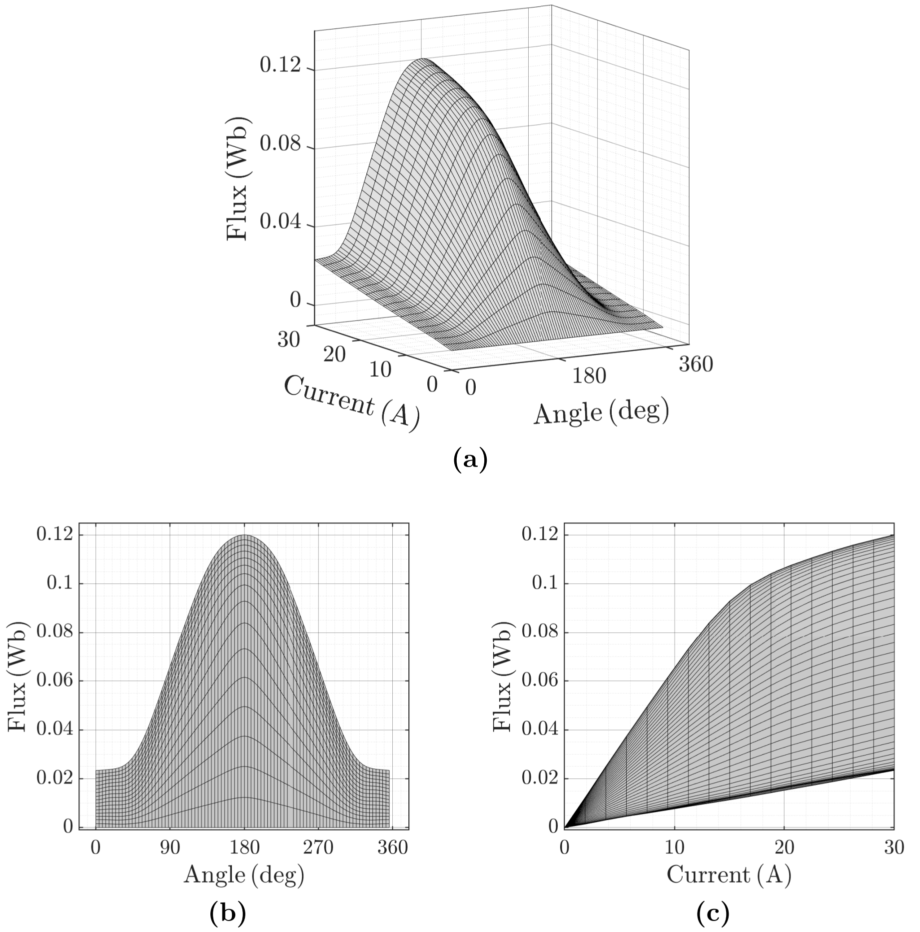

**(a)**

**(b)**

**(c)**

Figure 3.4: Flux characteristic. **(a)** 3-D view; **(b)** Angle view; **(c)** Current view

work. RBF also proved useful due to the hysteresis on the experimental flux-linkage curves, which is more easily appreciated in Fig. 3.3 when the position is closer to 180°. It can be observed how the estimated flux-linkage goes right through the middle of the hysteresis band and, therefore, successfully generalizes the flux-linkage behavior.

In Fig. 3.4 are shown multiple views of the flux-linkage characteristic, in which the electrical cycle and the current range were discretized in 90 and 17 equidistant positions, respectively. It can be observed clearly how the flux-linkage increases linearly with the current until the iron core saturates. Therefore, the flux-linkage increases at a smaller rate compared with the one present at non-saturated operation points.

## 3.2 Torque characteristic

A similar experimental procedure to the one presented in Section 3.1 was carried on to obtain the torque characteristic of the SRM. The setup was identical to the one shown in Fig. 3.1. The torque measurements were obtained for these experiments from the torque sensor described in Appendix A.2, which unfortunately had a sampling time of 16 `ms`. Thus, instead of applying a voltage pulse train, only one long pulse of 200 `ms` was applied for sixteen different positions. Due to the negligible resistance of the SRM phase, a series resistor of 2 $\Omega$ was connected to the phase $a$. Nineteen different DC-link voltage values between 0 to 60 `V` were applied in each rotor position, obtaining 304 sample points. Three of them are shown in Fig. 3.5.

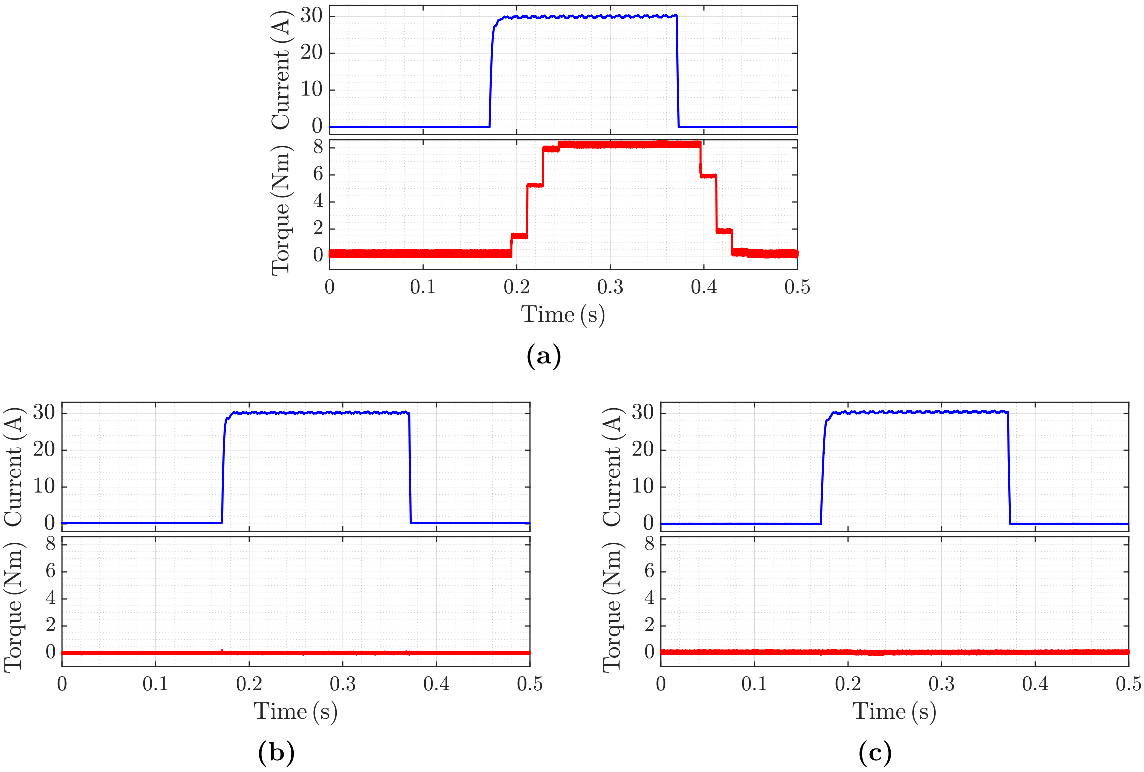

**(a)**

**(b)**

**(c)**

Figure 3.5: Torque measurements while applying current pulses. **(a)** $\theta = 99.12°$; **(b)** $\theta = 0°$; **(c)** $\theta = 180°$

It can be observed that the torque measurement signal has a discrete behaviour and is not continuous. Therefore, it is not reliable for measuring torque ripple at steady-state operation. Also, it can be noted that at the aligned and unaligned positions, the torque value is zero.

To find an approximation of the torque characteristics, a simple linear interpolation between the sample points was made. The results obtained by this procedure are shown in Fig. 3.6, where multiple views of the torque approximation are shown. In this approximation, the electrical cycle and the current range were discretized in 90 and 17 equidistant positions respectively, as well as the flux-linkage characteristics. It is worth saying that both flux-linkage and torque characteristics of the SRM have notorious resemblance with characteristics found of other SRMs in the literature, as the ones shown in Fig. 2.3.

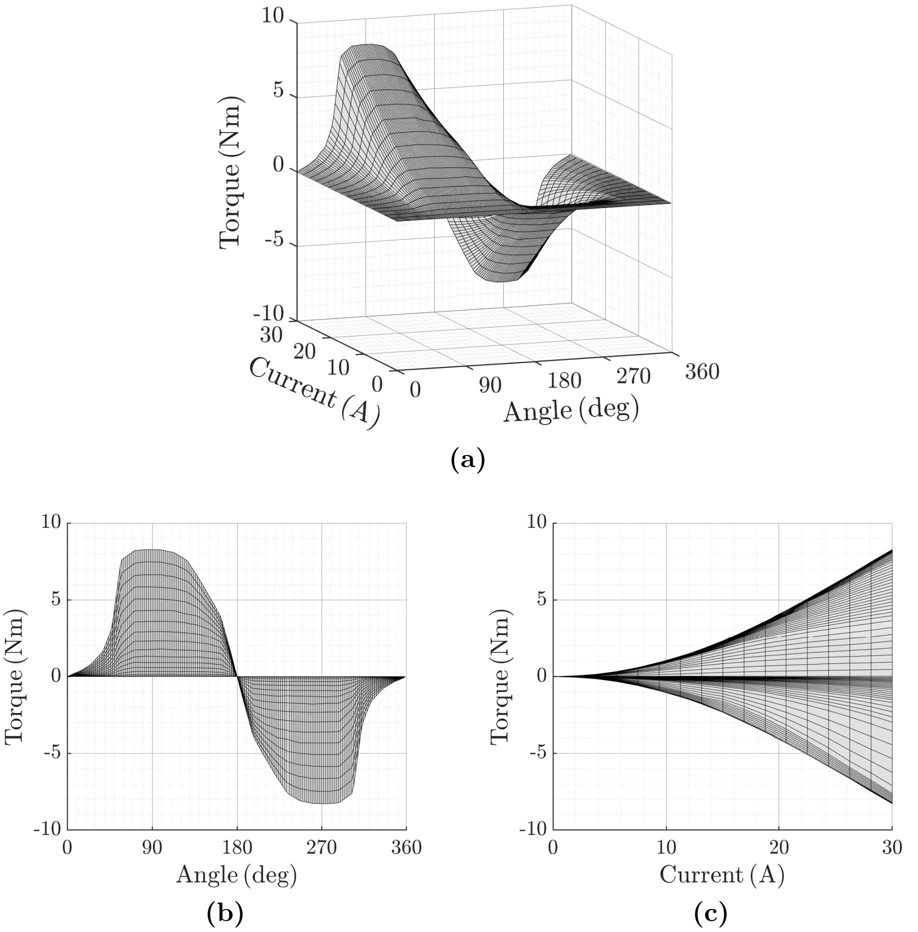

**(a)**

**(b)** **(c)**

Figure 3.6: Torque characteristic. **(a)** 3-D view; **(b)** Angle view; **(c)** Current view

# Chapter 4

# Proposed control strategy

The proposed control scheme is shown in Fig. 4.1 and consists of an outer flux reference generation layer that feds a closed-loop control stage. A more detailed explanation of this scheme is explained below.

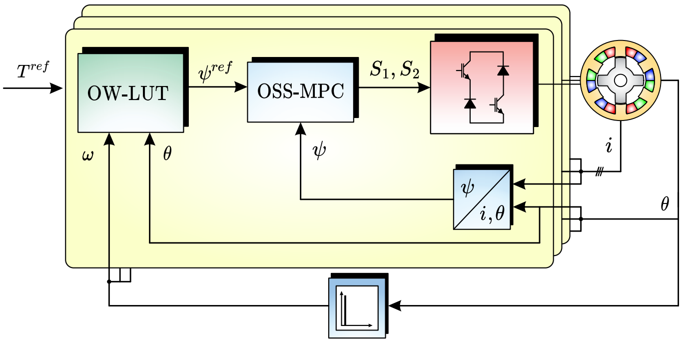

Figure 4.1: Proposed control scheme

The outer layer generates flux-linkage references to be tracked by the inner loop. This layer consists of a 3-D LUT that delivers an optimized flux-linkage pattern by knowing the machine's position, speed and reference torque. Each flux-linkage pattern is obtained offline by implementing OFWG for a given speed and torque. This layer is explained in Section 4.1.

In the inner flux-linkage control loop, the desired pattern is tracked by an OSS-MPC algorithm for each phase of the machine separately. The feedback signal needed by this block can be obtained using a flux-linkage LUT fed by the actual position and current through the phase. The reason for controlling the flux-linkage instead of the current is the simpler estimation of its derivative, which will be discussed in this chapter. This control strategy is explained in Section 4.2.

Both the optimized flux linkage patterns and the estimated flux-linkage will be obtained by using trilinear and bilinear interpolation of their respective LUT. Also, the control algorithm will be executed separetely for each phase, as depicted in Fig. 4.1, in which a three phase SRM is considered.

## 4.1 Optimal Flux Waveform Generation

In this work, the reference generation layer is built by using flux-linkage patterns computed offline by solving a modified mixed-integer quadratically constrained program (MIQCP) in which the flux and torque characteristics, along with the machine dynamics, are considered in order to minimize the total torque ripple delivered by the SRM. First, the proposed model of the optimization problem is presented, and its following proposed discretization is explained. The complete discretized optimization problem is later described in detail.

### 4.1.1 Problem formulation

The optimal flux-linkage patterns that this work proposes to compute are obtained for constant values of average torque and angular speed. By taking the last consideration into account, we will assume that the current $i$, the voltage $v$, the flux-linkage $\psi$, and the torque $T$ are $2\pi$-periodic waveforms of the position $\theta$ [3], allowing to decouple the SRM dynamic equations from the time variable $t$ and rewrite them as a function of $\theta$.

#### 4.1.1.1 Cost function

As stated previously in this work, the primary motivation of this work is to operate the SRM, minimizing both the torque ripple and the power losses. To achieve this goal, the cost function that accounts for both these objectives is defined as

$$Z_{\text{obj}}(T, i_p) = \frac{1}{2\pi}\int_0^{2\pi} (T - \bar{T})^2 \, d\theta + \lambda \sum_{p\in\mathcal{P}} \frac{1}{2\pi}\int_0^{2\pi} i_p^2 R \, d\theta \ , \tag{4.1}$$

where $\mathcal{P} := \{1, ..., N_{ph}\}$ is the set of phases of the SRM, $i_p$ is the current through the phase $p \in \mathcal{P}$, $T$ represents for the total torque output, $\bar{T}$ symbolize the average torque over one electrical cycle, $R$ is the phase resistance parameter, and $\lambda$ is a positive scalar constant. As can be observed, the first term of (4.1) represents the sum of the mean square error of the torque, and the second term represents the sum of the mean square losses of each phase.

#### 4.1.1.2 Constraints

Applying a change of variable of $\theta = \omega t$ to (2.1), and assuming a constant angular speed $\omega$, the electrical dynamic constraint of each phase is defined as

$$v_p = i_p R + \omega \frac{d\psi_p(\theta, i_p)}{d\theta} \qquad \forall p \ \in \ \mathcal{P}, \tag{4.2}$$

where $v_p$ is the voltage applied to the phase $p$, and $\psi_p(\theta, i_p)$ represents the flux-linkage of the same phase. As previously mentioned, the flux-linkage variable has a nonlinear dependency on the phase current and the motor's position. The torque generated by each phase also has a nonlinear dependency on these two variables. The total torque output is equal to the sum of each phase torque and is represented as

$$T = \sum_{p\in\mathcal{P}} T_p(\theta, i_p) \ , \tag{4.3}$$

where $T_p(\theta, i_p)$ represents the torque generated by each phase $p$. Finally, the average torque produced by the SRM over one cycle must be given by

$$\bar{T} = \frac{1}{2\pi}\int_0^{2\pi} T \, d\theta. \tag{4.4}$$

#### 4.1.1.3 Optimization model

Once the cost function and the electromechanical equations that govern the SRM are identified, the proposed optimization problem is defined as

$$\min_{T, i_p} \ Z_{\text{obj}}(T, i_p) \tag{4.5a}$$

$$\text{s.t.} \ v_p = i_p R + \omega \frac{d\psi_p(\theta, i_p)}{d\theta} \qquad \forall p \ \in \ \mathcal{P} \tag{4.5b}$$

$$T = \sum_{p\in\mathcal{P}} T_p(\theta, i_p) \tag{4.5c}$$

$$\bar{T} = \frac{1}{2\pi}\int_0^{2\pi} T \, d\theta. \tag{4.5d}$$

This problem is not simply solved due to the nonlinear characteristics of the flux-linkage and torque. Because of the complexity of identifying their functional expression, they are mainly represented as LUT approximations. In this work, the flux-linkage and torque functions will also be represented by LUTs. Considering the aforementioned, the optimization problem presented in (4.5) must be reformulated considering the now discrete nature of the flux-linkage and torque functions.

### 4.1.2 Implementation proposal

As stated previously, the optimization problem presented in (4.5) must be reformulated to consider the discrete nature of the LUTs representing the flux-linkage and torque functions. The following subsection consists of two parts. The first will explain how to approximate nonlinear functions into a set of linear and integer constraints, and the second will present the complete discrete reformulation of the original problem.

#### 4.1.2.1 Approximation of nonlinear functions

Here, a procedure is presented to approximate nonlinear functions into a set of linear and integer expressions. To be more concise, only the flux-linkage approximation procedure will be presented, but its implementation is analog to the torque function. First of all, the electrical cycle will be discretized and defined as the set $\mathcal{L} := \{1, ..., N_L\}$, where $N_L$ is the number of different angular positions in which the function is discretized. A piecewise approximation of the nonlinear function is made for each of these positions, and it will only depend on the phase current. Each piecewise approximation is discretized into the set $\mathcal{R} := \{1, ..., N_S\}$, where $N_S$ is the number of linear sections of each piecewise approximation. Taking these considerations, the flux-linkage characteristic at a given angular position $\theta_\ell$, where $\ell \in \mathcal{L}$, can be approximated as

$$\psi(\theta_\ell, i_\ell) \approx \psi_\ell(i_\ell) = a_{\ell,r} i_\ell + b_{\ell,r}, \quad \text{if } \check{\imath}_r \leq i_\ell \leq \hat{\imath}_r \tag{4.6}$$

where $a_{\ell,r}$ and $b_{\ell,r}$, with $r \in \mathcal{R}$, parametrize the affine functions, $\check{\imath}_r$ and $\hat{\imath}_r$ are the boundaries of the affine sections, and $i_\ell$ is the current at the angular position $\ell$. Considering that the newly defined piecewise-linear function will be part of the reformulation of the optimization problem presented in (4.5), a mixed-integer programming model for piecewise-linear functions [3, 55, 56] is proposed to reformulate (4.6) as a new set of constraints defined as

$$\psi_\ell = \sum_{r \in \mathcal{R}} a_{\ell,r} y_{\ell,r} + b_{\ell,r} x_{\ell,r} \qquad \forall \ell \in \mathcal{L} \tag{4.7a}$$

$$\sum_{r \in \mathcal{R}} x_{\ell,r} = 1 \qquad \forall \ell \in \mathcal{L} \tag{4.7b}$$

$$\sum_{r \in \mathcal{R}} y_{\ell,r} = i_\ell \qquad \forall \ell \in \mathcal{L} \tag{4.7c}$$

$$x_{\ell,r} \check{\imath}_r \leq y_{\ell,r} \leq x_{\ell,r} \hat{\imath}_r \qquad \forall (\ell, r) \in \mathcal{L} \times \mathcal{R}, \tag{4.7d}$$

where the additional binary variable $x_{\ell,r}$ and the continuous variable $y_{\ell,r}$ are introduced. As can be observed from (4.7a), the flux-linkage equals the sum of all the piecewise-linear function values, which is only different from zero in one section. The above is enforced by (4.7b) – (4.7d). A graphical representation of the aforementioned discretization is presented in Fig. 4.2a, in which the flux-linkage characteristic shown in Fig. 3.4 is used as an example.

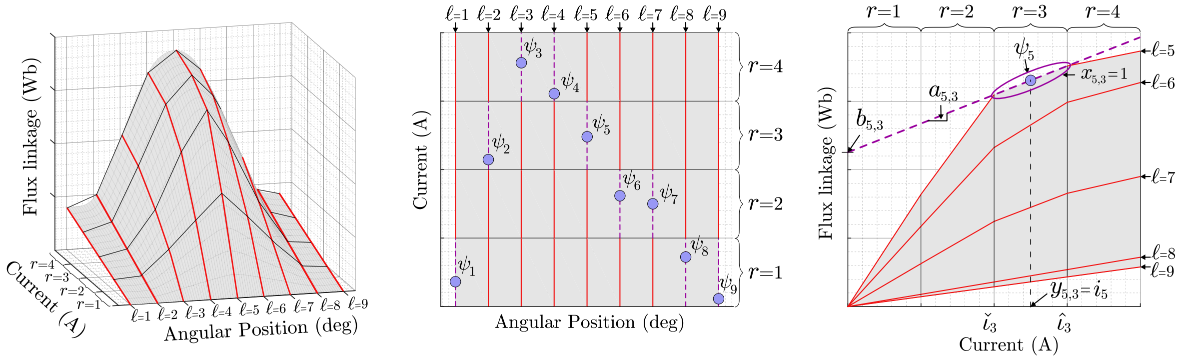

**(a)** **(b)** **(c)**

Figure 4.2: Proposed discretization of the LUTs **(b)** Full view; **(b)** Upper view; **(c)** Side view.

An upper view of Fig. 4.2a is presented in Fig. 4.2b. Here, it is shown how the flux-linkage function is discretized in $N_L = 9$ angles and also how each one of the piecewise functions is subdivided into $N_S = 4$ sections. The red and segmented purple lines represent the linear functions in which $x_{\ell,r}$ equals zero and one, respectively. It is in those last segmented sections in which the value of the flux-linkage lies. The above can also be observed in Fig. 4.2c, which shows a side view of the same flux-linkage characteristic. Here, it is presented how the flux-linkage value at position $\ell = 5$ resides at the linear function respective to the section $r = 3$. Finally, it is indicated how $x_{5,3}$ is equal to 1 and $y_{5,3}$ is equal to $i_5$, which shows an example of how the constraints (4.7b) – (4.7d) are enforced.

#### 4.1.2.2 Discrete optimization problem

Taking into consideration the optimal operation model presented in (4.5) and the mixed-integer reformulation of the nonlinear functions proposed in (4.7), the proposed optimization problem is redefined. The new formulation will also introduce new constraints proposed to meet equipment limitations and improve computation efficiency. Also, along with the condition of periodicity of the electrical and mechanical variables, it will be assumed that the electrical variables waveforms are isomorphic between phases, having a phase shift of $\frac{2\pi}{N_{ph}}$ electrical radians between them. This consideration allows to reduce the complexity of the problem and only consider the electrical variables of one phase in the optimization model. Taking all the aforementioned into account, the proposed reformulated optimization problem is defined as follows:

### Objective function

The cost function presented in (4.1) is modified and rewritten as

$$Z_{\text{obj}} = \tau^{ms} + \lambda\, i^{ms}, \tag{4.8}$$

where the first term represents the mean square torque ripple and the second term accounts for the mean square current, which is proportional to the conduction losses. It is important to notice that both components of the objective function are not directly dependent of each other. This is because even if the torque value directly depends on the current, the torque ripple is not.

### Constraints

The reformulation presented in (4.7) will model the flux-linkage nonlinear characteristic. Applying the same procedure to the torque equation presented in (4.3), the total torque output at an angle $\ell$ is defined as,

$$T_\ell = \sum_{p \in P} \sum_{r \in \mathcal{R}} m_{q(p,\ell),r}\, y_{q(p,\ell),r} + n_{q(p,\ell),r}\, x_{q(p,\ell),r} \qquad \forall \ell \;\in\; \mathcal{L}, \tag{4.9}$$

where $m_{\ell,r}$ and $n_{\ell,r}$ parametrize the torque affine piecewise function. As seen from (4.9), the total torque output variable is constructed by the sum of the torque output of all phases. Due to the isomorphism and periodicity of the variables which was referenced before, in order to obtain the torque values of the other phases, a coupling function $q(p, \ell)$ was set to replace the angle $\ell$ indexes of the piecewise function. It is mandatory to include the dynamic behavior of the electrical variables in the model, so the electrical balance equation (4.2) is reformulated for only one phase, discretized using the forward Euler method, and redefined as

$$v_\ell = R\, i_\ell + \omega \frac{\psi_{\ell+1} - \psi_\ell}{\Delta\theta} \qquad \forall \ell \;\in\; \mathcal{L}, \tag{4.10}$$

where $v_\ell$ is the applied voltage at the angle $\ell$, and $\Delta\theta$ is the angular difference between angles, which is equal to $\frac{2\pi}{N_L}$ electrical radians. Considering the periodicity of the flux-linkage applying the forward Euler method, a continuity constraint is set and denoted as

$$\psi_{N_L+1} = \psi_1. \tag{4.11}$$

As for the voltage applied to the phase, it must be bounded by the DC link voltage, which feeds the converter. The aforementioned is modeled by

$$-V_{dc} \leq v_\ell \leq V_{dc} \qquad \forall \ell \;\in\; \mathcal{L}, \tag{4.12}$$

where $V_{dc}$ is the DC link voltage. Concerning the mechanical constraints, some considerations must be made. First, the average torque output value during one electrical cycle must equal the reference torque $\bar{T}$. The above is modeled by

$$\bar{T} = \frac{1}{2\pi} \sum_{\ell \in \mathcal{L}} T_\ell \Delta\theta, \tag{4.13}$$

where the constraint (4.4) is discretized and reformulated. Among the modifications made to the original formulation, a constraint that bounds the instantaneous torque through a setting parameter $\xi$ is applied and defined as

$$\bar{T}(1-\xi) \leq T_\ell \leq \bar{T}(1+\xi) \qquad \forall \ell \;\in\; \mathcal{L}, \tag{4.14}$$

which improves both the torque solution's quality and the model's computational efficiency. The mean square torque error term defined in (4.1) is also discretized and redefined as

$$\frac{1}{2\pi} \sum_{\ell \in \mathcal{L}} \left(T_\ell - \bar{T}\right)^2 \Delta\theta \leq \tau^{ms}, \tag{4.15}$$

where $\tau^{ms}$ is an auxiliary variable that bounds the torque error. This variable is minimized in the objective function (4.8). As for the manufacturer's given limitations, two of them will be considered in the model. First, the instantaneous current should not surpass a maximum value, therefore

$$i_\ell \leq i^{max} \qquad \forall \ell \;\in\; \mathcal{L}, \tag{4.16}$$

where $i^{max}$ is the maximum instantaneous current allowed. Second, the maximum RMS current should not be surpassed; hence

$$\frac{1}{2\pi} \sum_{\ell \in \mathcal{L}} i_\ell^2 \Delta\theta \leq i^{ms} \leq \hat{I}_{\text{rms}}^2, \tag{4.17}$$

where $\hat{I}_{\text{rms}}$ is the maximum RMS current and $i^{ms}$ is an auxiliary variable which bounds the discrete approximation of the mean square current.

### Complete formulation

Once the problem and its components are defined, the formulation of the proposed MIQCP is presented in (4.31)

$$\min_{\substack{\psi, T, i, x, y,\\ v, i^{ms}, \tau^{ms}}} \quad (4.8) \tag{4.18a}$$

$$\text{s.t.} \;\; (4.7), (4.9) \text{ to } (4.17) \tag{4.18b}$$

This optimization problem can be solved by many solvers available online, such as Gurobi.

### 4.1.3 Analysis

The proposed MIQCP implementation is run considering the SRM model presented in Chapter 3, and its results are analyzed. The rest of the parameters considered to run the optimization are shown in Appendix A.1, where most correspond to the SRM nominal values.

In Fig. 4.3, the torque ripple and the RMS current values are shown when the MIQCP is run while varying the average torque and speed parameters for several $\lambda$ values. The torque ripple indicator $T_r$ corresponds to the difference between the maximum and minimum torque value and is normalized in percentage with the average torque value. The torque ripple tolerance band for this case equals ±10%. This MIQCP was solved using Gurobi Optimizer version 10.0.1.

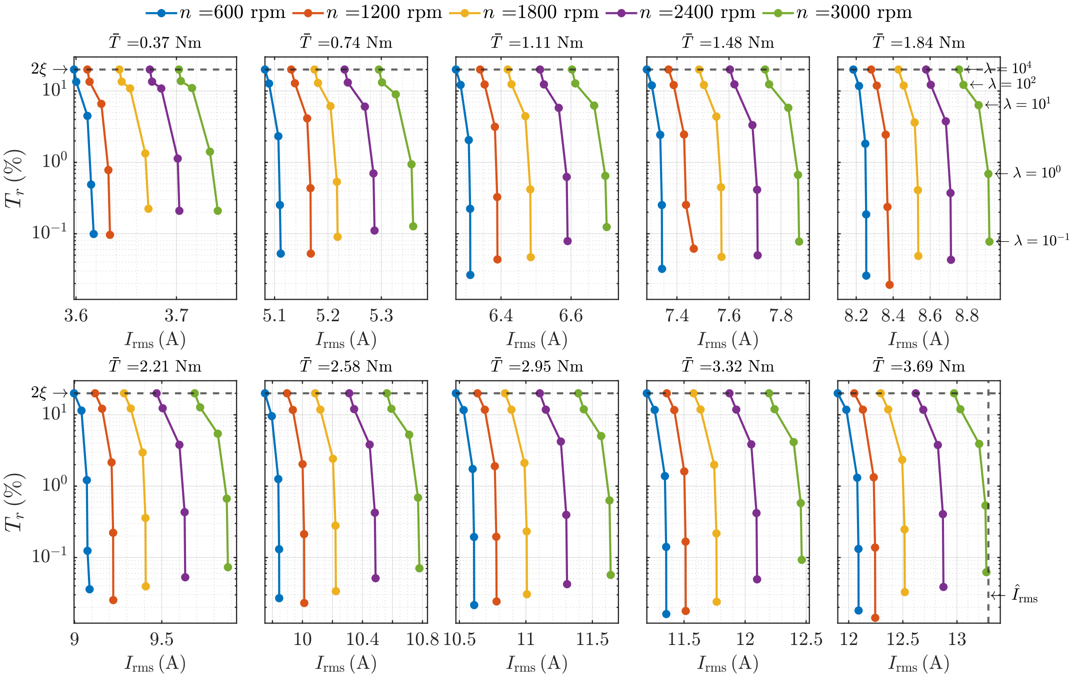

Figure 4.3: Impact on the choice of $\lambda$ for different operation points

As seen from Fig. 4.3, if $\lambda$ is increased, then $T_r$ also increases while reducing the phase current and, therefore, the losses. However, this graph shows that the current reduction is marginal concerning the torque ripple increment. Because of this reason, the flux-linkage patterns obtained for $\lambda = 10^{-1}$ are the ones considered to be implemented in this work. It is interesting to observe how the tolerance band constraint is active when the $\lambda$ value is the highest, which is logical. As for the maximum allowed RMS current constraint, it becomes close to activating at the maximum average torque and speed operation values. This observation suggests that for more demanding conditions, and without increasing the torque tolerance band or the DC-link voltage, the problem solution may not be feasible.

The waveforms obtained by running the proposed model in several operation conditions are presented in Fig. 4.4. Here, the electrical variables of the phase $a$ and the output torque are displayed. Ten cases are presented in which the average torque parameter is modified. The torque values are normalized for each case with their respective average torque. All cases consider the motor to run at a speed of 3000 `rpm`. The figure represents the average torque values as percentages of the nominal torque value of 3.69 `Nm`.

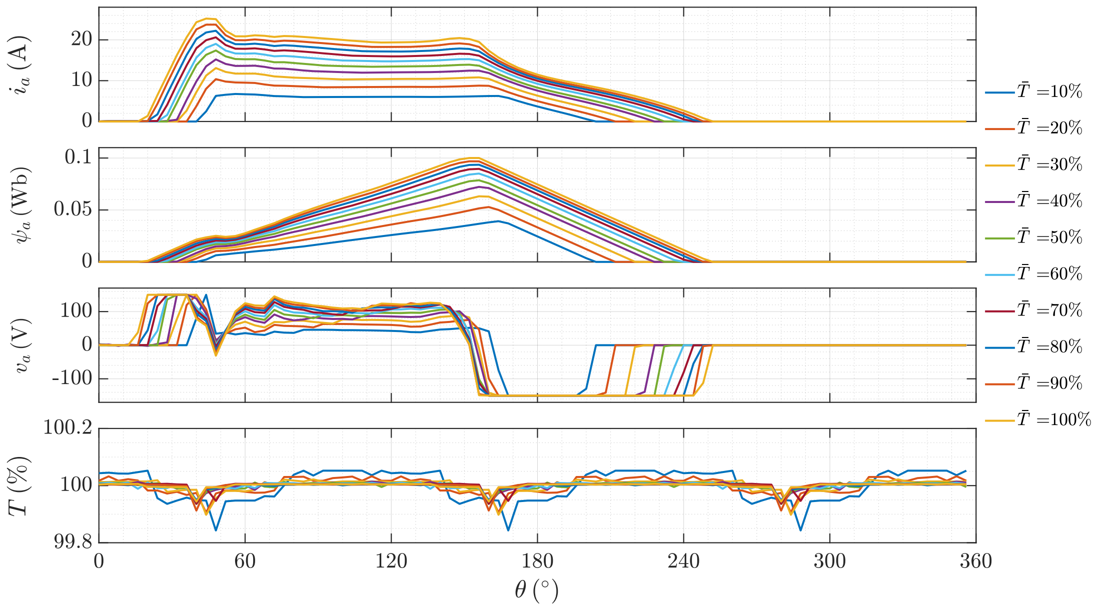

Figure 4.4: Optimal curves for $\lambda = 10^{-1}$ and $\omega = 3000$ `rpm`

It can be observed that when the average torque value that the SRM delivers rises, so do the current, flux, and voltage values. The increment of torque is not proportional to the increment in the electrical values, which can be explained because of the saturation of the iron core of the machine. Another interesting observation is that the torque ripple is minimal and quite negligible, as expected.

## 4.2 Optimal Switching Sequence Model Predictive Flux Control

This work proposes to control the flux-linkage of every phase separately by using an OSS-MPC algorithm. This section explains how this method is applied to the SRM control to improve the flux-tracking performance.

### 4.2.1 Sequences definition and state machine implementation

First, by considering the information in Table 2.1, the set of all possible output voltage vectors delivered by the ABC to the SRM is defined as

$$\mathcal{V} = \{P, O, O', N\}\,. \tag{4.19}$$

Then, by taking an approach similar to [2], the main idea of the proposed strategy is to apply the optimal sequence of voltage vectors to the phase winding during each sampling period. Considering the vectors in $\mathcal{V}$, it is possible to define all the possible three-element sequences $\mathcal{S}$ as follows:

$$\mathcal{S} = \mathcal{V}^3 \tag{4.20}$$

To simplify the real-time application of the methodology, only a subset of $\mathcal{S}$ is used for evaluation. If we assume that the sequences cannot include two or more equal vectors and must begin and end with a null vector, then the possible sequences to be applied to a phase are four. They are described in the Table 4.1 and portrayed in Fig. 4.5.

Usually, OSS-MPC strategies are implemented by delivering a duty-cycle constructed using the optimal application times to a modulation stage. This work proposes a different approach in which a state machine like the one shown in Fig. 4.5 is proposed. During one sampling period, this state machine can apply three of the four available voltage vectors depending on which of the four sequences is chosen.

Table 4.1: Preliminar sequences to use in the flux–tracking OSS-MPC.

| $Seq$ | Set of Vectors |
|---|---|
| 0 | $\{O, N, O'\}$ |
| 1 | $\{O, P, O'\}$ |
| 2 | $\{O', N, O\}$ |
| 3 | $\{O', P, O\}$ |

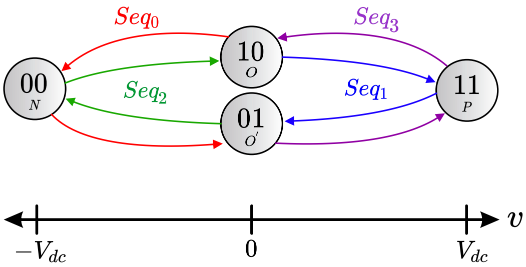

Figure 4.5: Preliminar state machine

In this work the sampling time $h$ is equal to the sum of the applied times of the different voltage vectors present in the sequence. Considering that three different voltage vectors form each sequence, $h$ is defined in (4.21) where $t_{\mathrm{I}}$, $t_{\mathrm{II}}$ and $t_{\mathrm{III}}$ correspond to the application time of the first, second and third vector of the sequence, respectively.

$$h = t_{\mathrm{I}} + t_{\mathrm{II}} + t_{\mathrm{III}} \tag{4.21}$$

Since the first and the third voltage vectors of each sequence are null, it comes naturally that the average voltage value applied to the phase does not change if the duration of $t_{\mathrm{I}}$ and $t_{\mathrm{III}}$ are equal or not, as the duration of the active voltage vector remains the same while complying with (4.21). By defining $t_{\mathrm{III}} = t_{\mathrm{I}}$ the optimization problem presented in the following subsection is simplified and becomes strictly convex. In Fig. 4.6, it can be seen that three possible switching scenarios can occur by taking this last consideration and implementing the proposed state machine. In this figure, the red line represents an active voltage vector (independent if its value is positive or negative) during one sample time.

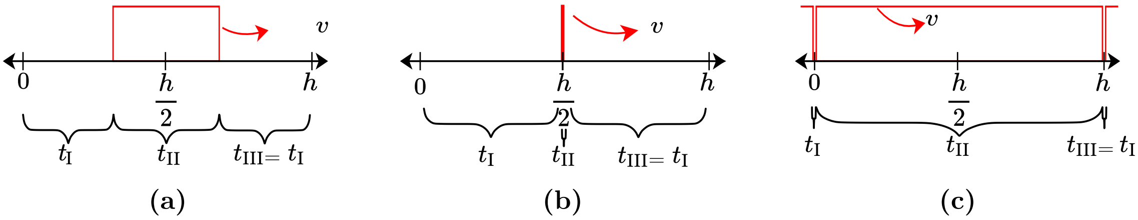

Figure 4.6: Possible switching scenarios. **(a)** Base; **(b)** $t_{\mathrm{II}} \approx 0$; **(c)** $t_{\mathrm{II}} \approx h$

In the base scenario, the active voltage vector of the sequence is applied during a time that is neither close to zero nor the whole sampling period, thus allowing minimum on and off times of the power semiconductor switches. The second and third scenarios shown in Fig. 4.6 do consider this, thus leading to unnecessary switching losses [57]. The second scenario can occur at any sampling window. However, the third case will only occur when, in the previous and/or next sampling window, the active voltage vector also has a duration near the sampling period. In order to avoid the scenarios shown in Fig. 4.6(b-c), four more sequences are added to the original subset of $\mathcal{S}$ shown in Table 4.1. Three voltage vectors also compone these new sequences, but all of their elements are equal, thus never truly switching during one sampling period. The modified subset of $\mathcal{S}$ is shown in Table 4.2, where $\sigma$ represents the switching sequence.

In order to be able to implement these new sequences, a modification is made to the initially proposed state machine to allow it to remain in active or null vectors during a whole sampling

Table 4.2: Proposed sequences to use in the flux–tracking OSS–MPC.

| $\sigma$ | Set of vectors |
|---|---|
| 0 | $\{O, N, O'\}$ |
| 1 | $\{O, P, O'\}$ |
| 2 | $\{O', N, O\}$ |
| 3 | $\{O', P, O\}$ |
| 4 | $\{O, O, O\}$ |
| 5 | $\{O', O', O'\}$ |
| 6 | $\{N, N, N\}$ |
| 7 | $\{P, P, P\}$ |

period, depending on the situation, thus reducing switching frequency and switching losses. This modified state machine is shown in Fig. 4.7.

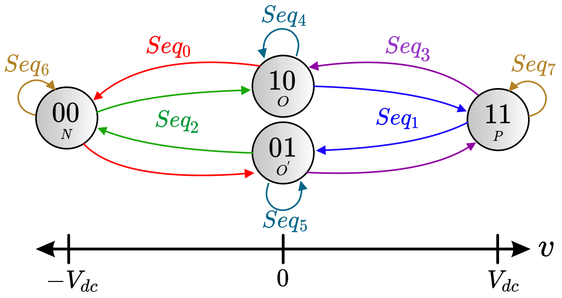

Figure 4.7: Proposed state machine

In order to reduce unnecessary switching, the modified state machine only allows the implementation of sequences that start with the same switching vector with which the previous sequence ends. However, there are exceptions with sequences 6 and 7. These sequences, which can only apply one active vector during the whole sampling period, can start after any given sequence, and any sequence can start after one of them has ended.

To reduce unnecessary switching, an user-defined constant $\varepsilon$ is proposed to limit the duration of the active state vector as shown in Fig. 4.8, where the dashed voltage vectors are avoided.

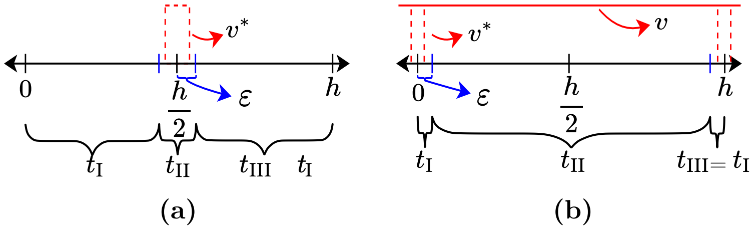

Figure 4.8: Modified switching scenarios, **(a)** Null vector; **(b)** Active vector

Taking into account (4.21) and the previously given consideration that $t_{\mathrm{I}} = t_{\mathrm{III}}$, the feasible domain $\mathcal{Z}_\sigma$ of $t_{\mathrm{I}}$ for each $\sigma$-th sequence can be defined as in (4.22)

$$\mathcal{Z}_\sigma = \begin{cases} \left[\varepsilon, \frac{h}{2} - \varepsilon\right] & , \ \sigma \in \{0, 1, 2, 3\} \\ \left\{\frac{h}{2}\right\} & , \ \sigma \in \{4, 5\} \\ \{0\} & , \ \sigma \in \{6, 7\} \end{cases} \tag{4.22}$$

It is worth saying that $\varepsilon$ could be defined higher than the minimum on and off times of the semiconductor, therefore reducing, even more, the switching frequency and the switching losses, but risking at the same time to reduce the quality delivered by the OSS-MPC. Further in this work, the impact of $\varepsilon$ for different operation points of the SRM drive will be analyzed.

### 4.2.2 Flux–tracking algorithm

Based on (2.1) and considering $v_j$ as the applied voltage vector, the derivative with respect to time of the flux-linkage of each phase $f_\psi$ can be calculated as follows:

$$f_\psi(v_j) = \frac{d\psi_j}{dt} = v_j - Ri \qquad \forall j \ \in \mathcal{V} \tag{4.23}$$

From (4.23) it is easy to see that the value of the flux-linkage variation can be obtained directly from the current and the applied voltage vector. This simple step would not be possible if the chosen control variable were the phase current because of the flux dependence shown in (2.1). In that case, it would be necessary to use a partial derivative operator to obtain the phase current gradient. By considering a sufficiently smaller sample time regarding the time constant of the system ($h \ll \frac{L}{R}$) and assuming a specific sequence for converter operation, it will be possible to evaluate the predicted flux-linkage $\hat{\psi}_{k+1}$ as,

$$\hat{\psi}_{k+1} = \psi_k + \sum_{n \in \mathcal{T}} f_{\psi_n} t_n, , \tag{4.24}$$

where $\psi_k$ is the estimated flux-linkage at instant $k$, $\mathcal{T} = \{\mathrm{I}, \mathrm{II}, \mathrm{III}\}$ is the set of indexes of the position of the vectors within a sequence, $f_{\psi_n}$ is gradient of the flux-linkage when the sequence vector in position $n$ is applied, and $t_n$ is the applied time of the vector in position $n$. From this formulation, the predicted trajectory of the flux-linkage obtained by applying an arbitrary sequence can be depicted as shown in Fig. 4.9.

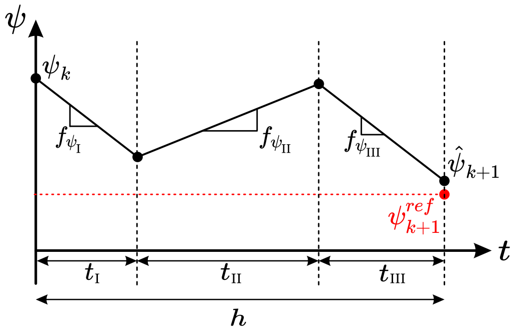

Figure 4.9: Predicted flux-linkage trajectory using the proposed OSS-MPC algorithm

The proposed OSS-MPC algorithm is designed by considering the flux-tracking error as:

$$e_{k+1} = \psi_{k+1}^{\mathrm{ref}} - \hat{\psi}_{k+1} \tag{4.25}$$

If the only objective of this flux-linkage control is to minimize the flux-tracking error, the cost function can be defined as its squared value:

$$J(t_\mathrm{I}, t_\mathrm{II}, t_\mathrm{III}) = e_{k+1}^2 \tag{4.26}$$

By replacing (4.24), (4.25) and (4.21) in (4.26), the cost function $J$ can be rewritten as:

$$J(t_\mathrm{I}) = A\ t_\mathrm{I}^2 + B\ t_\mathrm{I} + C \tag{4.27}$$

Where:

$$A = \left(f_{\psi_\mathrm{I}} + f_{\psi_\mathrm{III}} - 2f_{\psi_\mathrm{II}}\right)^2 \tag{4.28}$$

$$B = -2\left(\psi_{k+1}^{\mathrm{ref}} - \psi_k - hf_{\psi_\mathrm{II}}\right)\left(f_{\psi_\mathrm{I}} + f_{\psi_\mathrm{III}} - 2f_{\psi_\mathrm{II}}\right) \tag{4.29}$$

$$C = \left(\psi_{k+1}^{\mathrm{ref}} - \psi_k - hf_{\psi_\mathrm{II}}\right)^2 \tag{4.30}$$

In principle, this cost function must be evaluated for all $\sigma$ sequences during each sampling step and then apply the sequence with the lowest cost function. Nevertheless, as stated before, to avoid unnecessary switching, the proposed state machine only allows the implementation of sequences that start with the same switching vector with which the previous sequence ends, with the exceptions of sequences 6 and 7. Considering this, the $\sigma$ sequences to be evaluated in each sampling step depend on the previous sequence that was implemented.

With this last consideration, the optimization problem that is proposed to solve is presented in (4.31), where $\mathcal{S}^*$ represents the subset of $\mathcal{S}$ that results from reducing the quantity of possible $\sigma$ sequence candidates as a function of the sequence implemented on the previous sampling period.

$$\min_{\sigma}\big\{\min_{t_\mathrm{I}} \ J_\sigma(t_\mathrm{I})\big\} \tag{4.31a}$$

$$\text{s.t. } \ t_\mathrm{I} \in \mathcal{Z}_\sigma \tag{4.31b}$$

$$\sigma \in \mathcal{S}^* \tag{4.31c}$$

As obvious as it seems, when $\sigma \in \{4,5,6,7\}$, the value of the cost function comes directly by evaluating the only admissible value of $t_\mathrm{I}$ for that sequence (identical as it occurs for FCS-MPC). On the other hand, if $\sigma \in \{0,1,2,3\}$, then the minimum value of the cost function $J$ can be obtained by applying the first-order necessary conditions, solving the following equation.

$$\frac{dJ}{dt_\mathrm{I}} = 2A\,t_\mathrm{I} + B = 0 \tag{4.32}$$

Considering that $t_\mathrm{I}$ can only take values between $\varepsilon$ and $\frac{h}{2} - \varepsilon$, its value its equal to:

$$t_\mathrm{I} = \operatorname{mid}\left\{\varepsilon, \frac{-B}{2A}, \frac{h}{2} - \varepsilon\right\} \tag{4.33}$$

The saturation of the solution leads to suboptimal solutions. However, considering that this problem is uni-dimensional, the cost function reaches its minimum within its saturation limits if the original optimal solution is outside its allowed domain.

As will be seen further in this work, by raising the value of $\varepsilon$, it is possible to reduce the average switching frequency of the converter, but this also leads to poor flux-tracking performance and, therefore, increases the torque ripple.

# Chapter 5

# Simulation results

Once the SRM model characteristics are known, the proposed control strategy can be tested and compared with other state–of–the–art strategies by simulation. The parameters of the tested SRM are presented in Table A.5, in Appendix A.2, and the DC-link voltage of the converter is 155 `V`. The following sections will analyze and discuss the results of the simulation tests.

## 5.1 Performance metrics

The metrics to which the performance of the control strategy is evaluated must be defined before any simulation. These chosen metrics are presented and explained in this section.

- *Torque ripple* $T_r$: The difference between the maximum and minimum torque values during one electrical cycle. It is normalized by the reference torque value of the respective operation point, designated as $T^{ref}$. This metric is expressed in percentages and is defined as

  $$T_r = \frac{\hat{T} - \check{T}}{T^{ref}} \times 100, \tag{5.1}$$

  where $\hat{T}$ and $\check{T}$ represent the minimum and maximum torque respectively.

- *Torque RMSE* $T_{\text{rmse}}$: Is equal to the root–mean–square error of the torque during one electrical cycle. It is normalized by the reference torque value of the respective operation point. This metric is expressed in percentages and is given by

  $$T_{\text{rmse}} = \frac{\sqrt{\frac{1}{T_{cycle}} \int_0^{T_{cycle}} (T^{ref} - T)^2 \, dt}}{T^{ref}} \times 100, \tag{5.2}$$

  where $\mathrm{T_{cycle}}$ is the duration of the electrical cycle in seconds.

- *Average torque error* $\bar{T}_{\text{error}}$: It is equal to the reference torque value and the measured average torque. It is normalized by the reference torque value of the respective operation point. This metric is expressed in percentages and is given by

  $$\bar{T}_{\text{error}} = \frac{|T^{ref} - \bar{T}|}{T^{ref}} \times 100, \tag{5.3}$$

  where $\bar{T}$ is the measured average torque during one electrical cycle.

- *Maximum current* $\hat{I}$: Is defined as the maximum instantaneous value for the current $i$ during one electrical cycle. It is expressed in `A`.

- *RMS current* $I_{\text{rms}}$: It is the root–mean–square value of the current over one electrical cycle. This metric is expressed in `A` and is defined as

  $$I_{\text{rms}} = \sqrt{\frac{1}{T_{cycle}} \int_0^{T_{cycle}} i^2 \, dt}. \tag{5.4}$$

- *Flux-tracking error* $\psi_{\text{error}}$: Represents mean tracking error of the flux over one electrical cycle, which is normalized by the base flux-linkage value. This metric is expressed in percentages and is given by

$$\psi_{\text{error}} = \frac{1}{N_K} \sum_{k=1}^{N_K} \frac{|\psi_k^{ref} - \psi_k|}{\psi_{\text{nom}}} \times 100, \tag{5.5}$$

  where $N_K$ is the number of sampling instants during one electrical cycle, and $\psi_{\text{nom}}$ is the base value for the flux-linkage, defined in A.2.

- *Average switching frequency* $f_{\text{sw}}$: Represents the mean switching frequency of the converter. It is computed as

$$\frac{0.5\,(n_1 + n_2)}{\mathrm{T}_{\text{cycle}}}, \tag{5.6}$$

  where $n_1$ and $n_2$ are the number of switchings made by $S_1$ and $S_2$, respectively during one electrical cycle. It is expressed in `kHz`.

- *Maximum switching frequency* $\hat{f}_{\text{sw}}$: Represents the switching frequency of the semiconductor which switches the most. It is expressed in `kHz` and is computed as

$$\frac{\max\{n_1, n_2\}}{\mathrm{T}_{\text{cycle}}}. \tag{5.7}$$

## 5.2 Choice of $\varepsilon$ parameter

To be consistent with implementing the OSS-MPC flux control strategy, defining the $\varepsilon$ value that will be considered from now on is mandatory. A simulation approach is proposed to find this value, in which the motor is simulated and operated in a wide range of operation points for different values of $\varepsilon$. These simulations implement the control strategy shown in Fig. 4.1, where the proposed OFWG generates the flux reference. Three performance metrics will be analyzed to select a suitable value for $\varepsilon$, which will be used for the rest of this work.

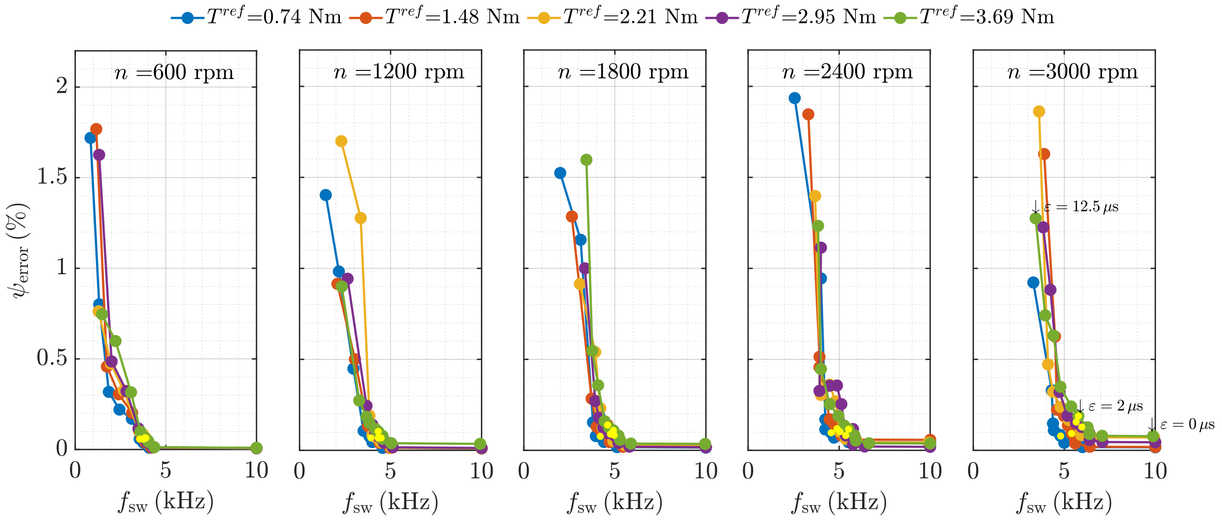

Figure 5.1: Impact on the choice of $\varepsilon$ on the flux-tracking error

Ten values between 0 and 25 times the minimum turn–off time ($t_{\text{off}} = 0.5\ \mu\text{s}$) of the semiconductor that is used in the experimental setup (shown in Appendix A.2) are tested for $\varepsilon$. The sampling frequency $f_{\text{sample}}$ for each simulation is 20 `kHz`. In Fig. 5.1 and Fig. 5.2, the flux-tracking error and the torque ripple, respectively, are compared with the average switching frequency $f_{\text{sw}}$.

It can be seen that $f_{\text{sw}}$ reduces while $\varepsilon$ increases, but at the same time, this leads to a reduction of the control tracking capabilities, and therefore the quality of the torque is worsened. Nonetheless, there are some values for $\varepsilon$ on which the switching frequency reduces considerably, but the torque ripple and flux-tracking error remain low. One of these values is chosen, more specifically

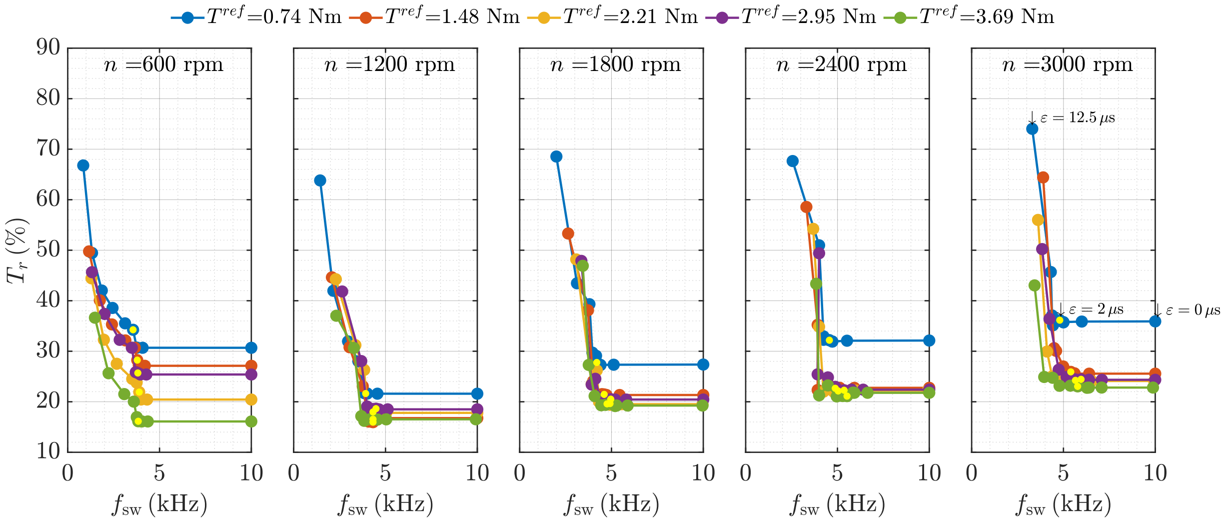

Figure 5.2: Impact on the choice of $\varepsilon$ on the torque ripple

$\varepsilon = 4 \times t_{\text{off}} = 2\,\mu$s, represented by a yellow dot in the above figures. It can be observed how a given $\varepsilon = 0\,\mu$s, the frequency remains at 10 kHz. Hence, the OSS-MPC behaves as a DBPC, which makes sense because no active or null vectors can occur during a whole sampling period, and at every sampling window, two switches will always change their state. In other words, if $\varepsilon$ is null, no sequences from 4 to 7 can occur.

## 5.3 Reference performance

In this section, the proposed reference generation strategy OFWG will be simulated and compared with the TSF approach presented in [9] in several operating conditions. The TSF used in this work is the cubic TSF, where the turn-on, turn-off, and overlap angle are computed offline by using a genetic algorithm. As in Section 5.2, the sampling frequency is 20 kHz. Also, in these simulations, the flux-tracking control algorithm implemented is the proposed OSS-MPC. The metrics values for 25 different operating conditions are shown from Table A.6 to Table A.11, on Appendix A. Also, these metrics' mean and standard deviation values are displayed in Table 5.1.

Table 5.1: Mean performance metrics. Reference generation comparison.

| Metric | Mean | | Standard deviation | |
|---|---|---|---|---|
| | OFWG | TSF | OFWG | TSF |
| $T_r$ (%) | 23.2 | 27.4 | 5.3 | 13.6 |
| $T_{\text{rmse}}$ (%) | 3.2 | 4.5 | 0.6 | 2.4 |
| $\bar{T}_{\text{error}}$ (%) | 0.4 | 1.1 | 0.2 | 1.5 |
| $\hat{I}$ (A) | 18.3 | 23.9 | 5.4 | 4.7 |
| $I_{\text{rms}}$ (A) | 9.2 | 10.1 | 2.7 | 2.2 |
| $\psi_{\text{error}}$ (%) | 0.09 | 4.28 | 0.03 | 5.5 |

It can be seen how the proposed OFWG outperforms the TSF approach in every performance metric mean value. Also, the standard deviations of these metrics reflect how these indicators are consistent within the whole operating range when OFWG is used, which does not occur when using TSF. Observing the mean value of the flux-tracking error metric becomes interesting, which is significantly higher for TSF by being 47.5 times higher than the one obtained by OFWG. The previous can be explained since TSF does not consider the electrical dynamics of the motor, which OFWG does. This effect can also be observed in Fig. 5.3, where the flux, current, and torque waveforms are shown for an arbitrary speed and full load condition. High values of flux-tracking error can lead to what can be seen with the average torque error metric, which is higher at more demanding conditions because the control algorithm cannot follow the reference. Therefore, the motor does not deliver the desired average torque.

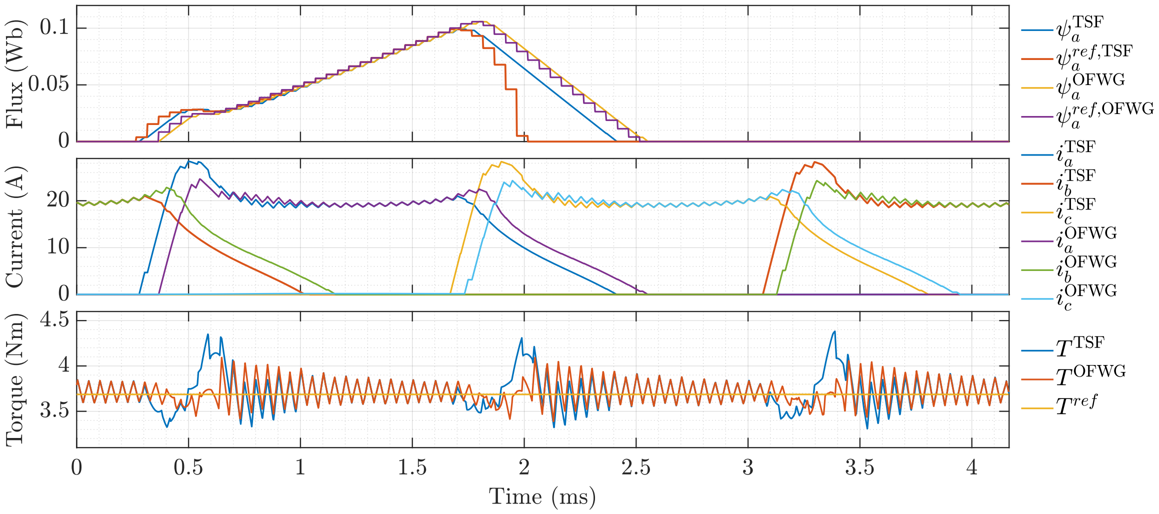

Figure 5.3: Waveforms comparison at $T^{ref} = 3.69\,\mathrm{Nm}$ and $n = 1800$ rpm

Among the reasons why OFWG surpasses TSF in most metrics is because this approach considers the flux and torque characteristics of the machine as well as its electrical dynamic. Also, the TSF approach solves an unconstrained optimization problem in which the torque ripple metric does not appear in the cost function because only the RMS current and a flux rate–of–change approximation are considered. Additionally, this approach does not guarantee the optimality of the solutions since it uses genetic algorithms to find the turn-on, turn-off, and overlap angle. At some operating points, TSF has a lower torque ripple than OFWG because the proposed MIQCP used to obtain the optimal flux patterns discretized the electrical cycle in 90 positions in which the motor dynamics were approximated and not exact. These considerations lead to not obtaining exactly the expected torque output. Nonetheless, considering the whole operation range, the OFWG delivers 4.2 % less torque ripple than TSF, validating the proposed approach. Taking all of this into consideration, the proposed OFWG outperforms TSF when generating flux-linkage references. Torque ripple is globally reduced, and the flux-linkage patterns that it generates can be tracked without practically any errors, which does not occur with TSF.

## 5.4 Flux control performance

In this section, the proposed OSS–MPC flux-tracking control strategy will be simulated and compared with the FCS-MPC approach presented in [11] and the DBPC approach presented in [25]. Five different metrics are considered to evaluate each control strategy with a sampling frequency of 20 `kHz` and an extra case in which the FCS-MPC strategy is implemented at a sampling frequency of 100 `kHz`. This last case is implemented to perform a comparison between FCS-MPC and OSS-MPC at similar average switching frequency conditions. The metrics values for 25 different operating conditions are shown from Table A.12 to Table A.16, on Appendix A. Also, these metrics' mean and standard deviation values are displayed in Table 5.2.

Table 5.2: Mean performance metrics. Flux control comparison.

| Metric | Mean | | | | Standard deviation | | | |
|---|---|---|---|---|---|---|---|---|
| | OSS | DB | FCS | $\mathrm{FCS}_{100\mathrm{k}}$ | OSS | DB | FCS | $\mathrm{FCS}_{100\mathrm{k}}$ |
| $T_r$ (%) | 23.2 | 22.9 | 79.8 | 20.1 | 5.3 | 4.7 | 17.5 | 6.6 |
| $T_{\mathrm{rmse}}$ (%) | 3.2 | 3.2 | 11.5 | 2.7 | 0.6 | 0.6 | 2.8 | 0.7 |
| $f_{\mathrm{sw}}$ (`kHz`) | 4.7 | 10.0 | 1.2 | 5.2 | 0.7 | 0.0 | 0.4 | 1.7 |
| $\hat{f}_{\mathrm{sw}}$ (`kHz`) | 4.7 | 10.0 | 2.1 | 9.5 | 0.7 | 0.0 | 0.8 | 3.2 |
| $\psi_{\mathrm{error}}$ (%) | 0.09 | 0.1 | 2.85 | 0.55 | 0.0 | 0.0 | 1.1 | 0.2 |

Regarding the mean of the torque ripple, it can be observed how both the DBPC and OSS-MPC achieve low values, which they reach by having low tracking error and, therefore, successfully following the flux reference. The significant difference between these strategies is the average and maximum switching frequency, which are considerably higher for DBPC by more than double that obtained when using OSS-MPC. The previous proves that the proposed strategy is superior in avoiding switching losses. As for the mean and standard deviation of the rest of the metrics, the two strategies perform very similarly. Fig. 5.4 and Fig. 5.5 show the flux, current, and torque waveforms, and also the switching of the two switches per phase while controlling with OSS-MPC and DBPC, respectively. In these figures and the next ones, the equivalent current associated with the flux-linkage reference will be presented as $i^{ref}$.

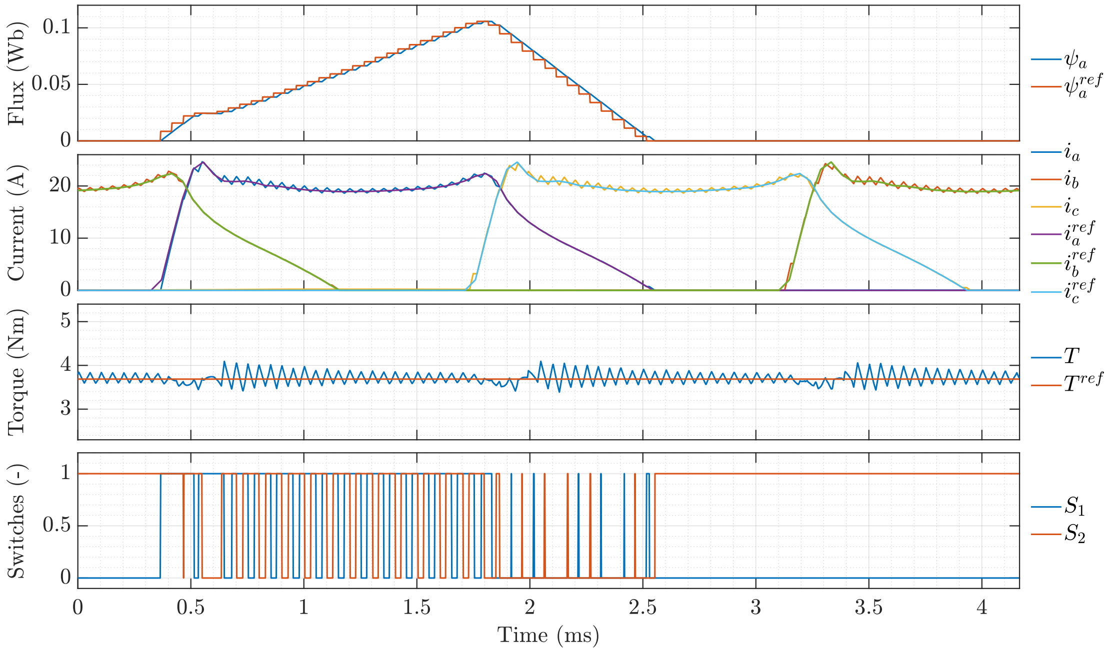

Figure 5.4: Waveforms controlling with OSS-MPC at $T^{ref} = 3.69\,\text{Nm}$ and $n = 1800\,\text{rpm}$

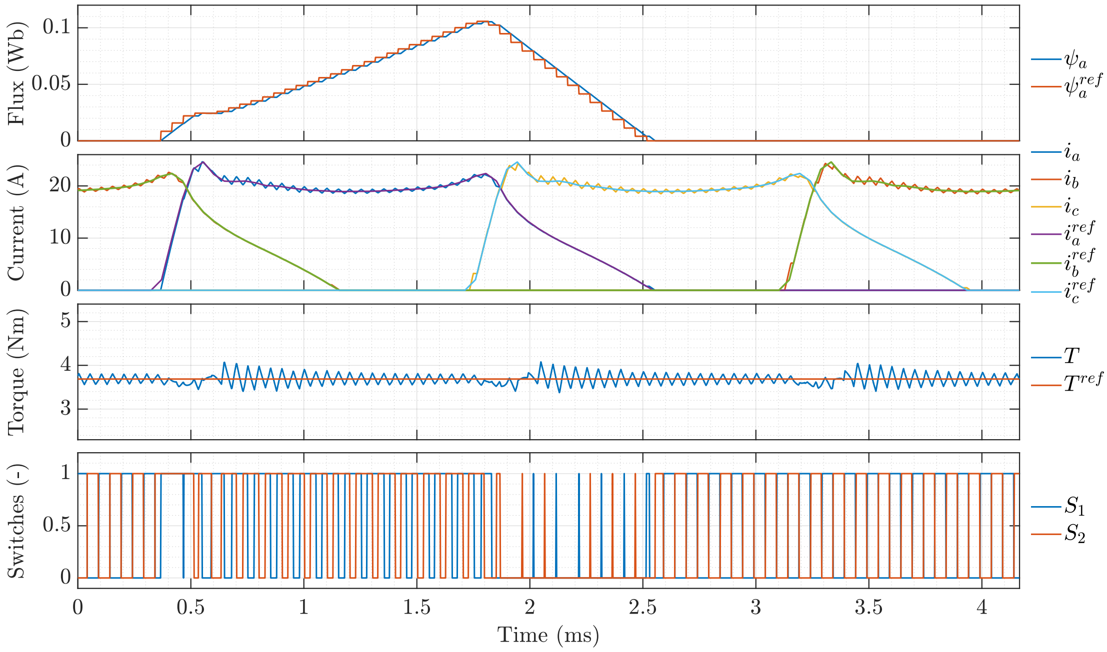

Figure 5.5: Waveforms controlling with DBPC at $T^{ref} = 3.69\,\text{Nm}$ and $n = 1800\,\text{rpm}$

As for the FCS-MPC, this strategy underperforms in every metric mean except for the average and maximum switching frequency when having a sampling frequency of 20 `kHz`. This occurs because it only applies one voltage vector during one sampling period, unlike the rest of the strategies, which apply three. In order to make a fair comparison between OSS-MPC and FCS-MPC in terms of similar average switching frequencies, the FCS-MPC strategy is also analyzed at a sampling frequency of 100 `kHz`, which is intractable in real time using commercial control platforms. This last case reaches comparable torque ripple and average switching frequency values with respect to OSS-MPC at 20 `kHz`. However, the flux-tracking error and the maximum switching frequency are way higher than the ones obtained by the proposed approach. This last weakness of the FCS-MPC control strategy proposed in [11] is because only one zero voltage state can be applied from the two available, leading to an enormous difference in switching frequency between the two switches per phase. This situation can be observed in Fig. 5.6, where the same variables shown in Fig. 5.4 and Fig. 5.5 are displayed, where is clearly shown how one of the switches makes most of the switching and the other one only switches once. Under these circumstances, the lifetime of each phase converter is expected to be strongly impacted and reduced due to the overuse of one of the semiconductors. Finally, when compared to FCS-MPC, the proposed OSS-MPC operates with more consistent average and switching frequencies, as can be observed by their standard deviations.

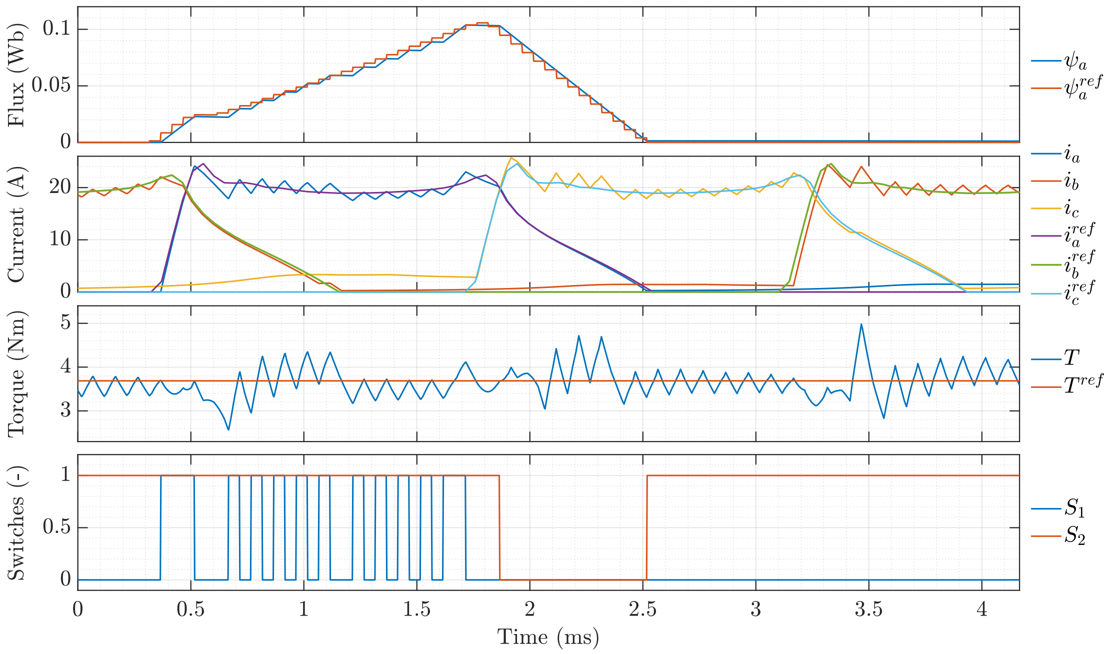

Figure 5.6: Waveforms controlling with FCS-MPC at $T^{ref} = 3.69\,\mathrm{Nm}$ and $n = 1800\,\mathrm{rpm}$

It becomes clear that the proposed OSS-MPC strategy outperforms both FCS-MPC and DBPC when controlling the flux–linkage of the motor. Both torque ripple and switching frequency values are kept low while not sacrificing the other, as with the FCS-MPC and DBPC. Therefore, the use of the proposed control strategy is validated and fulfills the objective of this work.

## 5.5 Simulated performance comparison

Finally, the mean performance metrics of reference generation and flux control stages are analyzed in Sections 5.3 and 5.4. Hence, a graphical representation of the information provided by Table 5.1 Table 5.2 is shown in Fig. 5.7.

As for the reference generation strategies, Fig. 5.7a clearly shows how OFWG is superior to TSF in every metric, as observed in Section 5.3. Both torque ripple and torque RMS error are reduced, delivering good-quality torque output while simultaneously reducing current losses, all accomplished by the tracking capability of the references. Interestingly, the torque ripple obtained while considering TSF references does not reach significant levels, despite the substantial flux-tracking error. The previous can be explained because the flux-tracking error gets higher for TSF

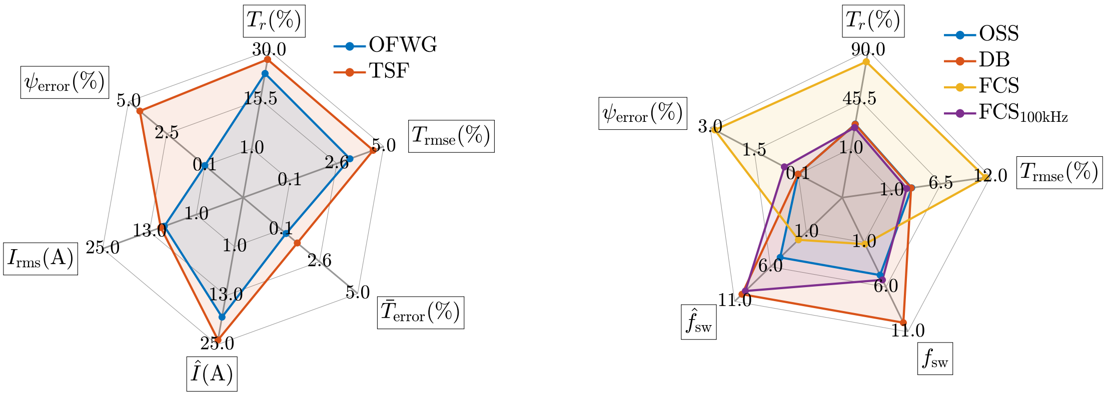

**(a)** **(b)**

Figure 5.7: Mean performance metrics comparison. **(a)** Reference generation; **(b)** Flux-tracking.

references when the phase is demagnetizing, and the current is small, as portrayed in Fig. 5.3. Therefore, even if the flux-tracking error is high in these instants, its impact on the output torque is reduced, considering that for small currents circulating, small torque is delivered.

Regarding the flux-tracking strategies, Fig. 5.7b demonstrates how OSS-MPC surpasses DBPC and FCS-MPC by maintaining a balance between flux-tracking error, torque ripple torque RMS error with the operation switching frequency. It becomes clear how DBPC achieves similar torque ripple and flux-tracking performance by switching almost double than OSS-MPC. It also becomes clear how FCS-MPC performs poorly in exchange for a reduced and unbalanced switching frequency, and the only way for it to perform similarly to OSS-MPC is to increase its sampling frequency five times, reaching 100 `kHz`. Even if the torque ripple and flux-tracking are similar to OSS-MPC at this sampling rate, the unbalanced switching caused by FCS-MPC leads to more than double the switching frequency of the switch that switches the most.

Considering all the simulations, their performance metrics, and analysis, it is computationally confirmed that the complete proposed control strategy composed of a reference generation stage and a flux-tracking control loop fulfills the objective of reducing the torque ripple of the SRM while simultaneously reducing losses. Each component of the complete strategy is also proven to surpass other state-of-the-art techniques, proving the control proposal's value.

# Chapter 6

# Experimental validation

This chapter implements the proposed control strategy in an experimental setup. At the same time, other state-of-the-art strategies are also implemented and compared with the strategy proposed in this work. Finally, some maneuvers with the SRM drive are shown to appreciate the behavior of the proposed strategy during transients and other operation points. The results obtained are discussed and evaluated in the following sections.

## 6.1 Experimental setup

The setup that was built to implement the proposed strategy is shown in Fig. 6.1, and it comprises the following:

- A 2.32 `kW` SRM is used as a motor, and an external speed control loop is added to the proposed scheme shown in Fig. 4.1. The outcome of the previous is the control scheme displayed in Fig. 6.2, in which the PI controller is simplified but is later on detailed in this section. The nominal values of the SRM are specified in Table A.5, in Appendix A.2.

- To implement a torque load to the SRM, a 2.23 `kW` induction machine (IM) is connected to his shaft. This IM is operated as a regenerative brake controlled by a Parker AC Drive, which carries out torque control. The torque sensor is not used actively in these experiments due to its low accuracy at high speeds. The nominal values of the IM are specified in Table A.4, in Appendix A.2.

- The IM works as a regenerative brake; hence, the energy transmitted from SRM flows to the IM and then it flows to the DC-link of the AC Drive. This converter does not allow four-quadrant operation; therefore, the DC-link voltage rises. To protect the equipment, an 87 Ω resistor is connected to the DC-bus in series with an IGBT that discharges the drive's capacitors when their voltage value exceeds 740 `V`. The control of this braking scheme is integrated into the capabilities of the AC Drive.

- Each one of the three phases of the SRM is connected to an ABC built of diodes and IGBTs. The ABCs are fed by a DC-link composed of two series capacitors of 3000 $\mu$`F` each. This DC-link is connected to the output of a diode three-phase rectifier, which is fed by a Variac. The voltage value of the DC-link is set as 155 `V` for each experiment, as done in the simulations presented in Chapter 5.

- A DCP called BRAIn performs the control of the SRM. This device combines a DSP and FPGA, whose models are Texas Instrument TMS320C6748 and Xilinx XC7A35T, respectively. The control strategy is programmed in the BRAIn's DSP using the Code Composer Studio v3.1 program. The sampling frequency of every experiment is set at 20 `kHz`.

- The SRM position will be measured by a Tamagawa TS2224N14E102 resolver, whose analog signals are converted to digital using a resolver-to-digital converter ADDI-DATA MSX-RDC-17. The digital signals are then sent to the DCP.

- The torque measurements will be estimated from the measured position and currents and using the torque characteristic obtained in Chapter 3. This is because the torque sensor only measures steady-state torque.

All of the mentioned components are described in detail in Appendix A.2.

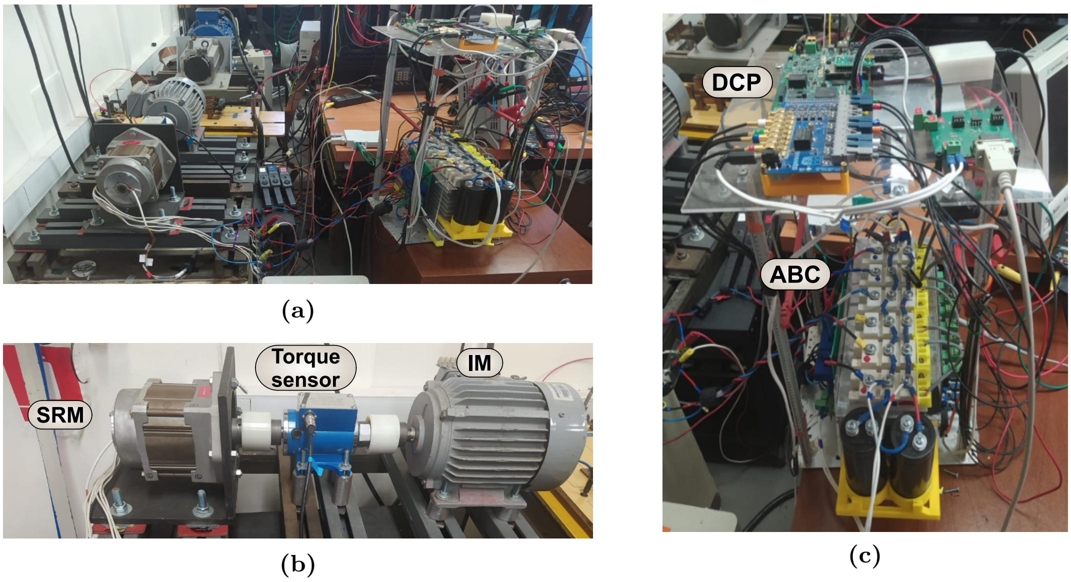

(a)

(b)

(c)

Figure 6.1: Complete Setup. (a) Full view (b) Motor setup (c) Converter with digital control platform.

### 6.1.1 Speed loop

As it was said earlier in this section, the SRM is controlled with an external speed control loop as the one shown in Fig. 6.2. The PI controller is tuned by only considering the setup inertia as the plant to be controlled, neglecting the dynamics of the flux control loop for being considerably small compared to the mechanical dynamics given by the inertia of the setup, which is $J = 0.0014$ `kg·m`$^2$. While implementing the first experiments, it was observed that the speed signal had a superposed oscillatory signal of 100 `Hz` when the motor ran at the maximum speed considered to be experimentally implemented, which was 3000 `rpm`. Above this speed, no optimal flux patterns were computed and added to the control due to the memory limitations of the DSP.

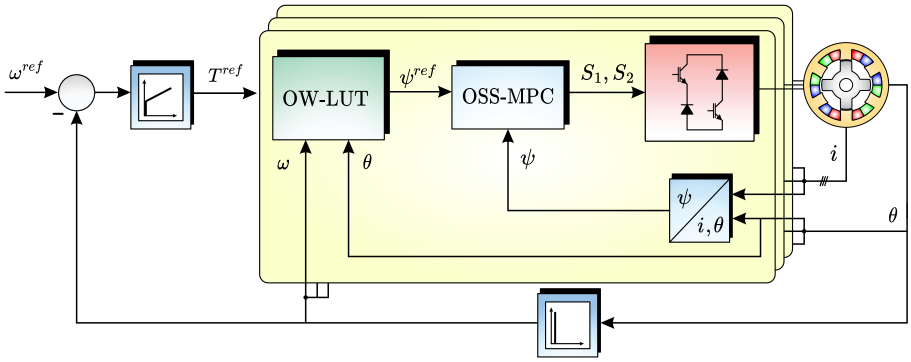

Figure 6.2: Simplified experimental control scheme

Returning to the oscillatory signal superposed to the speed, it seemed to arise from an eccentricity of the resolver and/or a non-optimal mechanical alignment of the machines. Measures were taken to overcome this, reducing the amplitude of this signal without completely eradicating it, which surpassed the current abilities of this work's author. The oscillatory signal translated to an oscillatory error that the PI tries to compensate for, replicating those same oscillations to the reference torque. Because of this, a modification to the speed loop is implemented and shown in Fig. 6.3, in which a filter named Filter N°1 is disposed before the flux control loop and after the PI controller. This filter has a time constant of 0.0318 `s`, reducing the amplitude of the 100 `Hz` signal to a 5% of its original value. As said before, if the flux control loop dynamic behavior is reduced to only the machine's inertia, the equivalent plant to be controlled by the PI controller is the product between a first-order function and an integrator. Therefore, to have a fast control response that reaches steady-state as fast as possible, the PI controller is obtained by adjusting it according to the optimization as a function of the symmetry technique proposed in [58]. The implemented PI is the following:

$$C(z) = 0.021882\frac{(z-0.9996)}{z-1} \tag{6.1}$$

Due to the considerable overshoot of the initial response of a closed loop optimized as a function of the symmetry, a reference smoothing function named Filter N°2 is set before the reference command and before the reference error computation. This filter consists of a first-order function, with a time constant of four times the constant of Filter N°1, as is also stated in [58].

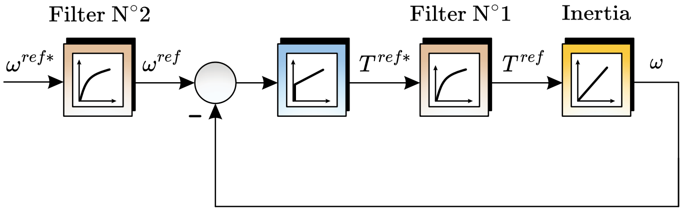

Figure 6.3: Proposed outer speed control optimizing with respect to the symmetry and adding smoothing of the reference

The modified speed control loop with its resulting bandwidth provides a steady speed and torque operation as needed to perform the experiments presented in this chapter. The step response and the bode diagram of the speed control loop are shown in Fig. 6.4, where it can be seen how low the control bandwidth is and how much time the step response takes compared with usual speed control schemes.

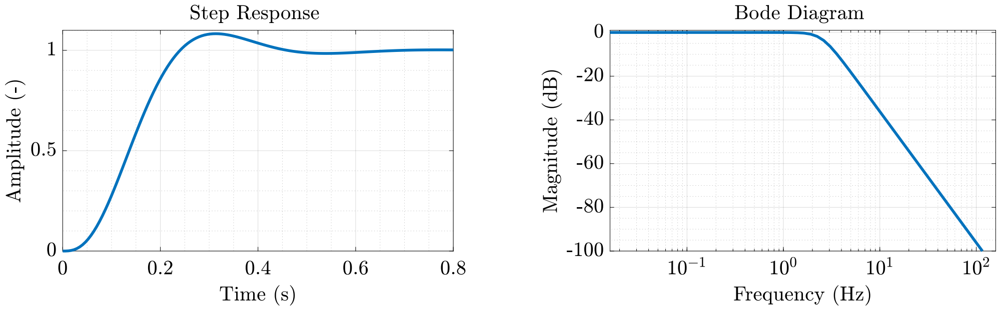

Figure 6.4: Step response and Bode diagram of the speed control loop

## 6.2 Full strategy implementation

To validate the proposed strategy, the chosen operation point for the SRM drive is to run at a speed of $n = 600$ `rpm` and with a load torque of close to the motor's nominal value of $T^{ref} = 3.69$ `Nm`. Both speed reference and torque load remain constant during the whole time. These experiments are valuable for assessing the stationary and dynamic behavior of the flux-tracking control loop because the flux-linkage reference is variable during each electrical cycle, even if the operation point is stationary. The operation point is chosen considering the actual position measurement limitations, which do not yet allow precisely estimating the position at high speeds; therefore, the minimum speed with which the optimal flux patterns were computed is selected. On the other hand, the nominal torque load is selected since this value is within the operational limits of the Parker drive and the load induction machine. The experimental waveforms of the full control strategy, which implements both the OFWG references and the OSS-MPC flux-tracking algorithm, are shown in Fig. 6.5.

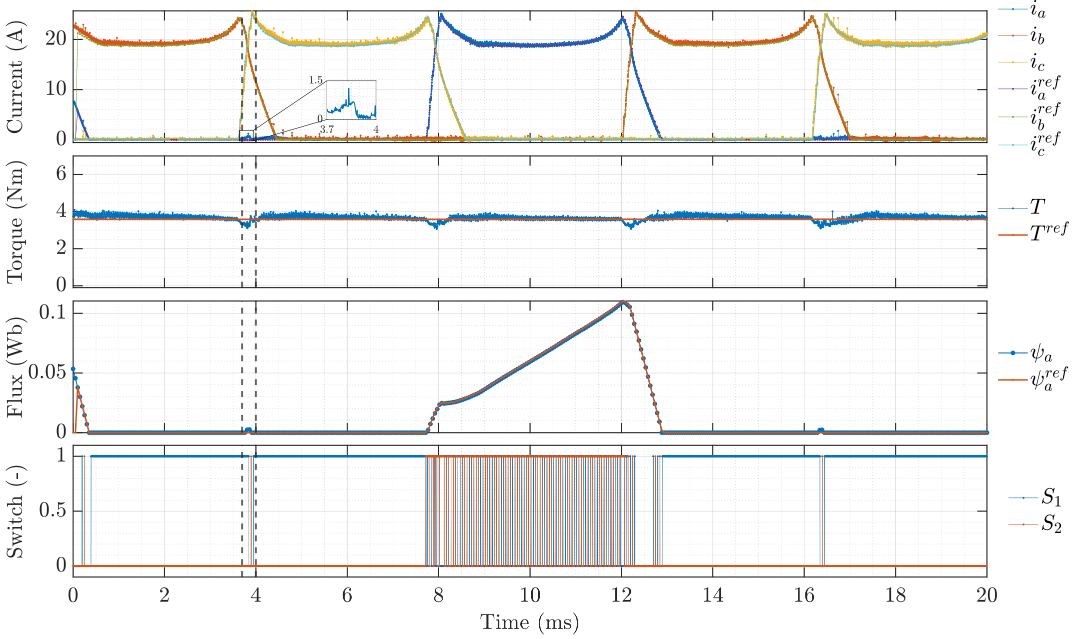

Figure 6.5: Experimental waveforms tracking OFWG references at $T^{ref} = 3.64$ `Nm` and $n = 600$ `rpm`

As expected, the flux-tracking is performed fairly and without any visible errors, thus leading to currents that are identical to those obtained if the reference flux were circulating through the phase. This fine flux-tracking produces phase currents that generate a torque output with a minimal ripple. The flux-linkage reference could be tracked since the OFWG references contemplate the motor dynamics. The slight torque ripple can be explained once again by considering that the discretization of the electrical cycle used to obtain the optimal flux patterns is not exact. On the other hand, the converter does not apply unnecessary switches when the flux references and measurements are zero, as expected and seen in the simulations. It is interesting to see how the current on phase $a$ increases when the currents on the other phases change rapidly, even if the applied voltage to phase $a$ is zero. The previous can be explained by some inherent mutual inductance phenomena between phases, which was neglected in the simulations and control proposal. The flux controller observes this rapid change in the phase $a$ current and then applies a negative voltage to return its value to zero.

## 6.3 TSF implementation

As it was done also in simulation, the reference generation technique OFWG is compared with the references obtained using TSF. The same cubic TSF used in simulation with the same turn-on and turn-off angles are considered in an experimental implementation, in which the SRM drive is run at the same conditions that the proposed implementation was in Section 6.2. The proposed OSS-MPC is the flux-tracking algorithm that is considered to track the TSF references. The experimental waveforms of this implementation are shown in Fig. 6.6.

It can be observed that the flux-tracking behaves well within the voltage limitations but worsens once they are reached. This means that the flux-tracking capability of the given TSF references is not enough to be tracked considering a DC-link of 150 `V`. The instant on which the flux cannot track its reference is where the torque error happens to increase, hence proving the limitations of the TSF by not considering the model of the motor. Nonetheless, the torque ripple is relatively small, as was expected by observing the performance metrics obtained by simulation at this operation point shown in Table A.6. Finally, it is interesting to notice how a negative voltage vector is applied when the current in phase $a$ increases due to the mutual induction effect between phases, as in Section 6.2.

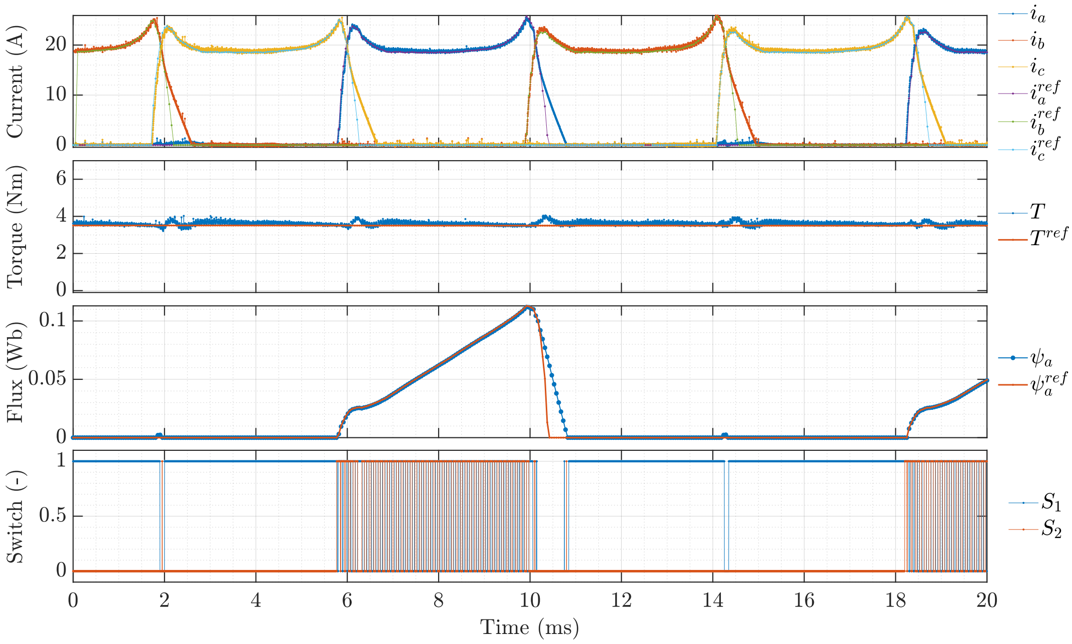

Figure 6.6: Experimental waveforms tracking TSF references at $T^{ref} = 3.67\,\mathtt{Nm}$ and $n = 600$ `rpm`

## 6.4 FCS-MPC and DBPC implementation

The state-of-the-art flux control algorithms with which the proposed OSS-MPC was compared in the simulation chapter are also implemented experimentally to analyze and discuss their differences with the proposed flux control algorithm. Both FCS-MPC and DBPC techniques track flux-linkage references generated by the proposed OFWG. First, the DBPC experimental behavior is analyzed by observing the waveforms presented in Fig. 6.7.

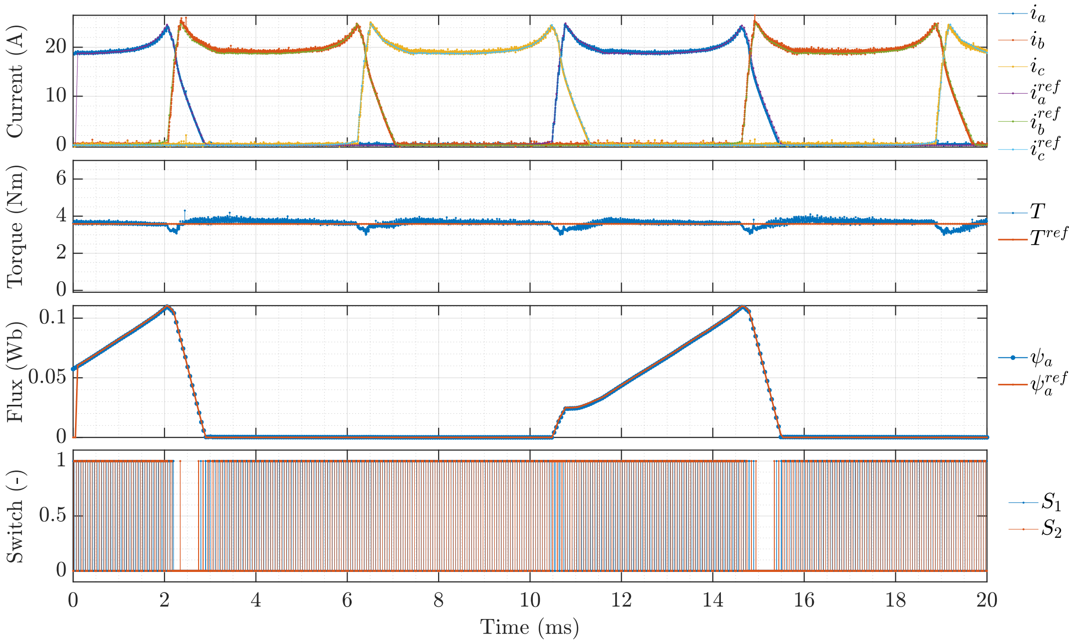

Figure 6.7: Experimental waveforms controlling with DBPC at $T^{ref} = 3.64$ `Nm` and $n = 600$ `rpm`

It can be seen from the last figure how DBPC manages to successfully track the flux-linkage reference and its equivalent currents, resulting in a torque experimental waveform that is practically identical to what was obtained by OSS-MPC in Section 6.2. However, as was also seen in the simulations, DBPC produces unnecessary switching during the instants in which the flux linkage reference is approximately zero. This can translate to extra stress on the semiconductors and additional switching losses that can be avoided, such as it does when OSS-MPC is implemented. As for the phenomena observed both in Section 6.2 and Section 6.3, where there is a current increment in a given phase when in the other two phases the current value changes rapidly, this becomes less obvious because of the continuous switching that occurs and the subsequent voltage vector application that reduces the current increment before it becomes noticeable.

Regarding the results of the experimental implementation of the FCS-MPC tracking algorithm, the waveforms of the variables of interest are shown in Fig. 6.8. This figure shows how the flux's tracking error is considerably higher than those observed with OSS-MPC and DBPC, directly affecting the output torque quality by displaying appreciable torque ripple. The above can be explained by noticing how the converter's switching frequency is less than the ones obtained by the other control algorithms. Nevertheless, even if the switching frequency is lower, the two switches that exist per phase do not present balanced switching, negatively impacting the hardware's lifetime in the long term. These observations confirm the ones made in the simulation chapter, which are fundamentally the same.

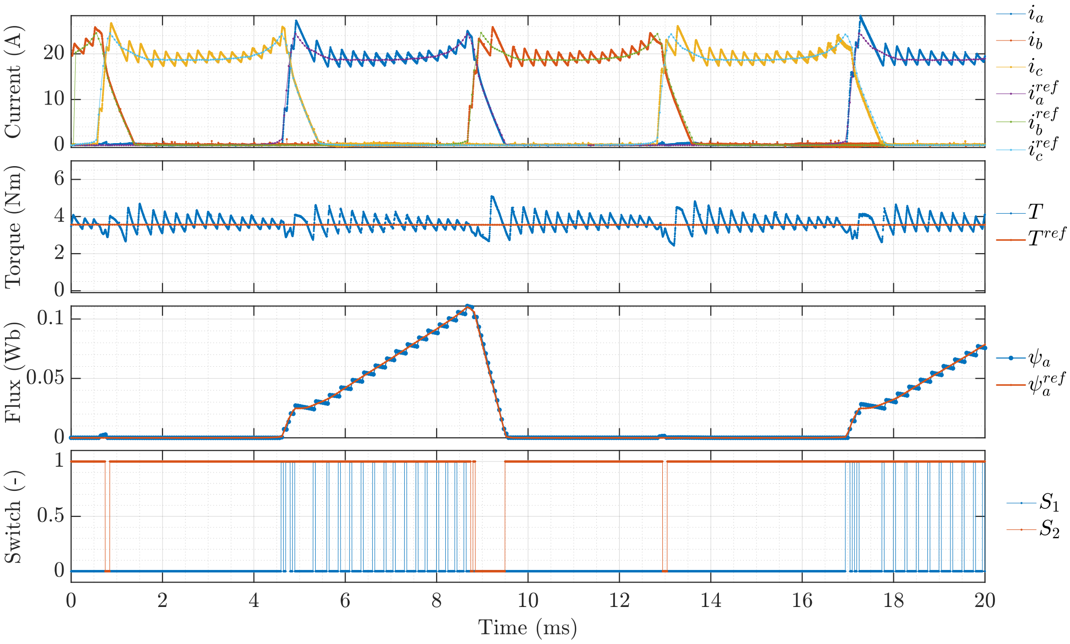

Figure 6.8: Experimental waveforms controlling with FCS-MPC at $T^{ref} = 3.65$ `Nm` and $n = 600$ `rpm`

## 6.5 Experimental performance comparison

The performance metrics of the experimental implementations presented in Sections 6.2, 6.3 and 6.4 are presented in Table 6.1 and Table 6.2, and displayed graphically in Fig. 6.9.

Table 6.1: Reference generation experimental performance metrics

| Metric | OFWG | TSF |
|---|---|---|
| $T_r$ (%) | 27.0 | 23.8 |
| $T_{\text{rmse}}$ (%) | 4.3 | 4.5 |
| $T_{\text{error}}$ (%) | 3.4 | 3.6 |
| $\hat{I}$( `A`) | 25.7 | 25.9 |
| $I_{\text{rms}}$( `A`) | 11.9 | 11.9 |
| $\psi_{\text{error}}$ (%) | 0.55 | 3.47 |

Table 6.2: Flux control strategy experimental performance metrics

| Metric | OSS | DB | FCS |
|---|---|---|---|
| $T_r$ (%) | 27.0 | 30.5 | 73.0 |
| $T_{\text{rmse}}$ (%) | 4.3 | 4.3 | 11.6 |
| $f_{\text{sw}}$( `kHz`) | 3.9 | 9.7 | 0.84 |
| $\hat{f}_{\text{sw}}$( `kHz`) | 3.9 | 9.8 | 1.4 |
| $\psi_{\text{error}}$ (%) | 0.55 | 0.68 | 2.0 |

Multiple observations can be made from these metrics. First, from Table 6.1 and Fig. 6.9a, it can be observed that the proposed reference generation strategy OFWG has a lower torque RMSE than TSF. In terms of the torque ripple, the proposed strategy is slightly worse than TSF, which was expected considering this same phenomenon occurs in simulation at this operation point, as seen in Table A.6. Nevertheless, both torque RMSE and torque ripple values are very similar; therefore, non-considerable improvement is appreciated in these aspects while using OFWG. As for the flux-tracking error, as was observed in Fig. 6.5 and Fig. 6.6, the reference obtained by OFWG was capable of being tracked unlike the references given by TSF. One of the benefits of better flux-tracking is that the error between the mean value of desired and measured torque reduces, as seen in Fig. 6.9a. At this operation point, no considerable benefits regarding RMS or the maximum current through the phases can be appreciated by tracking the references obtained using OFWG or TSF.

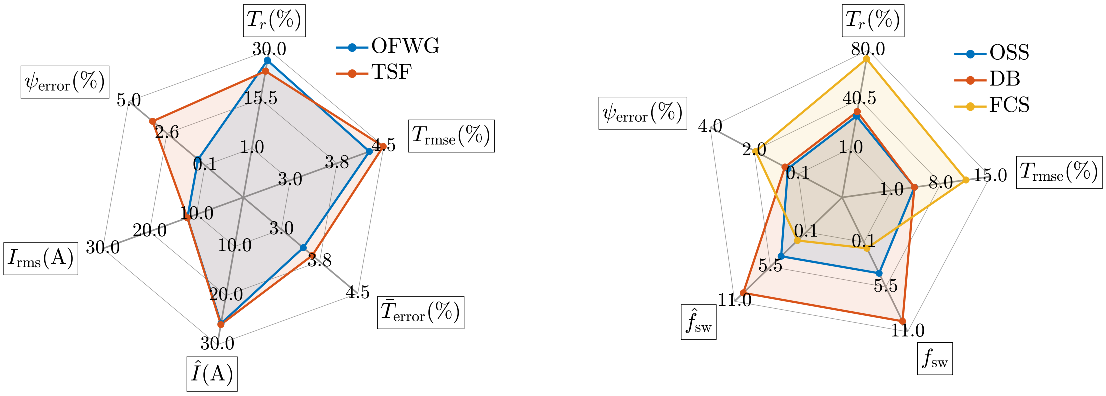

**(a)** **(b)**

Figure 6.9: Experimental comparison of the reference and flux-tracking performance metrics at $n = 600$ `rpm` and $T^{ref} \approx 3.69$ `Nm`. **(a)** Reference generation; **(b)** Flux-tracking.

Secondly, by observing Table 6.2 and Fig. 6.9b, it can be seen how the flux error, torque ripple, and torque RMSE are reduced when DBPC or the proposed OSS-MPC are implemented when compared to FCS-MPC. It is important to notice how the torque ripple implementing FCS-MPC is more than double the obtained with OSS-MPC, and the torque RMSE is almost four times bigger as well. Nevertheless, all these drawbacks benefit from a reduced but unbalanced switching frequency. As for the difference between the switching frequency between DBPC and OSS-MPC, it can be seen that the latter has less than half the switching frequency of the first, therefore avoiding unnecessary switching losses. Considering all these observations, it is fair to say that the OSS-MPC tracking algorithm is the most balanced regarding torque quality and switching frequency out of the rest of the state-of-the-art techniques used for flux-tracking in SRMs.

Considering the experimental results presented and their discussion, it can be confirmed that the experimental implementation of the proposed control strategy and its components behave as shown in the simulations presented in Chapter 5, and therefore, the control proposal is experimentally validated.

## 6.6 Maneuvers

A set of maneuvers are carried out to enrich the analysis and evaluation of the proposed control strategy. These maneuvers intend to show the tracking of the torque reference given by the speed's loop PI controller and, therefore, the flux-tracking quality at different operation points. The speed dynamic behavior will not be analyzed; however, it is expected to be slow considering the PI tuning presented in Section 6.1. Also, as was previously mentioned in this chapter, the position accuracy obtained by our current hardware reduces at high speed, which translates into a performance reduction of the flux control and, thus, an increase of the torque ripple; this is why this metric is not notoriously reduced at high speeds. The implemented maneuvers will be start up, load connection, and load disconnection. These are shown in Fig. 6.10 and described in the following subsections.

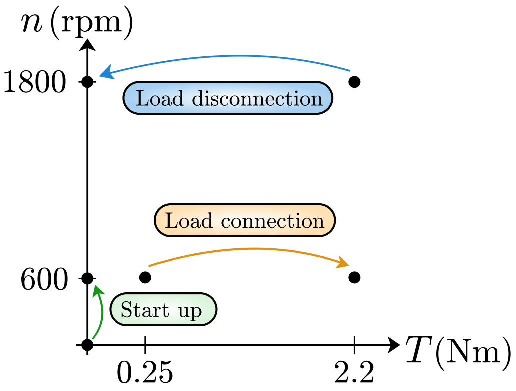

Figure 6.10: Experimental maneuvers

### 6.6.1 Start up

The SRM begins at zero speed without any load connected. The speed reference increases to 600 `rpm`, and the PI controller delivers an increasing reference torque until the desired operation point is reached. This maneuver's speed, current, torque, and flux waveforms are shown in Fig. 6.11.

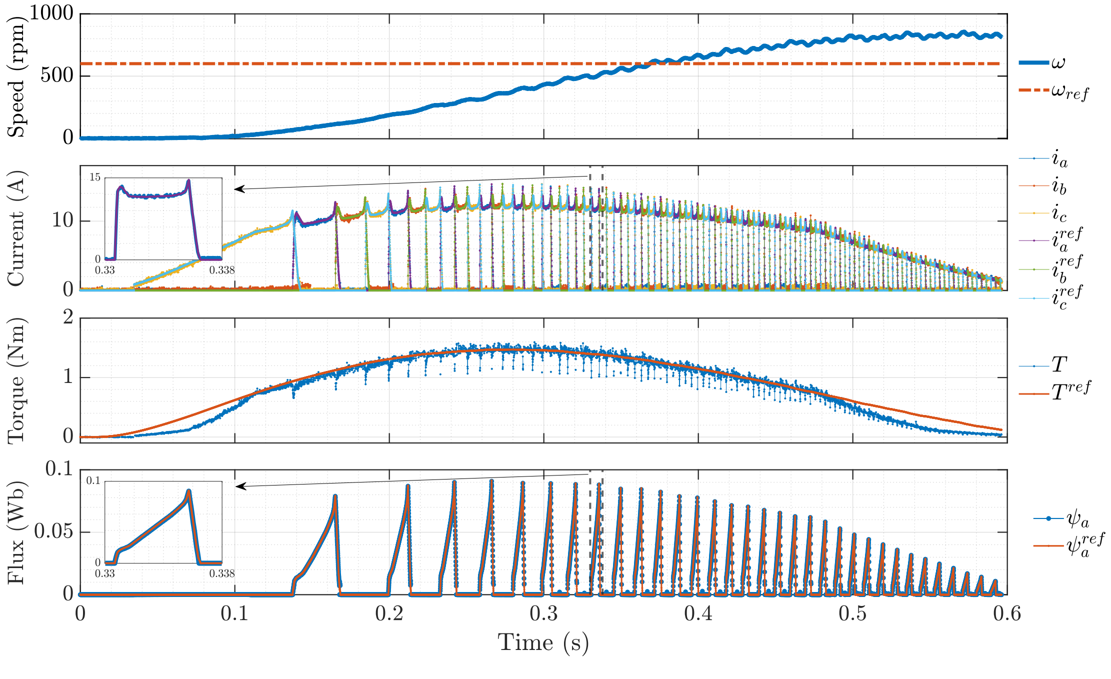

Figure 6.11: Motor's start up

It can be observed how the torque is tracked well during most parts of the maneuver. The torque reference is different from the measured torque only when the torque reference is below 0.738 `Nm`, which equals 20% of the nominal torque. This occurs because the optimal flux patterns were computed for discretized values of average torque, more specifically, multiples of 0.2 times the nominal torque. The minimum and maximum values computed were 0.2 and 1.0 times the nominal torque value, respectively. For values of reference torque lesser than 0.738 `Nm`, the delivered flux patterns are obtained for 0.738 `Nm`, and no interpolation is made. Therefore, the reference and measured torque are different if the reference torque is below this minimum value. As a last observation, it is seen how the control strategy can successfully track different flux-linkage references and their respective current patterns as the motor accelerates toward its new operation point. To appreciate the previous, a zoomed view of the current and flux-linkage tracking between the instants delimited by the dashed grey lines is shown.

### 6.6.2 Load connection

While being the SRM controlled at a speed of 600 `rpm`, and also charged with a torque load of approximately 0.25 `Nm`, the IM suddenly applies a torque load of 2.2 `Nm`. The drive starts with a low torque load because the torque control function of the Parker drive, which controls the IM, inevitably applies a small torque when having a torque reference of zero. The speed, current, torque, and flux waveforms are shown in Fig. 6.12.

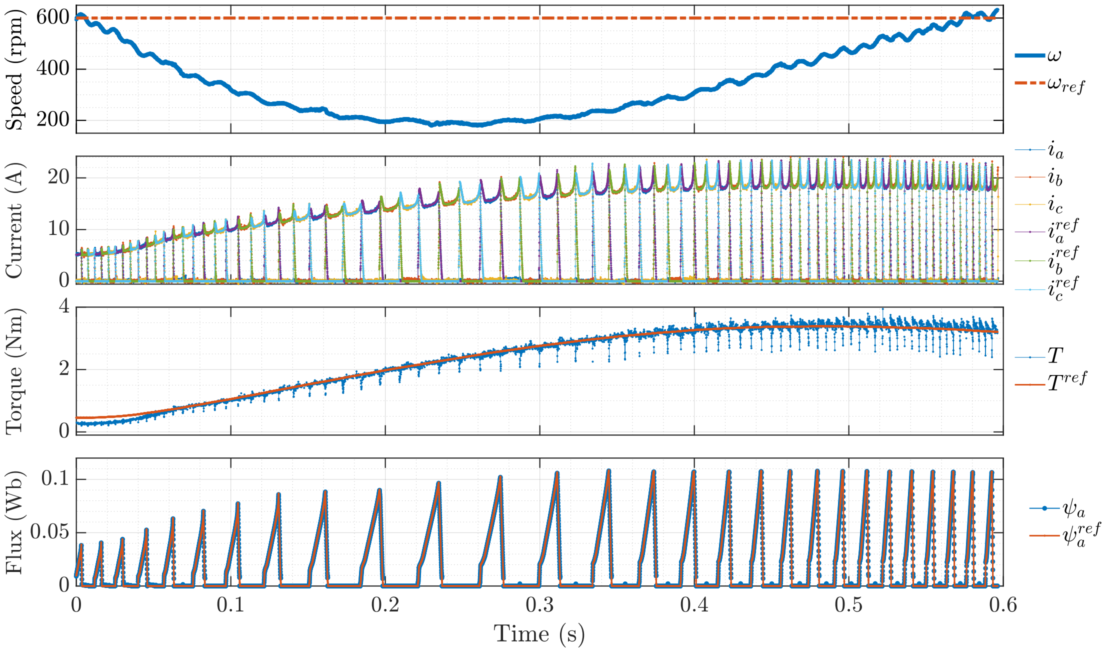

Figure 6.12: Motor's load connection

It becomes clear how, once the torque load is connected, the motor experiences a speed reduction, which causes the torque reference to rise until its nominal value. During this maneuver, the flux reference is successfully tracked, as it is the torque reference except for values below the 20% of the nominal value. It is shown clearly how the duration of excitation of each phase increases when the speed is reduced, as it is logical.

### 6.6.3 Load disconnection

The drive starts controlling a speed 1800 `rpm` while being loaded with a torque of 2.2 `Nm`. Suddenly, the load is disconnected, and the motor stops delivering torque until the reference speed is reached. This maneuver's speed, current, torque, and flux waveforms are shown in Fig. 6.13.

When suddenly the torque load is disconnected, the motor's speed starts increasing, which results in a reduction of the reference torque until it reaches zero, hence leaving the motor running and reducing its speed because of friction until the reference speed is reached, because the PI controller saturates at 0 `Nm` because no optimal patterns where computed for the machine to work with negative torque or negative speed. As shown in the torque reference is successfully tracked. Finally, a zoomed view of the current and flux-linkage tracking between the instants delimited by the dashed grey lines is shown. Here it is observed how the control strategy can successfully track the flux-linkage references and their respective current patterns. It is interesting to see how the current reference is not tracked perfectly, which is explained because the position can not be estimated precisely at high speeds because of the setup limitations, as previously mentioned in this work. Taking all the previous observations into consideration, the proposed strategy is validated and proves to be feasible and effective.

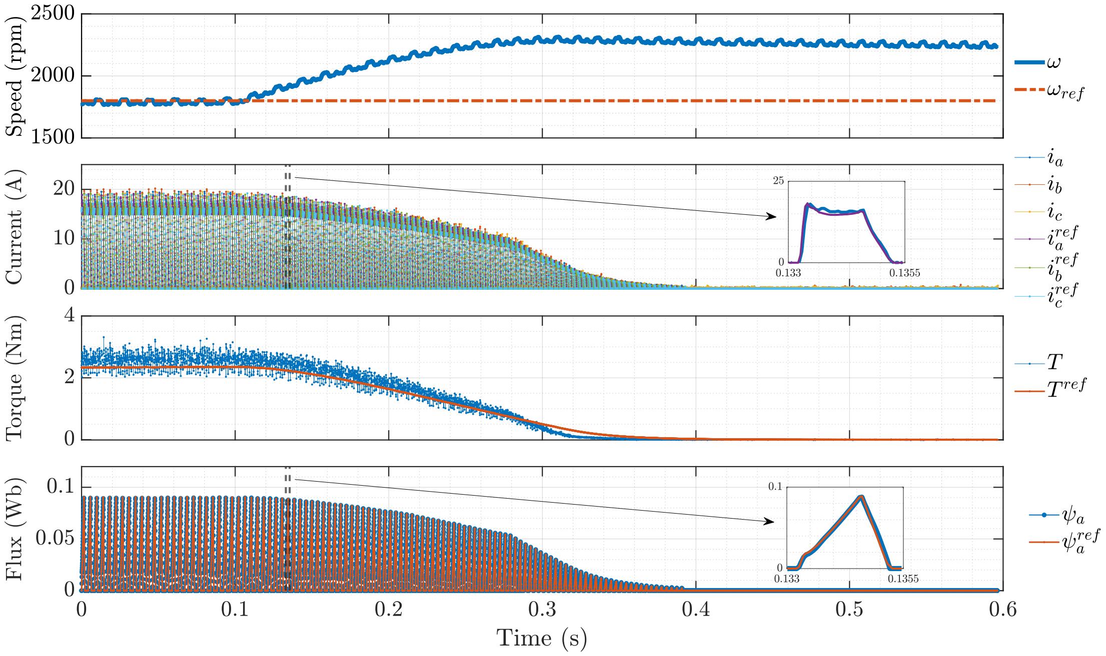

Figure 6.13: Motor's load disconnection

# Chapter 7

# Conclusion

This work proposed a control strategy to reduce the torque ripple in switched reluctance machines. The strategy is composed of two stages, the first being a reference generation stage and the second being a flux-tracking control algorithm. Several steps were needed to implement and validate the proposal. These steps and respective results will be discussed in this chapter.

First, an overview of the SRM is made, presenting its benefits and drawbacks, with the torque ripple recognized as one of the main disadvantages. Many reference generation and control strategies were presented, where TSF and MPC-based control are the most relevant in application and research nowadays.

Before proposing any control stage, identifying the nonlinear characteristics of the SRM is considered mandatory. An identification procedure was defined, and several experimental tests were made. The flux-linkage values were obtained from these measurements using the machine's electrical balance equation, and the torque values were obtained using a sensor.

To address the limitations of TSF, a reference generation strategy called OFWG was proposed. This strategy consists of solving an offline MICQP, which, unlike TSF, considers the machine's dynamics. The nonlinear characteristics of the SRM were inserted into the formulation using piecewise affine functions. The cost function of the MIQCP had two objectives to minimize (torque ripple and RMS current), so a weight parameter $\lambda$ was set, and a sensibility analysis was made as a function of this parameter. The results show that reducing the RMS current significantly impacts the torque ripple.

The subsequent contributions of this work are the introduction of an OSS-MPC algorithm for regulating the SRM's flux linkage, along with the proposal of a state machine implementation which considers the ABCs and motors characteristics. This implementation reduces the switching frequency by adjusting a user-defined parameter $\varepsilon$. To solve this algorithm along with its implementation, a two-stage optimization problem is solved. This problem can be solved online during each sampling window.

Once the proposed control stages are defined, the SRM model and the proposed control strategy are implemented in simulation. A sensitivity analysis was made with respect to $\varepsilon$, leading to a definitive choice on this parameter for the rest of this work. The chosen $\varepsilon$ allowed to considerably decrease the switching frequency while still keeping low torque ripple and flux-tracking error.

Afterwards, the OFWG references were compared by simulation with the ones obtained by TSF. A wide range of operation points was considered, and several performance metrics were analyzed. The results showed the overall superiority of the proposed technique with respect to TSF. The overall torque ripple is reduced by 4.2 %, the torque RMSE by 2.2 %, and the flux-tracking error by almost 50 times the obtained by using TSF. Also, the standard deviation of these metrics over the complete operation range proves OFWG to be more consistent than TSF. Nonetheless, an undesirable torque ripple is observed at small load and speed values due to the thickness of the discretization of the MICQP formulation, which should be improved in further works.

Furthermore, the proposed OSS-MPC is compared by simulation with other state-of-the-art control techniques, specifically FCS-MPC and DBPC. As with the references, a wide range of operation points was considered, and several performance metrics were analyzed. The results show how the OSS-MPC is more balanced than FCS and DB, which neglect flux-tracking or switching frequency on behalf of the other. OSS-MPC achieves low torque ripple and flux-tracking error while maintaining low switching frequency values.

The proposal's validity is confirmed through an experimental setup involving the SRM operating as a motor coupled to an IM operated as a regenerative brake. An external speed control loop controlled the SRM, and an external AC drive operating in torque control mode controlled the IM. Some considerations were taken, such as observing an estimation of the torque signal due to the sensor's limitations. Also, the SRM outer speed control loop was set to have very slow responses to overcome an error in the position reading. The proposed control strategy was tested on a single operating point and validated the results obtained by simulation. After that, some maneuvers were made in which the torque tracking was successful during transients.

Considering the abovementioned topics, the proposed strategy control to mitigate the torque ripple on an SRM using an optimization-based approach is validated, and its benefits over other state-of-the-art techniques are proven. As a consequence of the results obtained in this work, several possible improvements can be identified, which lead to define the problems that future research should address.

As for the offline flux-linkage pattern generation procedure, discretizing the electrical cycle in the MIQCP leads to undesirable torque ripple. This could be avoided by identifying reliable functional representations of the nonlinear characteristics of the SRM, which would allow reformulating the optimization problem with continuous variables of current and position.

The proposed OSS-MPC strategy only considered sequences composed of three vectors; therefore, considering sequences of two vectors may further reduce the converter's switching frequency. Also, this metric and the flux-tracking error could be reduced by formulating and implementing a multiperiod version of the proposed strategy.

Finally, more operation scenarios could be studied, such as operating the SRM as a generator or running it at higher speeds. The above would allow to identify the potential and further challenges associated with this electrical machine.

# Appendix A

# Appendix

## A.1 MICQP parameters

The parameters used in the MIQCP presented in Chapter 4 can be subdivided into two subgroups because multiple optimizations are made, in which some parameters vary. The first group is the constant parameters and remains unchanged for every optimization. These parameters are shown in Table A.1. The 2-D matrices that represent the parameters of these dimensions will not be shown in this appendix because of their size but are built considering the model's characteristics presented in Chapter 3.

Table A.1: Constant parameters used for the MIQCP

| Parameter | Value |
|---:|:---:|
| $N_{ph}$ (-) | 3 |
| $N_L$ (-) | 90 |
| $N_S$ (-) | 16 |
| $\xi$ (%) | 10 |
| $i^{max}$ (`A`) | 30 |
| $\hat{I}_{rms}$ (`A`) | 13.29 |
| $R$ ($\Omega$) | 0.18 |
| $V_{dc}$ (`V`) | 155 |

The second subgroup corresponds to the parameters modified to run different optimizations, each with different operation points or weights on the multi-objective cost function. These parameters are shown in Table A.2.

Table A.2: Variable parameters used for the MIQCP

| Parameter | Value |
|---:|:---:|
| $\omega$ ($\frac{\text{rad}}{\text{s}}$) | $\frac{8\pi}{30} \times \{600, 1200, 1800, 2400, 3000\}$ |
| $\bar{T}$ (`Nm`) | $3.69 \times \{0.1, 0.2, 0.3, ..., 1\}$ |
| $\lambda$ (-) | $\left\{10^{-1}, 10^{0}, 10^{1}, 10^{2}, 10^{4}\right\}$ |

The $\omega$ parameter is proportional to the desired speed at which the motor is run, which in this work is expressed with `rpm` units. Considering that with each mechanical cycle, the motor has made eight electrical cycles, a factor of $\frac{8\pi}{30}$ must be applied to speeds expressed in `rpm`. The speeds on which optimizations are run are multiples of 600 `rpm`. As for the average torque, the values to which the optimizations are made are ten percent steps of the nominal torque value, starting from zero to the motor's maximum.

## A.2 Equipment

To test the proposed strategy, an experimental setup was built. The most important hardware devices that compose this setup are partially described in Chapter 6, and Table A.3 are presented with more detail.

Table A.3: Hardware used for the experimental validation of the proposed strategy

| Device | Manufacturer | Model |
|---|---|---|
| Digital Control Platform | AC3E | BRAIn |
| Resolver | Tamagawa | TS2224N14E102 |
| Resolver-to-digital converter | ADDI-DATA | MSX-RDC-17 |
| IGBT | Infineon | FF50R12RT4 |
| SRM | MST | RB-165MR-250V |
| 3-Phase Induction Motor | Mitsubishi | L19666073 (Serial N°) |
| Torque Sensor | Forsentek | FYN-30-6000 |
| 3-Phase Rectifier Bridge | Microsemi | MSD50-08 |
| AC Drive | Parker | 690-432160 |

Some comments can be made about the hardware shown in Table A.3. First, the BRAIn platform is a commercial solution with an embedded DSP and FPGA. This proves the proposed strategy can be implemented successfully in a commercial platform. Second, it is suspected that the resolver to digital converter has a yet not known internal dynamic that impacts the position identification at high speeds. This will be solved in further work. The IM and the SRM manufacturer given nominal values are presented in Table A.4 and Table A.5, respectively.

Table A.4: IM parameters

| Parameter | Value |
|---|---|
| $P_{\text{nom}}$ ($\texttt{kW}$) | 2.23 |
| Poles (-) | 2 |
| $n_{\text{nom}}$ ($\texttt{rpm}$) | 2840 |
| $I_{\text{nom}}$ ($\texttt{A}$) | 4.5 |
| $V_{\text{nom}}$ ($\texttt{V}$) | 380 |

Table A.5: SRM parameters

| Parameter | Value |
|---|---|
| $P_{\text{nom}}$ ($\texttt{kW}$) | 2.32 |
| $T_{\text{nom}}$ ($\texttt{Nm}$) | 3.69 |
| $n_{\text{nom}}$ ($\texttt{rpm}$) | 6000 |
| $R_{\text{ph}}$ ($\Omega$) | 0.185 |
| $V_{\text{nom}}$ ($\texttt{V}$) | 250 |
| $N_{\text{ph}}$ ($-$) | 3 |
| Poles (-) | 8 |
| $I_{\text{nom}}$ ($\texttt{A}$) | 13.29 |
| $I_{\text{peak}}$ ($\texttt{A}$) | 30 |

Also, in this work, the base value for the flux is set as $\psi_{\text{nom}} = 0.049\ \texttt{Wb}$ and is defined from the SRMs nominal torque and speed values. It is defined according to $\frac{V_{\text{nom}}}{\omega_{\text{nom}}}$, where $\omega_{\text{nom}} = \frac{8\pi}{30} \times n_{\text{nom}}$.

## A.3 Simulated performance metrics

### A.3.1 Reference generation comparison

Two flux-linkage reference generation strategies, OFWG and TSF, were implemented by simulation at different scenarios in Chapter 5. The performance metrics for 25 different operation points are displayed from Table A.6 to Table A.11.

Table A.6: Torque ripple $T_r$ (%). Reference generation comparison.

| $n = 600$ `rpm` | | |
|---|---|---|
| $T^{ref}$ (`Nm`) | OFWG | TSF |
| 0.74 | 34.3 | 20.4 |
| 1.48 | 28.2 | 13.6 |
| 2.21 | 21.9 | 11.8 |
| 2.95 | 25.7 | 13.1 |
| 3.69 | 16.1 | 12.8 |
| $n = 1200$ `rpm` | | |
| $T^{ref}$ (`Nm`) | OFWG | TSF |
| 0.74 | 21.6 | 16.9 |
| 1.48 | 16.0 | 15.4 |
| 2.21 | 18.0 | 18.5 |
| 2.95 | 18.6 | 20.6 |
| 3.69 | 16.5 | 20.0 |
| $n = 1800$ `rpm` | | |
| $T^{ref}$ (`Nm`) | OFWG | TSF |
| 0.74 | 27.8 | 21.6 |
| 1.48 | 21.5 | 20.8 |
| 2.21 | 19.6 | 24.2 |
| 2.95 | 20.5 | 30.8 |
| 3.69 | 19.6 | 32.2 |
| $n = 2400$ `rpm` | | |
| $T^{ref}$ (`Nm`) | OFWG | TSF |
| 0.74 | 32.2 | 23.1 |
| 1.48 | 22.7 | 29.5 |
| 2.21 | 22.1 | 26.9 |
| 2.95 | 22.3 | 35.1 |
| 3.69 | 21.1 | 60.6 |
| $n = 3000$ `rpm` | | |
| $T^{ref}$ (`Nm`) | OFWG | TSF |
| 0.74 | 36.1 | 26.6 |
| 1.48 | 25.9 | 41.6 |
| 2.21 | 24.2 | 51.2 |
| 2.95 | 24.4 | 41.1 |
| 3.69 | 23.0 | 56.0 |
| Total Average | | |
| — | 23.2 | 27.4 |
| Std Deviation | | |
| — | 5.3 | 13.6 |

Table A.7: RMS current $I_{\text{rms}}$(`A`). Reference generation comparison.

| $n = 600$ `rpm` | | |
|---|---|---|
| $T^{ref}$ (`Nm`) | OFWG | TSF |
| 0.74 | 5.1 | 6.2 |
| 1.48 | 7.3 | 8.5 |
| 2.21 | 9.1 | 11.1 |
| 2.95 | 10.6 | 12.0 |
| 3.69 | 12.1 | 12.3 |
| $n = 1200$ `rpm` | | |
| $T^{ref}$ (`Nm`) | OFWG | TSF |
| 0.74 | 5.2 | 5.9 |
| 1.48 | 7.5 | 10.1 |
| 2.21 | 9.2 | 9.5 |
| 2.95 | 10.8 | 11.0 |
| 3.69 | 12.2 | 12.5 |
| $n = 1800$ `rpm` | | |
| $T^{ref}$ (`Nm`) | OFWG | TSF |
| 0.74 | 5.2 | 6.4 |
| 1.48 | 7.6 | 10.7 |
| 2.21 | 9.4 | 10.8 |
| 2.95 | 11.0 | 11.0 |
| 3.69 | 12.5 | 12.7 |
| $n = 2400$ `rpm` | | |
| $T^{ref}$ (`Nm`) | OFWG | TSF |
| 0.74 | 5.3 | 6.2 |
| 1.48 | 7.6 | 10.6 |
| 2.21 | 9.6 | 10.6 |
| 2.95 | 11.3 | 11.3 |
| 3.69 | 12.9 | 12.3 |
| $n = 3000$ `rpm` | | |
| $T^{ref}$ (`Nm`) | OFWG | TSF |
| 0.74 | 5.4 | 6.3 |
| 1.48 | 7.8 | 10.0 |
| 2.21 | 9.9 | 10.6 |
| 2.95 | 11.7 | 11.4 |
| 3.69 | 13.3 | 12.6 |
| Total Average | | |
| — | 9.2 | 10.1 |
| Std Deviation | | |
| — | 2.7 | 2.2 |

Table A.8: Torque RMSE $T_{\text{rmse}}$ (%). Reference generation comparison.

| $n = 600$ `rpm` | | |
|---|---|---|
| $T^{ref}$ (`Nm`) | OFWG | TSF |
| 0.74 | 3.5 | 3.3 |
| 1.48 | 3.1 | 1.7 |
| 2.21 | 2.4 | 1.6 |
| 2.95 | 3.2 | 2.1 |
| 3.69 | 2.3 | 2.1 |
| $n = 1200$ `rpm` | | |
| $T^{ref}$ (`Nm`) | OFWG | TSF |
| 0.74 | 3.0 | 3.1 |
| 1.48 | 2.7 | 2.4 |
| 2.21 | 2.5 | 3.3 |
| 2.95 | 2.6 | 3.9 |
| 3.69 | 2.8 | 3.7 |
| $n = 1800$ `rpm` | | |
| $T^{ref}$ (`Nm`) | OFWG | TSF |
| 0.74 | 4.0 | 3.6 |
| 1.48 | 3.2 | 3.6 |
| 2.21 | 3.0 | 3.4 |
| 2.95 | 3.1 | 4.3 |
| 3.69 | 3.2 | 4.7 |
| $n = 2400$ `rpm` | | |
| $T^{ref}$ (`Nm`) | OFWG | TSF |
| 0.74 | 4.4 | 4.1 |
| 1.48 | 3.7 | 4.4 |
| 2.21 | 3.3 | 3.9 |
| 2.95 | 3.3 | 5.4 |
| 3.69 | 3.2 | 9.2 |
| $n = 3000$ `rpm` | | |
| $T^{ref}$ (`Nm`) | OFWG | TSF |
| 0.74 | 4.6 | 4.6 |
| 1.48 | 4.1 | 6.2 |
| 2.21 | 3.3 | 7.3 |
| 2.95 | 3.2 | 7.4 |
| 3.69 | 3.0 | 12.0 |
| Total Average | | |
| — | 3.2 | 4.5 |
| Std Deviation | | |
| — | 0.6 | 2.4 |

Table A.9: Average torque error $\bar{T}_{\text{error}}$ (%). Reference generation comparison.

| $n = 600$ `rpm` | | |
|---|---|---|
| $T^{ref}$ (`Nm`) | OFWG | TSF |
| 0.74 | 0.7 | 1.3 |
| 1.48 | 0.3 | 0.2 |
| 2.21 | 0.1 | 0.2 |
| 2.95 | 0.2 | 0.3 |
| 3.69 | 0.5 | 1.2 |
| $n = 1200$ `rpm` | | |
| $T^{ref}$ (`Nm`) | OFWG | TSF |
| 0.74 | 0.6 | 1.0 |
| 1.48 | 0.2 | 0.3 |
| 2.21 | 0.0 | 1.0 |
| 2.95 | 0.4 | 1.4 |
| 3.69 | 0.6 | 1.4 |
| $n = 1800$ `rpm` | | |
| $T^{ref}$ (`Nm`) | OFWG | TSF |
| 0.74 | 0.5 | 1.0 |
| 1.48 | 0.2 | 0.5 |
| 2.21 | 0.1 | 0.5 |
| 2.95 | 0.5 | 0.1 |
| 3.69 | 0.7 | 0.6 |
| $n = 2400$ `rpm` | | |
| $T^{ref}$ (`Nm`) | OFWG | TSF |
| 0.74 | 0.5 | 0.8 |
| 1.48 | 0.3 | 0.5 |
| 2.21 | 0.1 | 0.4 |
| 2.95 | 0.6 | 1.3 |
| 3.69 | 0.8 | 3.1 |
| $n = 3000$ `rpm` | | |
| $T^{ref}$ (`Nm`) | OFWG | TSF |
| 0.74 | 0.5 | 0.6 |
| 1.48 | 0.2 | 0.1 |
| 2.21 | 0.2 | 0.1 |
| 2.95 | 0.6 | 2.8 |
| 3.69 | 0.8 | 7.6 |
| Total Average | | |
| — | 0.4 | 1.1 |
| Std Deviation | | |
| — | 0.2 | 1.5 |

Table A.10: Maximum current $\hat{I}$ (`A`). Reference generation comparison.

| $n = 600$ `rpm` | | |
|---|---|---|
| $T^{ref}$ (`Nm`) | OFWG | TSF |
| 0.74 | 10.4 | 15.0 |
| 1.48 | 15.0 | 22.1 |
| 2.21 | 18.9 | 27.1 |
| 2.95 | 22.6 | 27.3 |
| 3.69 | 25.7 | 24.8 |
| $n = 1200$ `rpm` | | |
| $T^{ref}$ (`Nm`) | OFWG | TSF |
| 0.74 | 10.2 | 14.5 |
| 1.48 | 14.1 | 26.7 |
| 2.21 | 17.8 | 22.1 |
| 2.95 | 21.0 | 24.6 |
| 3.69 | 25.1 | 27.9 |
| $n = 1800$ `rpm` | | |
| $T^{ref}$ (`Nm`) | OFWG | TSF |
| 0.74 | 10.3 | 16.1 |
| 1.48 | 14.7 | 28.3 |
| 2.21 | 18.9 | 27.3 |
| 2.95 | 21.8 | 23.3 |
| 3.69 | 24.7 | 28.4 |
| $n = 2400$ `rpm` | | |
| $T^{ref}$ (`Nm`) | OFWG | TSF |
| 0.74 | 10.3 | 15.5 |
| 1.48 | 15.3 | 28.3 |
| 2.21 | 18.5 | 26.2 |
| 2.95 | 22.0 | 24.5 |
| 3.69 | 25.1 | 27.1 |
| $n = 3000$ `rpm` | | |
| $T^{ref}$ (`Nm`) | OFWG | TSF |
| 0.74 | 10.6 | 16.1 |
| 1.48 | 15.4 | 27.6 |
| 2.21 | 19.4 | 26.9 |
| 2.95 | 22.9 | 25.2 |
| 3.69 | 25.6 | 23.7 |
| Total Average | | |
| — | 18.3 | 23.9 |
| Std Deviation | | |
| — | 5.4 | 4.7 |

Table A.11: Flux-tracking error $\psi_{\text{error}}$ (%). Reference generation comparison.

| $n = 600$ `rpm` | | |
|---|---|---|
| $T^{ref}$ (`Nm`) | OFWG | TSF |
| 0.74 | 0.06 | 0.19 |
| 1.48 | 0.06 | 0.09 |
| 2.21 | 0.06 | 0.08 |
| 2.95 | 0.06 | 0.31 |
| 3.69 | 0.06 | 1.39 |
| $n = 1200$ `rpm` | | |
| $T^{ref}$ (`Nm`) | OFWG | TSF |
| 0.74 | 0.07 | 0.09 |
| 1.48 | 0.07 | 0.19 |
| 2.21 | 0.07 | 2.46 |
| 2.95 | 0.07 | 4.20 |
| 3.69 | 0.10 | 4.18 |
| $n = 1800$ `rpm` | | |
| $T^{ref}$ (`Nm`) | OFWG | TSF |
| 0.74 | 0.08 | 0.23 |
| 1.48 | 0.14 | 0.77 |
| 2.21 | 0.09 | 2.28 |
| 2.95 | 0.08 | 6.81 |
| 3.69 | 0.11 | 7.45 |
| $n = 2400$ `rpm` | | |
| $T^{ref}$ (`Nm`) | OFWG | TSF |
| 0.74 | 0.10 | 0.79 |
| 1.48 | 0.12 | 1.55 |
| 2.21 | 0.10 | 3.95 |
| 2.95 | 0.08 | 9.19 |
| 3.69 | 0.12 | 16.07 |
| $n = 3000$ `rpm` | | |
| $T^{ref}$ (`Nm`) | OFWG | TSF |
| 0.74 | 0.08 | 1.04 |
| 1.48 | 0.09 | 3.04 |
| 2.21 | 0.16 | 7.19 |
| 2.95 | 0.13 | 11.81 |
| 3.69 | 0.19 | 21.58 |
| Total Average | | |
| — | 0.09 | 4.28 |
| Std Deviation | | |
| — | 0.03 | 5.5 |

### A.3.2 Flux-linkage control comparison

Three flux-tracking strategies, OSS-MPC, FCS-MPC, and DBPC, were implemented by simulation at different scenarios in Chapter 5. The performance metrics for 25 different operation points are displayed from Table A.12 to Table A.16.

Table A.12: Torque Ripple $T_r$ (%). Flux-linkage control comparison.

| $n = 600$ rpm | | | | |
|---|---|---|---|---|
| $T^{ref}$ (Nm) | OSS | DB | FCS | FCS$_{100k}$ |
| 0.74 | 34.3 | 30.4 | 113.8 | 40.0 |
| 1.48 | 28.2 | 26.9 | 85.9 | 32.2 |
| 2.21 | 21.9 | 20.7 | 74.1 | 23.7 |
| 2.95 | 25.7 | 24.8 | 69.8 | 31.4 |
| 3.69 | 16.1 | 15.8 | 64.9 | 18.0 |
| $n = 1200$ rpm | | | | |
| $T^{ref}$ (Nm) | OSS | DB | FCS | FCS$_{100k}$ |
| 0.74 | 21.6 | 21.3 | 108.4 | 23.3 |
| 1.48 | 16.0 | 16.9 | 83.8 | 20.8 |
| 2.21 | 18.0 | 18.2 | 78.1 | 15.6 |
| 2.95 | 18.6 | 18.3 | 63.5 | 14.8 |
| 3.69 | 16.5 | 16.5 | 62.2 | 14.2 |
| $n = 1800$ rpm | | | | |
| $T^{ref}$ (Nm) | OSS | DB | FCS | FCS$_{100k}$ |
| 0.74 | 27.8 | 26.4 | 112.7 | 25.0 |
| 1.48 | 21.5 | 21.1 | 83.7 | 17.6 |
| 2.21 | 19.6 | 19.9 | 78.5 | 16.7 |
| 2.95 | 20.5 | 20.4 | 66.4 | 16.2 |
| 3.69 | 19.6 | 19.6 | 64.5 | 13.9 |
| $n = 2400$ rpm | | | | |
| $T^{ref}$ (Nm) | OSS | DB | FCS | FCS$_{100k}$ |
| 0.74 | 32.2 | 31.8 | 109.2 | 23.9 |
| 1.48 | 22.7 | 22.6 | 79.1 | 18.8 |
| 2.21 | 22.1 | 22.7 | 71.3 | 14.8 |
| 2.95 | 22.3 | 22.2 | 66.0 | 16.0 |
| 3.69 | 21.1 | 22.7 | 60.1 | 14.3 |
| $n = 3000$ rpm | | | | |
| $T^{ref}$ (Nm) | OSS | DB | FCS | FCS$_{100k}$ |
| 0.74 | 36.1 | 35.2 | 111.0 | 24.2 |
| 1.48 | 25.9 | 25.4 | 83.3 | 18.9 |
| 2.21 | 24.2 | 23.9 | 70.8 | 16.4 |
| 2.95 | 24.4 | 24.4 | 71.0 | 16.3 |
| 3.69 | 23.0 | 24.3 | 64.0 | 15.4 |
| Total Average | | | | |
| — | 23.2 | 22.9 | 79.8 | 20.1 |
| Std Deviation | | | | |
| — | 5.3 | 4.7 | 17.5 | 6.6 |

Table A.13: Torque RMSE $T_{\mathrm{rmse}}$ (%). Flux-linkage control comparison.

| $n = 600$ rpm | | | | |
|---|---|---|---|---|
| $T^{ref}$ (Nm) | OSS | DB | FCS | FCS$_{100k}$ |
| 0.74 | 3.5 | 3.4 | 17.8 | 4.8 |
| 1.48 | 3.1 | 3.1 | 12.7 | 3.6 |
| 2.21 | 2.4 | 2.4 | 10.9 | 2.7 |
| 2.95 | 3.2 | 3.1 | 10.2 | 3.4 |
| 3.69 | 2.3 | 2.2 | 11.2 | 2.6 |
| $n = 1200$ rpm | | | | |
| $T^{ref}$ (Nm) | OSS | DB | FCS | FCS$_{100k}$ |
| 0.74 | 3.0 | 3.0 | 16.8 | 3.7 |
| 1.48 | 2.7 | 2.7 | 12.1 | 2.7 |
| 2.21 | 2.5 | 2.5 | 10.5 | 2.2 |
| 2.95 | 2.6 | 2.5 | 8.6 | 2.1 |
| 3.69 | 2.8 | 2.6 | 9.7 | 2.1 |
| $n = 1800$ rpm | | | | |
| $T^{ref}$ (Nm) | OSS | DB | FCS | FCS$_{100k}$ |
| 0.74 | 4.0 | 3.9 | 16.6 | 3.5 |
| 1.48 | 3.2 | 3.2 | 10.4 | 2.3 |
| 2.21 | 3.0 | 3.0 | 9.5 | 2.1 |
| 2.95 | 3.1 | 3.0 | 10.2 | 2.0 |
| 3.69 | 3.2 | 3.0 | 8.8 | 2.1 |
| $n = 2400$ rpm | | | | |
| $T^{ref}$ (Nm) | OSS | DB | FCS | FCS$_{100k}$ |
| 0.74 | 4.4 | 4.4 | 15.4 | 3.6 |
| 1.48 | 3.7 | 3.7 | 9.5 | 2.5 |
| 2.21 | 3.3 | 3.3 | 9.2 | 2.1 |
| 2.95 | 3.3 | 3.2 | 11.4 | 2.0 |
| 3.69 | 3.2 | 3.1 | 8.3 | 2.1 |
| $n = 3000$ rpm | | | | |
| $T^{ref}$ (Nm) | OSS | DB | FCS | FCS$_{100k}$ |
| 0.74 | 4.6 | 4.6 | 16.1 | 3.1 |
| 1.48 | 4.1 | 4.0 | 11.4 | 2.4 |
| 2.21 | 3.3 | 3.3 | 11.0 | 2.2 |
| 2.95 | 3.2 | 3.2 | 9.6 | 2.4 |
| 3.69 | 3.0 | 2.9 | 8.9 | 2.4 |
| Total Average | | | | |
| — | 3.2 | 3.2 | 11.5 | 2.7 |
| Std Deviation | | | | |
| — | 0.6 | 0.6 | 2.8 | 0.7 |

Table A.14: Average switching frequency $f_{\mathrm{sw}}$(kHz). Flux-linkage control comparison.

| $n = 600$ rpm | | | | |
|---|---|---|---|---|
| $T^{ref}$ (Nm) | OSS | DB | FCS | FCS$_{100\mathrm{k}}$ |
| 0.74 | 3.6 | 10.0 | 0.4 | 2.0 |
| 1.48 | 3.8 | 10.0 | 0.6 | 2.7 |
| 2.21 | 3.9 | 10.0 | 0.6 | 2.9 |
| 2.95 | 3.8 | 10.0 | 0.6 | 2.8 |
| 3.69 | 3.8 | 10.0 | 0.6 | 3.2 |
| $n = 1200$ rpm | | | | |
| $T^{ref}$ (Nm) | OSS | DB | FCS | FCS$_{100\mathrm{k}}$ |
| 0.74 | 3.9 | 10.0 | 0.7 | 3.0 |
| 1.48 | 4.3 | 10.0 | 1.0 | 4.2 |
| 2.21 | 4.3 | 10.0 | 1.0 | 4.6 |
| 2.95 | 4.5 | 10.0 | 1.0 | 5.6 |
| 3.69 | 4.3 | 9.9 | 1.1 | 5.2 |
| $n = 1800$ rpm | | | | |
| $T^{ref}$ (Nm) | OSS | DB | FCS | FCS$_{100\mathrm{k}}$ |
| 0.74 | 4.2 | 10.0 | 1.0 | 4.1 |
| 1.48 | 4.6 | 10.0 | 1.2 | 5.8 |
| 2.21 | 4.8 | 10.0 | 1.5 | 6.4 |
| 2.95 | 5.0 | 10.0 | 1.6 | 7.0 |
| 3.69 | 4.9 | 10.0 | 1.6 | 7.4 |
| $n = 2400$ rpm | | | | |
| $T^{ref}$ (Nm) | OSS | DB | FCS | FCS$_{100\mathrm{k}}$ |
| 0.74 | 4.6 | 10.0 | 1.3 | 5.4 |
| 1.48 | 4.9 | 10.0 | 1.6 | 6.8 |
| 2.21 | 5.0 | 9.9 | 1.8 | 7.4 |
| 2.95 | 5.4 | 10.0 | 1.7 | 6.9 |
| 3.69 | 5.5 | 10.0 | 1.4 | 6.5 |
| $n = 3000$ rpm | | | | |
| $T^{ref}$ (Nm) | OSS | DB | FCS | FCS$_{100\mathrm{k}}$ |
| 0.74 | 4.8 | 10.0 | 1.6 | 6.4 |
| 1.48 | 5.4 | 10.0 | 1.8 | 7.4 |
| 2.21 | 5.7 | 9.9 | 1.8 | 6.1 |
| 2.95 | 6.0 | 10.0 | 1.4 | 5.5 |
| 3.69 | 5.8 | 9.9 | 1.2 | 4.4 |
| Total Average | | | | |
| — | 4.7 | 10.0 | 1.2 | 5.2 |
| Std Deviation | | | | |
| — | 0.7 | 0.0 | 0.4 | 1.7 |

Table A.15: Maximum switching frequency $f_{\mathrm{sw}}$(kHz). Flux-linkage control comparison.

| $n = 600$ rpm | | | | |
|---|---|---|---|---|
| $T^{ref}$ (Nm) | OSS | DB | FCS | FCS$_{100\mathrm{k}}$ |
| 0.74 | 3.6 | 10.0 | 0.7 | 3.6 |
| 1.48 | 3.8 | 10.0 | 1.0 | 4.9 |
| 2.21 | 3.9 | 10.0 | 1.1 | 5.3 |
| 2.95 | 3.8 | 10.0 | 1.2 | 5.3 |
| 3.69 | 3.8 | 10.0 | 1.1 | 5.8 |
| $n = 1200$ rpm | | | | |
| $T^{ref}$ (Nm) | OSS | DB | FCS | FCS$_{100\mathrm{k}}$ |
| 0.74 | 3.9 | 10.0 | 1.3 | 5.4 |
| 1.48 | 4.3 | 10.0 | 1.7 | 7.7 |
| 2.21 | 4.3 | 10.0 | 1.8 | 8.6 |
| 2.95 | 4.5 | 10.0 | 1.9 | 10.1 |
| 3.69 | 4.3 | 9.9 | 2.1 | 9.9 |
| $n = 1800$ rpm | | | | |
| $T^{ref}$ (Nm) | OSS | DB | FCS | FCS$_{100\mathrm{k}}$ |
| 0.74 | 4.2 | 10.0 | 1.7 | 7.8 |
| 1.48 | 4.6 | 10.0 | 2.2 | 10.6 |
| 2.21 | 4.8 | 9.9 | 2.7 | 12.0 |
| 2.95 | 5.0 | 10.0 | 2.8 | 13.4 |
| 3.69 | 4.9 | 10.0 | 2.9 | 13.8 |
| $n = 2400$ rpm | | | | |
| $T^{ref}$ (Nm) | OSS | DB | FCS | FCS$_{100\mathrm{k}}$ |
| 0.74 | 4.6 | 10.0 | 2.2 | 9.6 |
| 1.48 | 4.9 | 10.0 | 2.9 | 12.8 |
| 2.21 | 5.0 | 10.0 | 3.0 | 13.8 |
| 2.95 | 5.4 | 10.0 | 3.0 | 12.6 |
| 3.69 | 5.6 | 10.0 | 2.6 | 11.5 |
| $n = 3000$ rpm | | | | |
| $T^{ref}$ (Nm) | OSS | DB | FCS | FCS$_{100\mathrm{k}}$ |
| 0.74 | 4.8 | 10.0 | 2.8 | 11.7 |
| 1.48 | 5.4 | 10.0 | 3.2 | 13.6 |
| 2.21 | 5.7 | 10.0 | 2.8 | 10.9 |
| 2.95 | 6.0 | 10.0 | 2.3 | 9.4 |
| 3.69 | 5.8 | 9.9 | 1.8 | 7.6 |
| Total Average | | | | |
| — | 4.7 | 10.0 | 2.1 | 9.5 |
| Std Deviation | | | | |
| — | 0.7 | 0.0 | 0.8 | 3.2 |

Table A.16: Flux-tracking error $\psi_{\text{error}}\,(\%)$ .
Flux-linkage control comparison.

| $n = 600$ rpm | | | | |
|---|---|---|---|---|
| $T^{ref}$ (Nm) | OSS | DB | FCS | FCS$_{100k}$ |
| 0.74 | 0.06 | 0.02 | 2.41 | 0.63 |
| 1.48 | 0.06 | 0.04 | 1.43 | 0.59 |
| 2.21 | 0.06 | 0.08 | 3.51 | 0.32 |
| 2.95 | 0.06 | 0.12 | 2.39 | 0.63 |
| 3.69 | 0.06 | 0.15 | 1.68 | 0.37 |
| $n = 1200$ rpm | | | | |
| $T^{ref}$ (Nm) | OSS | DB | FCS | FCS$_{100k}$ |
| 0.74 | 0.07 | 0.02 | 1.54 | 0.32 |
| 1.48 | 0.07 | 0.04 | 3.73 | 0.34 |
| 2.21 | 0.07 | 0.08 | 4.27 | 0.36 |
| 2.95 | 0.07 | 0.12 | 1.65 | 0.36 |
| 3.69 | 0.10 | 0.17 | 1.67 | 1.05 |
| $n = 1800$ rpm | | | | |
| $T^{ref}$ (Nm) | OSS | DB | FCS | FCS$_{100k}$ |
| 0.74 | 0.08 | 0.03 | 1.68 | 0.65 |
| 1.48 | 0.14 | 0.04 | 1.70 | 0.37 |
| 2.21 | 0.09 | 0.09 | 3.53 | 0.43 |
| 2.95 | 0.08 | 0.12 | 3.88 | 0.65 |
| 3.69 | 0.11 | 0.16 | 3.93 | 0.45 |
| $n = 2400$ rpm | | | | |
| $T^{ref}$ (Nm) | OSS | DB | FCS | FCS$_{100k}$ |
| 0.74 | 0.10 | 0.05 | 1.72 | 0.38 |
| 1.48 | 0.12 | 0.08 | 2.19 | 0.98 |
| 2.21 | 0.10 | 0.11 | 4.61 | 0.44 |
| 2.95 | 0.08 | 0.13 | 4.30 | 0.95 |
| 3.69 | 0.12 | 0.18 | 3.41 | 0.46 |
| $n = 3000$ rpm | | | | |
| $T^{ref}$ (Nm) | OSS | DB | FCS | FCS$_{100k}$ |
| 0.74 | 0.08 | 0.03 | 2.05 | 0.41 |
| 1.48 | 0.09 | 0.04 | 3.99 | 0.71 |
| 2.21 | 0.16 | 0.14 | 2.64 | 0.51 |
| 2.95 | 0.13 | 0.15 | 3.83 | 0.53 |
| 3.69 | 0.19 | 0.21 | 3.47 | 0.82 |
| Total Average | | | | |
| — | 0.09 | 0.1 | 2.85 | 0.55 |
| Std Deviation | | | | |
| — | 0.0 | 0.0 | 1.1 | 0.2 |

# Bibliography

[1] Berker Bilgin, James Weisheng Jiang, and Ali Emadi. Switched reluctance motor drives : Fundamentals to applications. 2019.

[2] Sergio Vazquez, Ricardo P. Aguilera, Pablo Acuna, Josep Pou, Jose I. Leon, Leopoldo G. Franquelo, and Vassilios G. Agelidis. Model predictive control for single-phase npc converters based on optimal switching sequences. *IEEE Transactions on Industrial Electronics*, 63(12):7533–7541, Dec 2016.

[3] Nicholas Moehle and Stephen Boyd. Optimal current waveforms for switched-reluctance motors. In *2016 IEEE Conference on Control Applications (CCA)*, pages 1129–1136, Sep. 2016.

[4] IEA. Global ev outlook 2017. *https://www.iea.org/reports/global-ev-outlook-2017*, 2017.

[5] Berker Bilgin and Ali Emadi. Electric motors in electrified transportation: A step toward achieving a sustainable and highly efficient transportation system. *IEEE Power Electronics Magazine*, 1(2):10–17, June 2014.

[6] Berker Bilgin, Pierre Magne, Pawel Malysz, Yinye Yang, Vera Pantelic, Matthias Preindl, Alexandre Korobkine, Weisheng Jiang, Mark Lawford, and Ali Emadi. Making the case for electrified transportation. *IEEE Transactions on Transportation Electrification*, 1(1):4–17, June 2015.

[7] Berker Bilgin, Brock Howey, Alan Dorneles Callegaro, Jianbin Liang, Milan Kordic, Joshua Taylor, and Ali Emadi. Making the case for switched reluctance motors for propulsion applications. *IEEE Transactions on Vehicular Technology*, 69(7):7172–7186, July 2020.

[8] Gaoliang Fang, Filipe P. Scalcon, Dianxun Xiao, Rodrigo P. Vieira, Hilton A. Gründling, and Ali Emadi. Advanced control of switched reluctance motors (srms): A review on current regulation, torque control and vibration suppression. *IEEE Open Journal of the Industrial Electronics Society*, 2:280–301, 2021.

[9] X.D. Xue, K.W.E. Cheng, and S.L. Ho. Optimization and evaluation of torque-sharing functions for torque ripple minimization in switched reluctance motor drives. *Power Electronics, IEEE Transactions on*, 24:2076 – 2090, 10 2009.

[10] Xavier Rain, Mickaël Hilairet, and Olivier Bethoux. Comparative study of various current controllers for the switched reluctance machine. In *2010 IEEE Vehicle Power and Propulsion Conference*, pages 1–6, Sep. 2010.

[11] Diego F. Valencia, Silvio Rotilli Filho, Alan Dorneles Callegaro, Matthias Preindl, and Ali Emadi. Virtual-flux finite control set model predictive control of switched reluctance motor drives. In *IECON 2019 - 45th Annual Conference of the IEEE Industrial Electronics Society*, volume 1, pages 1465–1470, Oct 2019.

[12] Howard C. Lovatt and John Michael Stephenson. Computer-optimised smooth-torque current waveforms for switched-reluctance motors. 1997.

[13] S.A. Nasar. DC-switched reluctance motor. *Proceedings of the Institution of Electrical Engineers (London)*, 116(6):1048, June 1969.

[14] A.V. Rajarathnam, K.M. Rahman, and M. Ehsani. Improvement of hysteresis control in switched reluctance motor drives. In *IEEE International Electric Machines and Drives Conference. IEMDC'99. Proceedings (Cat. No.99EX272)*, pages 537–539, May 1999.

[15] I. Husain and M. Ehsani. Torque ripple minimization in switched reluctance motor drives by pwm current control. *IEEE Transactions on Power Electronics*, 11(1):83–88, Jan 1996.

[16] M. Ilic'-Spong, R. Marino, S. Peresada, and D. Taylor. Feedback linearizing control of switched reluctance motors. *IEEE Transactions on Automatic Control*, 32(5):371–379, May 1987.

[17] Xiaoyan Wang and Jih-Sheng Lai. Small-signal modeling and control for pwm control of switched reluctance motor drives. In *2002 IEEE 33rd Annual IEEE Power Electronics Specialists Conference. Proceedings (Cat. No.02CH37289)*, volume 2, pages 546–551 vol.2, June 2002.

[18] Syed Shahjahan Ahmad and G. Narayanan. Linearized modeling of switched reluctance motor for closed-loop current control. *IEEE Transactions on Industry Applications*, 52(4):3146–3158, July 2016.

[19] G. Schroder and J. Bekiesch. Adaptive current control for the srm. In *Proceedings of the IEEE International Symposium on Industrial Electronics, 2005. ISIE 2005.*, volume 1, pages 69–74, June 2005.

[20] Hsin-Ning Huang, Kai-Wei Hu, Yu-Wei Wu, Tai-Lang Jong, and Chang-Ming Liaw. A current control scheme with back emf cancellation and tracking error adapted commutation shift for switched-reluctance motor drive. *IEEE Transactions on Industrial Electronics*, 63(12):7381–7392, Dec 2016.

[21] H. Hannoun, M. Hilairet, and C. Marchand. Gain-scheduling pi current controller for a switched reluctance motor. In *2007 IEEE International Symposium on Industrial Electronics*, pages 1177–1182, June 2007.

[22] H. Naitoh and H. Ishikawa. A current controller for a switched reluctance motor based on model reference adaptive control. In *SPEEDAM 2010*, pages 1270–1275, June 2010.

[23] Fei Peng, Jin Ye, and Ali Emadi. A digital pwm current controller for switched reluctance motor drives. *IEEE Transactions on Power Electronics*, 31(10):7087–7098, Oct 2016.

[24] Jose Rodriguez and Patricio Cortes. *Predictive Control of Power Converters and Electrical Drives.* John Wiley and Sons, March 2012.

[25] Rajib Mikail, Iqbal Husain, Yilmaz Sozer, Mohammad S. Islam, and Tomy Sebastian. A fixed switching frequency predictive current control method for switched reluctance machines. *IEEE Transactions on Industry Applications*, 50(6):3717–3726, Nov 2014.

[26] Xing Zhang, Qingqing Yang, Mingyao Ma, Zhengyu Lin, and Shuying Yang. A switched reluctance motor torque ripple reduction strategy with deadbeat current control and active thermal management. *IEEE Transactions on Vehicular Technology*, 69(1):317–327, Jan 2020.

[27] Xin Li and Pourya Shamsi. Model predictive current control of switched reluctance motors with inductance auto-calibration. *IEEE Transactions on Industrial Electronics*, 63(6):3934–3941, June 2016.

[28] Xin Li and Pourya Shamsi. Inductance surface learning for model predictive current control of switched reluctance motors. *IEEE Transactions on Transportation Electrification*, 1(3):287–297, Oct 2015.

[29] Tobias Geyer. A comparison of control and modulation schemes for medium-voltage drives: Emerging predictive control concepts versus pwm-based schemes. *IEEE Transactions on Industry Applications*, 47(3):1380–1389, May 2011.

[30] Sergio Vazquez, Abraham Marquez, Ricardo Aguilera, Daniel Quevedo, Jose I. Leon, and Leopoldo G. Franquelo. Predictive optimal switching sequence direct power control for grid-connected power converters. *IEEE Transactions on Industrial Electronics*, 62(4):2010–2020, April 2015.

[31] Andrés Mora, Roberto Cárdenas-Dobson, Ricardo P. Aguilera, Alejandro Angulo, Felipe Donoso, and Jose Rodriguez. Computationally efficient cascaded optimal switching sequence mpc for grid-connected three-level npc converters. *IEEE Transactions on Power Electronics*, 34(12):12464–12475, Dec 2019.

[32] Andres Mora, Roberto Cardenas, Ricardo P. Aguilera, Alejandro Angulo, Pablo Lezana, and Dylan Dah-Chuan Lu. Predictive optimal switching sequence direct power control for grid-tied 3l-npc converters. *IEEE Transactions on Industrial Electronics*, 68(9):8561–8571, Sep. 2021.

[33] Changming Zheng, Tomislav Dragievi, Zhenbin Zhang, Jose Rodriguez, and Frede Blaabjerg. Model predictive control of lc-filtered voltage source inverters with optimal switching sequence. *IEEE Transactions on Power Electronics*, 36(3):3422–3436, March 2021.

[34] Vladan P. Vujii. Minimization of torque ripple and copper losses in switched reluctance drive. *IEEE Transactions on Power Electronics*, 27(1):388–399, Jan 2012.

[35] Chun Gan, Yu Chen, Qingguo Sun, Jikai Si, Jianhua Wu, and Yihua Hu. A position sensorless torque control strategy for switched reluctance machines with fewer current sensors. *IEEE/ASME Transactions on Mechatronics*, 26(2):1118–1128, 2021.

[36] Jin Ye, Berker Bilgin, and Ali Emadi. An extended-speed low-ripple torque control of switched reluctance motor drives. *IEEE Transactions on Power Electronics*, 30(3):1457–1470, March 2015.

[37] Zekun Xia, Berker Bilgin, Shamsuddeen Nalakath, and Ali Emadi. A new torque sharing function method for switched reluctance machines with lower current tracking error. *IEEE Transactions on Industrial Electronics*, 68(11):10612–10622, Nov 2021.

[38] Haoding Li, Berker Bilgin, and Ali Emadi. An improved torque sharing function for torque ripple reduction in switched reluctance machines. *IEEE Transactions on Power Electronics*, 34(2):1635–1644, Feb 2019.

[39] Rajib Mikail, Iqbal Husain, Yilmaz Sozer, Mohammad S. Islam, and Tomy Sebastian. Torque-ripple minimization of switched reluctance machines through current profiling. *IEEE Transactions on Industry Applications*, 49(3):1258–1267, May 2013.

[40] Rajib Mikail, Iqbal Husain, Mohammad S. Islam, Yilmaz Sozer, and Tomy Sebastian. Four-quadrant torque ripple minimization of switched reluctance machine through current profiling with mitigation of rotor eccentricity problem and sensor errors. *IEEE Transactions on Industry Applications*, 51(3):2097–2104, May 2015.

[41] Z. Q. Zhu, Beomseok Lee, Liren Huang, and Wenqiang Chu. Contribution of current harmonics to average torque and torque ripple in switched reluctance machines. *IEEE Transactions on Magnetics*, 53(3):1–9, March 2017.

[42] Cong Ma, Liyan Qu, Rakesh Mitra, Prerit Pramod, and Rakib Islam. Vibration and torque ripple reduction of switched reluctance motors through current profile optimization. In *2016 IEEE Applied Power Electronics Conference and Exposition (APEC)*, pages 3279–3285, March 2016.

[43] Wen Ding, Guoji Liu, and Pengyu Li. A hybrid control strategy of hybrid-excitation switched reluctance motor for torque ripple reduction and constant power extension. *IEEE Transactions on Industrial Electronics*, 67(1):38–48, Jan 2020.

[44] Zhiyue Yu, Chun Gan, Yu Chen, and Ronghai Qu. Dc-biased sinusoidal current excited switched reluctance motor drives based on flux modulation principle. *IEEE Transactions on Power Electronics*, 35(10):10614–10628, Oct 2020.

[45] R.B. Inderka and R.W.A.A. De Doncker. Ditc-direct instantaneous torque control of switched reluctance drives. *IEEE Transactions on Industry Applications*, 39(4):1046–1051, July 2003.

[46] A.D. Cheok and Y. Fukuda. A new torque and flux control method for switched reluctance motor drives. *IEEE Transactions on Power Electronics*, 17(4):543–557, July 2002.

[47] Christoph R. Neuhaus, Nisai H. Fuengwarodsakul, and Rik W. De Doncker. Predictive pwm-based direct instantaneous torque control of switched reluctance drives. In *2006 37th IEEE Power Electronics Specialists Conference*, pages 1–7, June 2006.

[48] Hao Wen and Zaiping Pan. A novel dead-beat torque control of switched reluctance machines. In *2011 International Conference on Electrical Machines and Systems*, pages 1–5, Aug 2011.

[49] Qianni Li, Aide Xu, Chaoyi Shang, and Lepeng Huang. Minimization torque ripple for srm based on flux linkage partition in db-dtfc. *MATEC Web of Conferences*, 306:04007, 01 2020.

[50] J. Villegas, S. Vazquez, J.M. Carrasco, and I. Gil. Model predictive control of a switched reluctance machine using discrete space vector modulation. In *2010 IEEE International Symposium on Industrial Electronics*, pages 3139–3144, July 2010.

[51] Cunhe Li, Guofeng Wang, Yan Li, and Aide Xu. An improved finite-state predictive torque control for switched reluctance motor drive. *IET Electric Power Applications*, 12(1):144–151, 2018.

[52] Rasul Tarvirdilu-Asl, Shamsuddeen Nalakath, Berker Bilgin, and Ali Emadi. A finite control set model predictive torque control for switched reluctance motor drives with adaptive turn-off angle. In *IECON 2019 - 45th Annual Conference of the IEEE Industrial Electronics Society*, volume 1, pages 840–845, Oct 2019.

[53] Aide Xu, Chaoyi Shang, Jiagui Chen, Jingwei Zhu, and Lele Han. A new control method based on dtc and mpc to reduce torque ripple in srm. *IEEE Access*, 7:68584–68593, 2019.

[54] H.C. Lovatt and J.M. Stephenson. Optimum excitation of switched reluctance motors. In *1997 Eighth International Conference on Electrical Machines and Drives (Conf. Publ. No. 444)*, pages 356–360, Sep. 1997.

[55] Keely Croxton, Bernard Gendron, and Thomas Magnanti. A comparison of mixed-integer programming models for non-convex piecewise linear cost minimization problems. *Management Science*, 49:1268–1273, 09 2003.

[56] Juan Vielma, Shabbir Ahmed, and George Nemhauser. Mixed-integer models for nonseparable piecewise-linear optimization: Unifying framework and extensions. *Operations Research*, 58:303–315, 04 2010.

[57] J. Holtz. Pulsewidth modulation for electronic power conversion. *Proceedings of the IEEE*, 82(8):1194–1214, 1994.

[58] F. Fröhr and F. Orttenburger. *Introduction to Electronic Control Engineering.* Siemens, 1982.